

博士論文

**Material Properties and Shear Behaviour of Clinker Ash**

(クリンカアッシュの材料特性及びせん断挙動)

平成 29 年 3 月

**Winter Michael James**

山口大学大学院理工学研究科

# Table of contents

## Chapter 1 Introduction

<b>1.1 Background.....</b>	<b>1-1</b>
<b>1.2 Process of generation and outline of properties of coal ash.....</b>	<b>1-3</b>
1.2.1 Process of generation.....	1-3
1.2.2 Outline of coal ash properties.....	1-4
<b>1.3 Production amount of and usage of coal ash.....</b>	<b>1-6</b>
1.3.1 Production amount of coal ash.....	1-6
1.3.2 Usage of coal ash.....	1-9
1.3.3 Amount of production and use of clinker ash.....	1-11
1.4 Laws and regulations related to the handling of coal ash.....	1-12
1.4.1 Legal system for the promotion of a recycling-based society.....	1-12
1.4.2 Handling of coal ash in the basic law for establishing the recycling-base society.....	1-13
1.4.3 Handling of coal ash in the legal system according to the basic law.....	1-14
1.4.4 Laws and standards relating to safety assessment of coal ash.....	1-17
<b>1.5 Literature review.....</b>	<b>1-19</b>
1.5.1 Physical properties.....	1-19
1.5.2 Mechanical properties.....	1-21
1.5.3 Chemical composition.....	1-24
<b>1.6 Objective and structure of this paper.....</b>	<b>1-26</b>
1.6.1 Objective of paper.....	1-26
1.6.2 Structure of paper.....	1-27
<b>1.7 Previous group research and innovation of this study.....</b>	<b>1-28</b>
<b>References.....</b>	<b>1-30</b>

## **Chapter 2 Material properties of clinker ash**

<b>2.1 Outline</b> .....	<b>2-1</b>
<b>2.2 Samples used</b> .....	<b>2-3</b>
<b>2.3 Physical properties</b> .....	<b>2-5</b>
2.3.1 Particle density.....	2-5
2.3.2 Particle distribution.....	2-6
2.3.3 Maximum and minimum density.....	2-7
<b>2.4 Particle Characteristics</b> .....	<b>2-8</b>
2.4.1 Particle shape.....	2-8
2.4.2 Single particle crushing tests.....	2-10
<b>2.5 Compaction and permeability characteristics</b> .....	<b>2-14</b>
2.5.1 Compaction characteristics.....	2-14
2.5.2 Permeability characteristics.....	2-17
<b>2.6 Summary</b> .....	<b>2-23</b>
<b>References</b> .....	<b>2-24</b>

## **Chapter 3 Static shear characteristics of clinker ash**

<b>3.1 Outline</b> .....	<b>3-1</b>
<b>3.2 Static shear characteristics from triaxial compression tests</b> .....	<b>3-1</b>
3.2.1 Specimen preparation method and test conditions.....	3-1
3.2.2 Testing apparatus and test method.....	3-2
3.2.3 Stress-strain relationship.....	3-5
3.2.4 Relationship between peak strength $\Phi_{\text{peak}}$ and degree of compaction $D_c$ .....	3-7
3.2.5 Relationship between peak strength $\Phi_{\text{peak}}$ and confining pressure $\sigma_c'$ .....	3-9
3.2.6 Stress-dilatancy behaviour of clinker ash.....	3-11
<b>3.3 Evaluation of the static shear strength of clinker ash</b> .....	<b>3-16</b>

3.3.1 Evaluation of residual strength $\Phi_{res}$ .....	3-18
3.3.2 Evaluation of $P_{cr}$ .....	3-19
3.3.3 Evaluation of material parameter $C$ .....	3-20
3.3.4 Evaluation of peak strength $\Phi_{peak}$ .....	3-22
<b>3.4 Coloured particle crushing observation.....</b>	<b>3-23</b>
3.4.1 Test procedure.....	3-23
3.4.2 Particle observation before and after shearing.....	3-24
<b>3.5 Summary.....</b>	<b>3-40</b>
<b>References.....</b>	<b>3-41</b>

## **Chapter 4 Dynamic shear characteristics of clinker ash**

<b>4.1 Dynamic deformation characteristics through small strain cyclic triaxial testing.....</b>	<b>4-1</b>
4.1.1 Outline.....	4-1
4.1.2 Specimen preparation and test conditions.....	4-1
4.1.3 Outline of test equipment.....	4-2
4.1.4 Samples used and test procedure.....	4-6
4.1.5 Organization of results.....	4-8
4.1.6 Dynamic deformation characteristics.....	4-10
4.1.7 Hardin-Drnevich model.....	4-12
<b>4.2 Initial shear rigidity characteristics through bender element testing.....</b>	<b>4-17</b>
4.2.1 Outline of test equipment and method of measurement.....	4-17
4.2.2 Bender element test method.....	4-22
4.2.3 Results.....	4-25
4.2.4 Comparison of results with other experiments.....	4-29
<b>4.3 Liquefaction strength characteristics through cyclic triaxial testing.....</b>	<b>4-30</b>
4.3.1 Specimen preparation and test conditions.....	4-30
4.3.2 Test equipment and test procedure.....	4-32

4.3.3 Test results.....	4-33
4.4 Summary.....	4-36
References.....	4-37

## **Chapter 5 Conclusions and further research**

5.1 Conclusions.....	5-1
5.2 Further research.....	5-3

## **Appendices**

A. Table of physical properties.....	A-1
B. Stress-strain relationships from triaxial compression tests.....	A-2
C. Mohr's stress circles from triaxial compression tests.....	A-5
D. Test results from cyclic triaxial liquefaction tests.....	A-8

# **Chapter 1 Introduction**

## **1.1 Background**

Coal has been used widely as an energy source around the world for a very long time, and within the integrated energy policy of Japan it is regarded as being one of the most important pillars of alternative energy, along with nuclear power. This is due to coal having several advantages over other forms of energy. There are numerous reserves of coal around the world, meaning it can be mined for a long time, and, unlike oil, which is mostly from the Middle East, coal can be imported from more politically stable countries such as Australia and Canada. Also, compared with oil, the cost per unit of heat is lower, making it economically favourable. Due to these advantages, the demand for coal has been increasing year by year and will likely continue to increase in the future.

Currently, a large amount of coal is being used by electric utility companies in order to supply power through incineration of the coal. This in turn leads to generation of coal ash, and as mentioned above, the demand for coal is increasing year by year and as such it can also be expected that the amount of coal ash generated will also increase.

One type of coal ash, known as fly ash, has been effectively used as an additive to cement, and as such around 95% of generated coal ash is being utilized. However, clinker ash, which makes up around 5-15% of generated coal ash, is still not being used effectively, with only 63% being used in 2003. In 2001, a new law to ensure the circulation of materials by society named “The Basic Law for Establishing the Recycling-based Society” was enacted, and following this other laws related to the environment such as “Waste Management Law”, “Law for Promotion of Effective Utilisation of Resources” and “Green Purchasing Law” were revised and implemented one after another. In

particular, in the “Law for Promotion of Effective Utilisation of Resources”, coal ash is designated as a “specified by-product for which in particular the effective use as a recycled resource should be promoted”. Also, in the “Law on Promoting Green Purchasing”, even fly ash which has a high rate of efficient use is deemed to “not be used enough in public works”, and as such it can be thought that it is even more important to advance effective use of clinker ash.

Taking into account the above, that there is a relatively low rate of effective use of clinker ash, that it is a designated product in the “Promotion of Effective Utilisation”, and that actual usage is low, it can be deemed necessary to expand the useful applications of clinker ash, such as a ground material where large amounts can be used at a time.

However, due to clinker ash being an artificially created material, there are many differing points when compared with naturally occurring soils, such as particle shape and strength. For example, after clinker ash is formed it is crushed in a grinder which leads to very complex and angular particle shapes, which in turn leads to high shear strength due to interlocking of particles. In addition, when coal is incinerated the ash falls from the high temperature boiler into a water tank below, where it rapidly cools and hardens, which leads to pores existing in the particles, making clinker ash a light material with high water retention and relatively high permeability. However, the particle strength of clinker ash is low, sometimes being crushable under pressure from just the fingers, which makes clinker ash a crushable material which could be an obstacle for use as a ground material.

The following is an outline of the sections of this chapter. In Section 1.2, the nature of the generation of coal ash in general and that of clinker ash is outlined. In Section 1.3, the amount of clinker ash and coal ash generated is presented along with the situation of usage. In Section 1.4, the legal aspects of the handling of clinker ash are given. In Section 1.5, a review of literature is given and in Section 1.6 the objective and layout of this paper are described. Section 1.7 notes previous research by this group and notes the innovation of the current research.

## **1.2 Process of generation and outline of properties of coal ash**

### **1.2.1 Process of generation**

Coal ash, although also generated from general industry (such as chemical or pulp and paper industries), is mainly generated from coal fired power plants in the electric power industry. There are two types of power plants, those which use the fluidized bed combustion system and those which use a pulverized coal combustion system, although the pulverized coal combustion system type is most commonly in use at the moment. The types of coal ash and process of generation in the pulverized coal combustion type power plants are shown in Figure 1.1. Coal ash is divided mainly into two types, fly ash and clinker ash. Clinker ash is formed from coal ash particles which stick to the hot walls of the boiler where they clump together before falling into a water tank below. It is mainly formed from sand and gravel type particles. Fly ash particles are light, spherical particles which become suspended in the combustion gas and are collected by an electrostatic precipitator. Fly ash particles are mainly composed of fines. The generation ratio of clinker ash to fly ash is around 5-15%:85-90%<sup>2)</sup>.



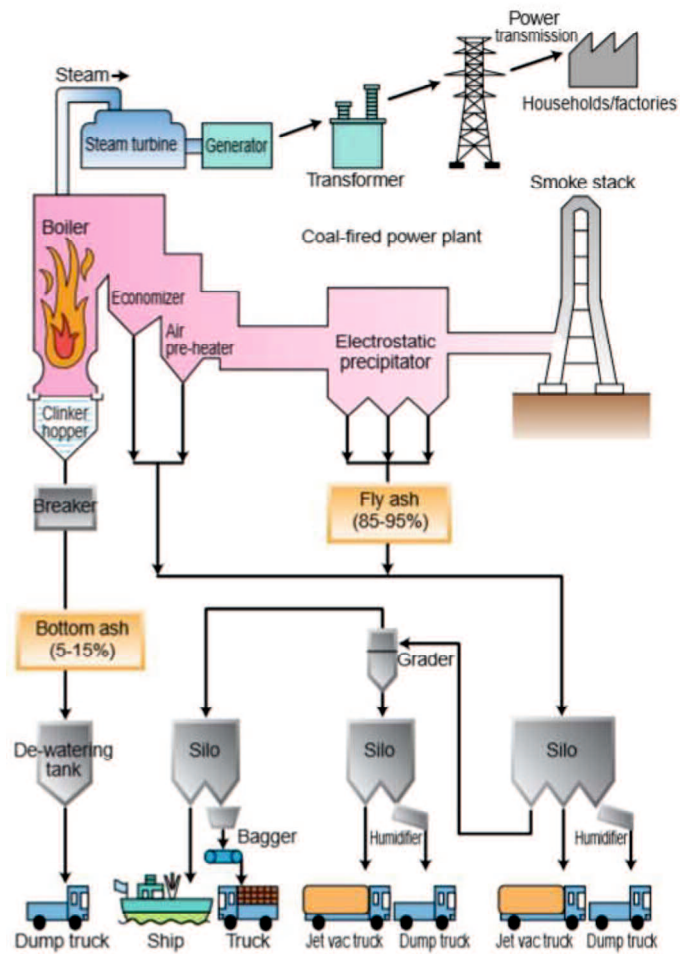


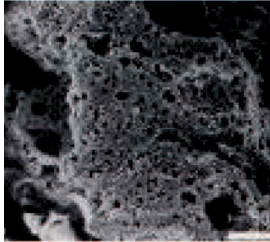



Figure 1.1 Generation process of coal ash in pulverized coal combustion type power plant<sup>1)</sup>

### 1.2.2 Outline of coal ash properties

An outline of the properties of clinker ash and fly ash generated through the pulverized coal combustion method is given in Table 1.1.

Table 1.1 Outline of coal ash properties<sup>2)</sup>

Type	Clinker Ash	Fly Ash
Colour/ Appearance		
Particle Shape		
Engineering Properties	Falls into a boiler in an incandescent state before being crushed in a grinder and then particle size adjusted. Chemically stable due to rapid cooling from incandescent state.	Mainly comprising silica-alumina, it causes a pozzolanic reaction with calcium hydroxide produced in hydration reactions in cement and forms a dense structure over time.
Physical Properties	<ul style="list-style-type: none"> <li>• Mainly coarse sand or fine gravel particles with the same particle distribution as high compaction performance sand.</li> <li>• High hydraulic conductivity like sand with drainage properties and high rate of water retention due to porous surface.</li> <li>• Lightweight with high shear strength</li> <li>• Density: Around 2.3(±0.3)g/cm<sup>3</sup></li> <li>• pH: Around 9(±1.5)</li> </ul>	<ul style="list-style-type: none"> <li>• Consisting of fine, spherical particles, fly ash is often mixed with concrete or mortar.</li> <li>• Over 90% of particle diameter less than 0.1mm in size, however basic properties are similar to sand and has high compaction performance.</li> <li>• Density: Around 1.3 (±0.3)g/cm<sup>3</sup></li> <li>• pH: Around 11 (Large variation)</li> </ul>
Chemical Composition	<p>&lt; Composition Ratio (Approx) &gt;</p> <p>SiO<sub>2</sub> : 65%</p> <p>Al<sub>2</sub>O<sub>3</sub> : 15%</p> <p>Fe<sub>2</sub>O<sub>3</sub> : 10%</p> <p>CaO : 5%</p> <p>Other : 5%</p>	<p>&lt; Composition Ratio (Approx) &gt;</p> <p>SiO<sub>2</sub> : 60%</p> <p>Al<sub>2</sub>O<sub>3</sub> : 20%</p> <p>Fe<sub>2</sub>O<sub>3</sub> : 5%</p> <p>CaO : 10%</p> <p>Other : 5%</p>

## **1.3 Production amount and usage of coal ash**

### **1.3.1 Production amount of coal ash**

As shown in Figure 1.2, compared with other forms of energy such as oil and natural gas, there are much larger reserves of coal spread widely around the world. Also, as shown in Figure 1.3, the amount produced in 2005 means that mining can be expected to continue for over 155 years. Coal is found in countries such as the United States, Russia and China, and as such, unlike oil which can be absent in some regions, it has the advantage of having a stable price and steady supply. The demand for coal in Japan continues to grow larger, and as shown in Figure 1.4, Japan imported 180,660,0000 tons of coal, making it the largest importer of coal in the world (17.6%).

As shown below, the types of coal used in Japan are classified as coking coal, thermal coal and anthracite, or smokeless coal. Of these, coal ash is generated from anthracite and thermal coal, although the use of anthracite is very small. Thermal coal is mainly used for generation of power, as shown in Figure 1.5, and is also used in other general industries such as cement, ceramic and chemical industries among others.

-Coking Coal: Used as an ingredient in coke and city gas production, and in coal chemical industry.

-Thermal Coal: Used in steam and power generating boilers and thermal radiators.

-Anthracite: As it causes less smoke, is used in home appliances such as charcoal briquettes.

According to the JCOAL Journal Vol. 18<sup>5)</sup>, the emission of coal ash in Japan is increasing every year. In 2008, the amount produced was 1,220,0000 tons, with a 40% increase occurring over the last 10 years.

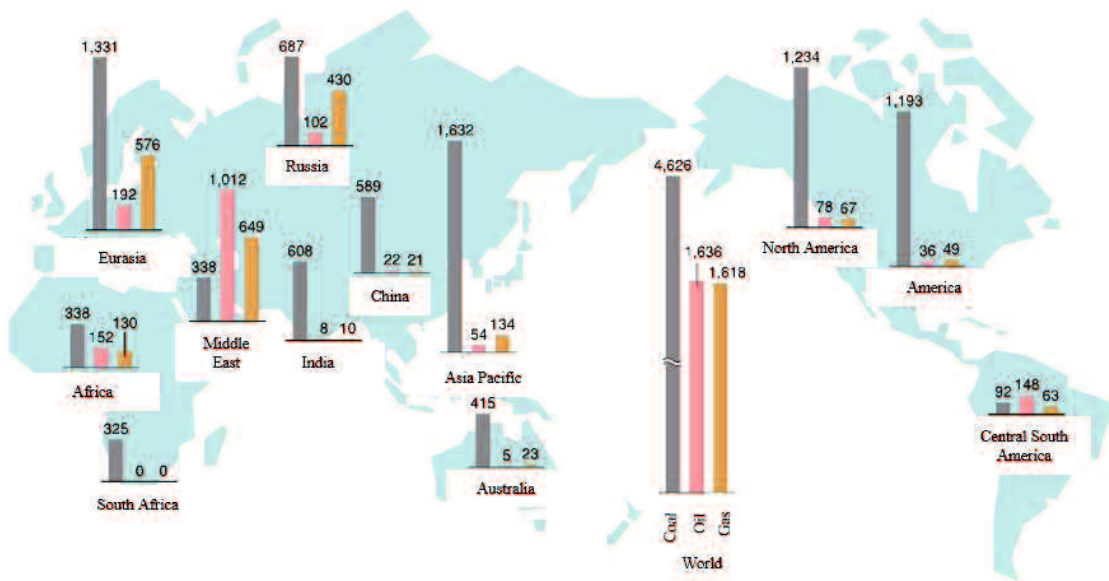


Figure 1.2 Reserves of oil, natural gas and coal worldwide (Equivalent to 100,000,000 tons of oil)<sup>3)</sup>

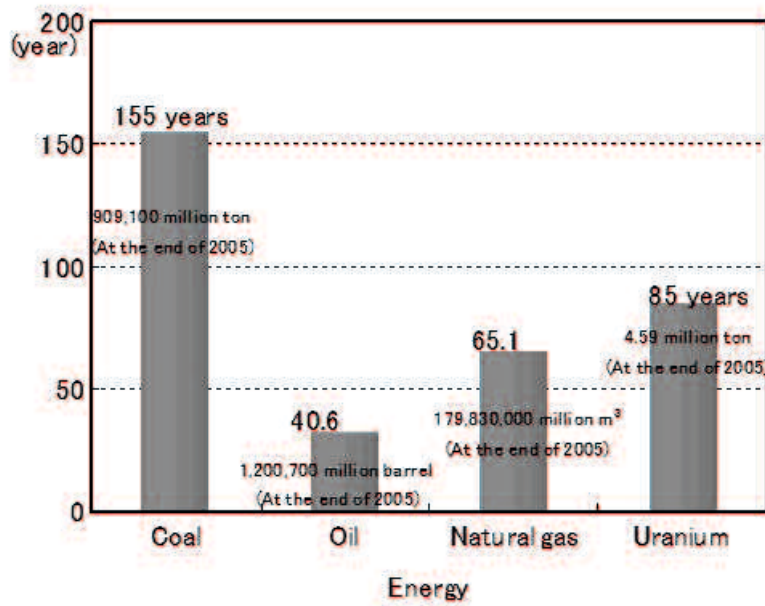


Figure 1.3 Recoverable amount and years' worth of major energy sources<sup>3)</sup>

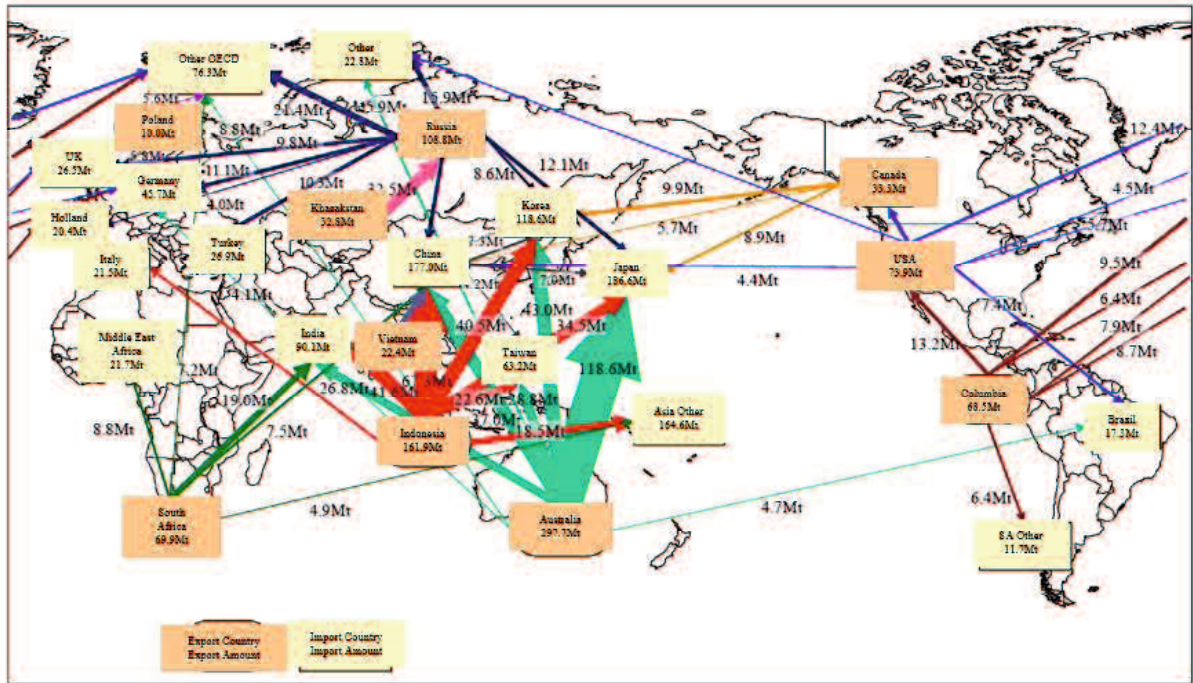


Figure 1.4 Flow-chart of worldwide import/export of coal<sup>4)</sup>

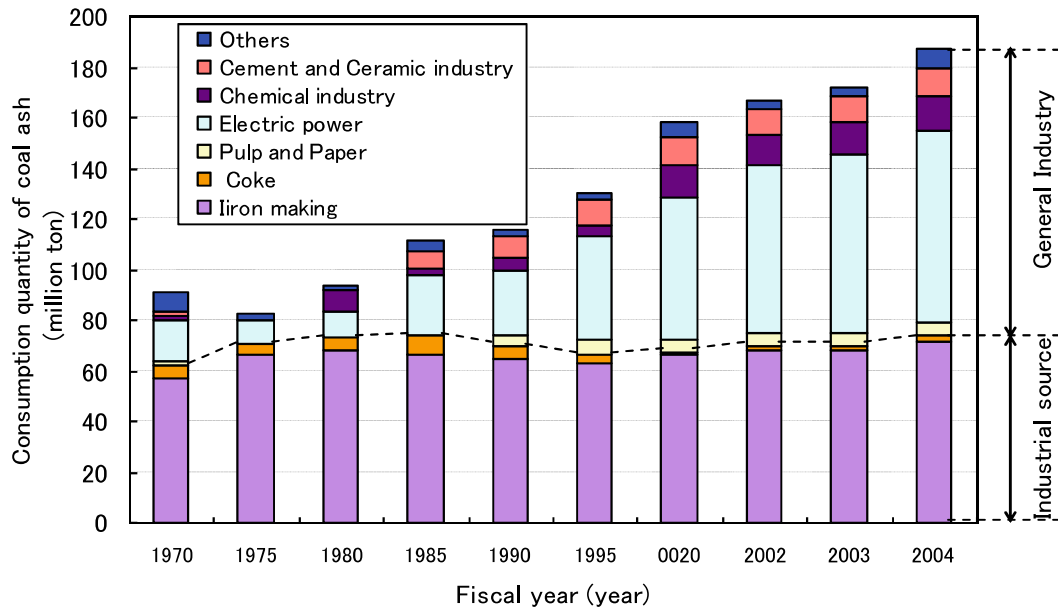


Figure 1.5 Changes in coal consumption by industry sector in Japan<sup>3)</sup>

### **1.3.2 Usage of coal ash**

Figure 1.6 shows the amount of coal ash effectively used up to the year 2008. As can be seen, there is an increase in the effective utilisation of coal each year, as in 1994 there was around 65% being effectively used which increases to approximately 98% by 2008. However, along with this there has also been a decrease in the amount of landfill space, and as such the problem of preserving landfills increases year by year. Although the amount of coal ash effectively used and that put into landfills is equal to the amount of coal ash being produced, this may not be so in the future as the amount of coal ash emitted increases.

Focus on the effective use of coal ash began in 1955. At first, research was carried out into the use of coal ash as an additive to concrete, and from the results of this it began to be used in dams. Then, from the 1970's when oil power plants took the place of coal fired power plants, the amount of coal ash being produced decreased, and this in turn led to a decrease in the development of utilization technology. However, after two oil crises there was again a turnaround in the use of coal as a source of energy and an increase in the construction of new coal fired power plants, which again led to an increase year by year of production of coal ash coupled with the introduction of imported coal.

Coal ash is currently used in large quantities in large structures such as dams, bridges, and hydro, thermal and nuclear power plants in additions to having applications as a road material, fertilizer building material and soil improvement material. Figure 1.7 shows the amount of effectively used coal ash by type. Coal ash is used as a raw material in a wide range of applications spread across cement, civil engineering, construction, agricultural, forestry, and fishing sectors. The cement sector uses the most coal ash at around 70%.

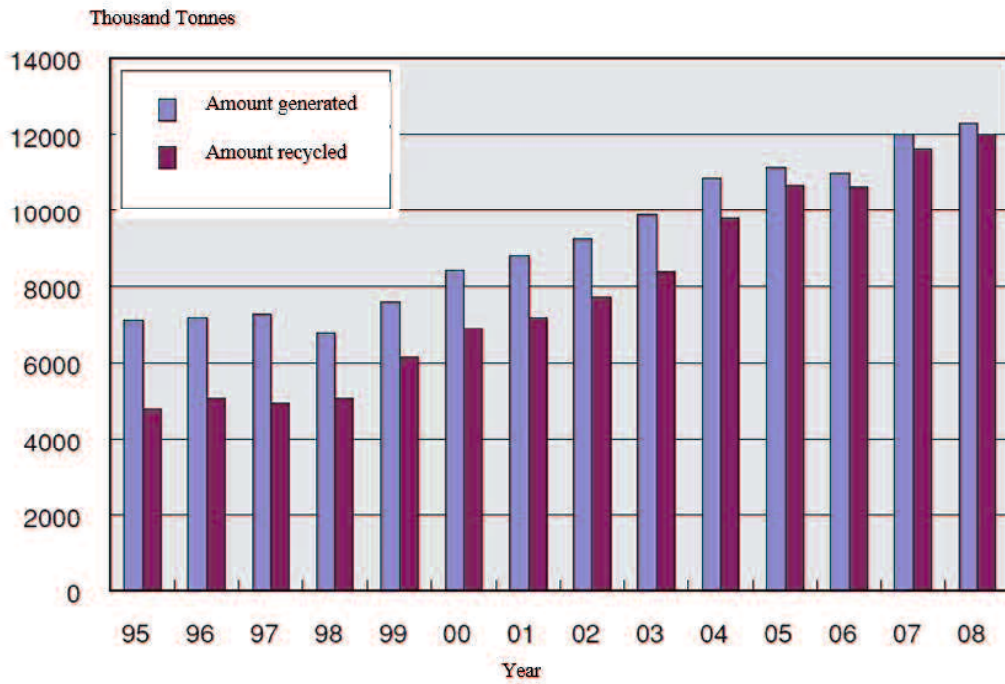


Figure 1.6 Amount of production and effective use of coal ash<sup>5)</sup>

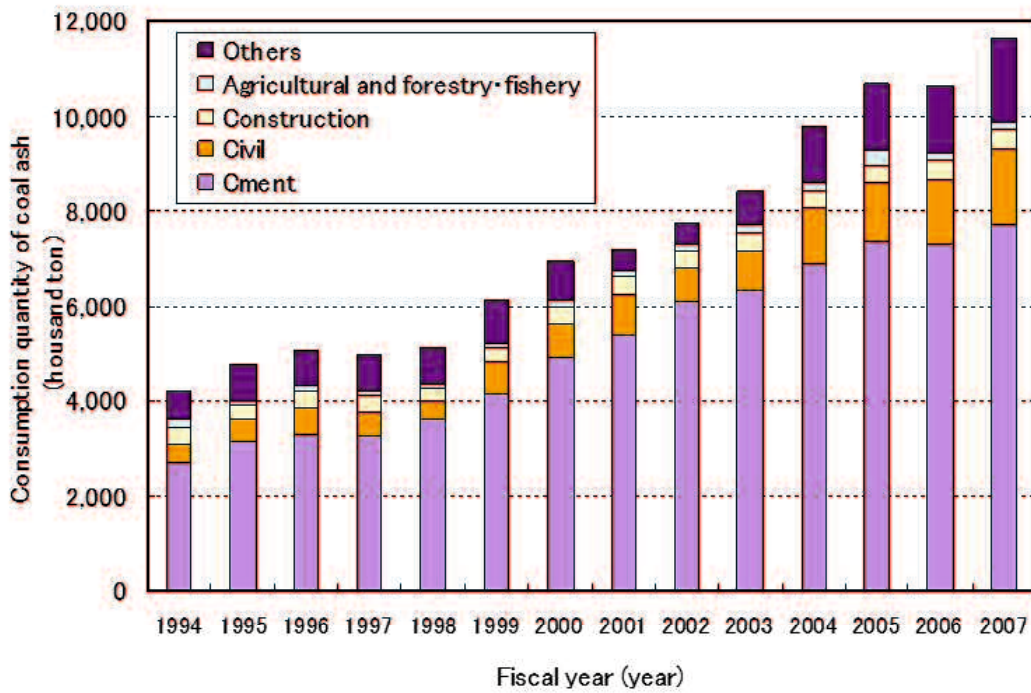


Figure 1.7 Breakdown of effective use of coal ash by sector<sup>4)</sup>

### **1.3.3 Amount of production and use of clinker ash**

Although there is little quantitative data on the amount of production and use of clinker ash, the environmental technology association Japan Fly Ash Association compiled data from coal fired power plants between 1999 and 2003 (see Figure 1.8).

According to the report, the amount of clinker ash produced has increased year by year since 1999, and in 2003 reached around the 700,000-ton mark. As for the amount being effectively used, although there was a slight reduction in 2002, overall there was a trend of increase. Unfortunately, exactly what ways clinker ash is being used, and in what amounts, is not disclosed.

Further, in 2003 the rate of effective use of coal ash as a whole was around 85%, whereas for the same year the rate of effective use of clinker ash was a relatively low 67%. This in some part is due to the fact that at the time, as clinker ash was mainly being treated as just a byproduct from coal fired power plants, it was not widely recognized as having the potential of being a ground material, and also there were no systems in place in order to transport large quantities of clinker ash from the power plants as cargo. However, in recent years, there has been development of such systems and from now it can be expected that there will be advancements in effective use.



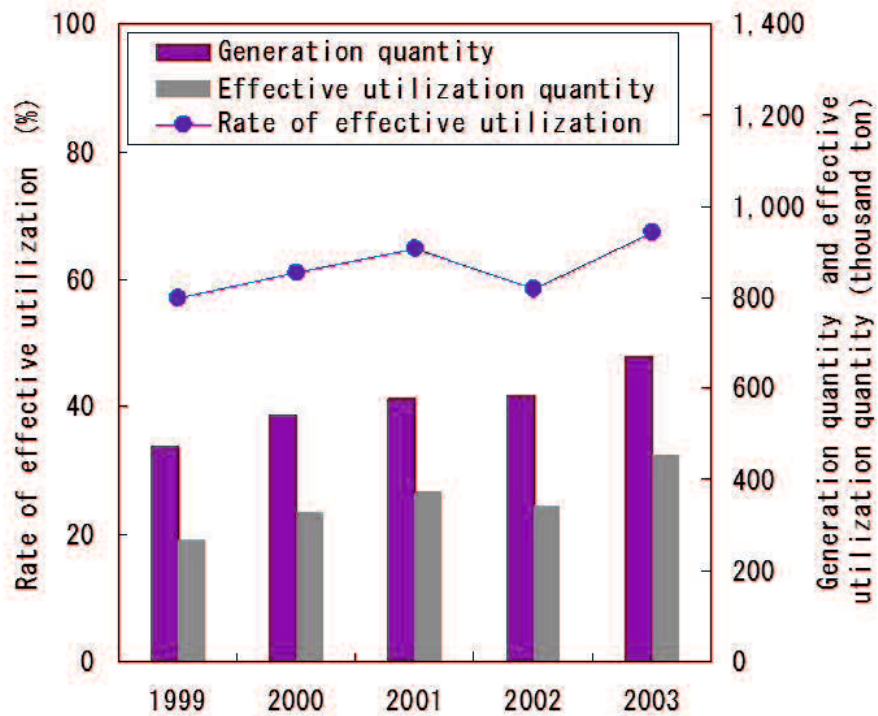


Figure 1.8 Amount of clinker ash produced and used<sup>1)</sup>

## 1.4 Laws and regulations related to the handling of coal ash

### 1.4.1 Legal system for the promotion of a recycling-based society

As coal ash is an industrial waste there are a number of laws and regulations relating to it. It can be seen that, in order to reasonably advance a plan given in the Ministry of the Environment's 2009 version of the Environment/Recycling-based Society/Biodiversity White Paper<sup>6)</sup>, there are laws and regulations related to the proper disposal of waste products and promotion of recycling. There is also the Green Purchasing Law in relation to support for demand and it is organized in order to advance the creation of a recycling-based society.

## **1.4.2 Handling of coal ash in the Basic Law for Establishing the Recycling-based Society**

The Basic Law for Establishing the Recycling-based Society (hereafter referred to as the Basic Law) was fully enforced in January, 2001. The objective of the Basic Law was to promote recycling and waste management, and move from a society of “mass production, mass consumption and mass disposal” to a recycling-based society.

In the Basic Law, the desired recycling-based society is defined as firstly reducing the amount of products becoming waste, and secondly using generated waste products as a raw material as much as possible. Finally, if there is no possible way to use the waste, it should be disposed of completely in an appropriate manner. It is a society which controls the consumption of natural materials and reduces the burden on the environment. In order to create this recycling-based society, firstly the generation of waste products (regardless of whether they have value or not) should be controlled, and secondly the generated waste which can be used should be defined as “recyclable resources”, whilst aiming for “reuse, recycling, and heat recovery”. Finally, there must be regulation of the proper disposal of waste which cannot be used, whilst ensuring that there is no negative impact on the environment.

In applying the above to coal fired power plants, the generation of the waste product (coal ash) which comes from the process of production of the product (electricity) can be controlled through improving the effectiveness of energy generation and using coal which generates less ash. The usable waste product generated (coal ash) can be reused as a recyclable product without harming the environment and the unusable part can be properly disposed of (disposed of in managed waste disposal sites). Therefore, in relation to the Basic Law for clinker ash, the proper disposal in managed disposal sites is regulated by the Waste Management Law, and recycling is regulated by the Law for Promotion of Use.

### **1.4.3 Handling of coal ash in the legal system according to the Basic Law**

#### a) Handling of coal ash in the Waste Management Law

In the Waste Management Law, “waste” is defined as “garbage, bulk waste, ash, sludge, manure, waste oil, waste acid, waste alkali, and animal corpses as well as unneeded solids and liquids (excluding radioactive substances or that contaminated by radiation).” Also, “industrial waste” is defined as “waste generated through business activities such as cinder, sludge, waste oil, waste acid, waste alkali and waste plastics as specified by government ordinance.

Based on this definition, the unneeded clinker ash corresponds to “cinder” from statutory industrial waste, and the fly ash corresponds to “ash” (defined in article 2, paragraph 2 of the Air Pollution Control Law as “soot and dust that occurs due to the use of electricity as a heat source or combustion of fuel and other things”) from government-designated industrial waste. Based on the Waste Management Law, the coal ash must be properly disposed of by either reusing or recycling it or disposing of it properly in a managed disposal site.

In the Waste Management Law, whether waste is unneeded or not is judged by the whether or not it can be used by those who created it and, if not, whether or not it can be sold to someone else for a profit. This in turn is judged by considering such things as the characteristics, the state of emission, form of conventional handling and whether or not it has transaction value. This overall judgment theory has also been adopted by a Supreme Court precedent.

#### b) Handling of coal ash in the Law for Promotion of Effective Utilization of Resources

The Law for Promotion of Effective Utilization of Resources aims to create a recycling based economic system through giving responsibility for the following four items to businesses:

- 1) Strengthening recycling measures such as product recovery and recycling.

2) Putting waste generation control measures in place through using long-life and resource-saving products.

3) Putting measures in place for the reuse of recovered products.

4) Promoting recycling and the control of waste byproduct generation.

Clinker ash falls into 4) as a designated byproduct for which effective use as a recycled resource must be advanced. In line with this basic policy, the power industry aims for initiatives relating to the expansion of reuse of waste byproducts by the company itself, whilst also developing technology for quality improvement.

#### c) Handling of coal ash in the Green Purchasing Law

The Green Purchasing Law contributes to a recycling-based society from the aspect of demand. The independent administrative agency and special government corporations (referred to hereafter as simply corporations) which are set by the country (parliament, ministries and courts) decide the “basic policies” each year, creating and officially announcing each corporation’s “provisional policies for aiming to promote the supply of environmental goods” and setting concrete objectives for the advancement of provisions for recycled goods. At the end of the year, the results of the provisions are published. At the end of 2001 there were 151 items spread across 14 sectors, including public work and service sectors, which were selected for this, and reviews are carried out annually depending on the state of development and scientific knowledge.

For coal ash-related products fly ash cement, a mixed cement used as a public works material, was designated as a special provisional item at the end of 2002. Other coal ash products were listed as shown below in the special provisional items candidate group published in May, 2003. Table 1.2 shows a table of the specific procured item candidate group.

According to the results of the investigation, there was a large problem with insufficient use of

these products in public works. However, as this is a system which aims to push for the advancement of effective use, it can be hoped that technology which makes effective use of coal ash will be adopted as a provisional item.

Table 1.2 Specific procured item candidate group (extract related to coal ash)<sup>1)</sup>

General Item Name	Proposed Item Name	Result
FS Concrete	FS Concrete	③② (①)
Coal ash calcined lightweight aggregate	High strength (fly ash) artificial aggregate	② (①)
Coal ash calcined lightweight aggregate	Calcined fly ash aggregate	② (①)
Shotcrete using coal ash	Shotcrete with coal ash powder	② (①)
Shotcrete using coal ash	Shotcrete admixture using coal ash	② (①)
Coal ash air bubble mixture lightweight soil	Air bubble mixture lightweight soil using coal ash	② (①)
Soil improvement material using coal ash	Soil improvement material using waste from thermal power plant	③② (①)
Asphalt mixture of mixed coal ash and molten slag	Paving colour aggregate using coal ash	③② (①)
Asphalt mixture of mixed coal ash and molten slag	Coal ash molten slag pavement (Fine ash pavement)	③② (①)
Soil improvement material using clinker ash	Method of usage for coal ash (fly ash) in construction generated soil	③② (①)

The meaning of “Result” is as follows:

- 1) After solving other problems it is necessary to confirm that there is expectation that along with the spread of cost it will be comparable in quality to similar products.
- 2) Use in public works is insufficient, evaluation and verification have not been sufficiently performed for actual and comparable conditions.
- 3) Does not meet or otherwise comply with public standards such as JIS or JAS, uncertainty remains about quality assurance. Note that for FS concrete mixed with slag, problems are raised relating to the expensive nature of slag.

#### **1.4.4 Laws and standards relating to safety assessment of coal ash**

As shown in the example in Table 1.3, coal ash contains heavy metals, although in very small amounts. Due to this, for effective use of coal ash attention must be paid to the Basic Law for Establishing the Recycling-based Society, Article 6 Clause 2, which states that it must be ensured that the reuse of recyclable materials must not damage the environment.

A basic criterion for judging if something will cause harm to the environment is given in Article 16 Clause 1, which states that a desirable standard is that which protects people's health and living environment, relating to atmospheric contamination, contamination of water quality and soil and noise pollution. These criteria can be divided into air, noise, water, soil and dioxins, however the standard generally used in evaluation of the safety in effective use of coal ash is given as follows:

- 1) Environmental standards relating to water pollution (environmental standards relating to the protection of human health): Health protection standards.
- 2) Environmental standards relating to water pollution of ground water: Groundwater pollution criteria.
- 3) Environmental standards relating to pollution of soil: Environmental quality standards for soil.
- 4) Effluent standards based on the Water Pollution Control Law: Effluent standard.
- 5) Criteria relating to heavy metal containing waste which will be discharge to a landfill site, as defined in the Act on Prevention of Maritime Disaster and the Marine Pollution Prevention Act: Emission standard.

In these environmental standards, there is the following relationship in the magnitude of the reference values of heavy metals incorporated in the safety assessment of coal ash for effective use:

- 1) Health protection standards=2) Groundwater pollution standards=3) Environmental quality standards for soil<3) Environmental quality standards for soil in the case of ground water not being contaminated<4) Effluent standard<5) Emission standard.

Table 1.3 Dissolution test results of coal ash (example)<sup>1)</sup>

Coal	Water	Alkyl Mercury	Total Mercury	Cadmium	Lead	Organic Phosphorous	Hexavalent Chromium	Arsenic	Cyan	PCB
Domestic	Pure	ND	ND	ND	ND	ND	0.19	ND	ND	ND
	Sea	ND	ND	ND	ND	ND	0.19	ND	ND	ND
China	Pure	ND	ND	ND	ND	ND	ND	ND	ND	ND
	Sea	ND	ND	ND	ND	ND	ND	ND	ND	ND
South Asia	Pure	ND	ND	ND	ND	ND	0.10	ND	ND	ND
	Sea	ND	ND	ND	ND	ND	0.15	ND	ND	ND
Australia	Pure	ND	ND	ND	ND	ND	ND	0.06	ND	ND
	Sea	ND	ND	ND	ND	ND	ND	0.20	ND	ND

In the Soil Contamination Countermeasures Law, promulgated on May 29 2002, designated areas are specified in which measures such as the removal of pollution (restricted access, covering of soil, paving (in the case of direct ingestion), containment of contaminated soil, cleaning etc.) are necessary. These designations apply to soil which does not satisfy the criteria shown in Table 1.4.

The dissolution criterion is equivalent to the reference values for the environmental quality standards for soil. Because of this, when these reference values of environmental quality standards for soil are used in the safety evaluation for the effective use of coal ash, it is not a designated area according to the Soil Contamination Countermeasures Law. However, for other reference values attention must be paid to the relationship between future soil contamination countermeasures laws and the case of setting higher values than the values set out already. It should be noted that the content standards for coal ash from coal fired power plants are sufficiently below the reference values.

Table 1.4 Specified criteria for hazardous substances (heavy metals, etc.)<sup>6)</sup>

Type	Elution standard	Content standard
Cadmium	Less than 0.01mg/ltr	Less than 150mg/ltr
Lead	Less than 0.01mg/ltr	Less than 150mg/ltr
Hexavalent chromium	Less than 0.05mg/ltr	Less than 250mg/ltr
Arsenic	Less than 0.01mg/ltr	Less than 150mg/ltr
Total mercury	Less than 0.0005mg/ltr	Less than 15mg/ltr
Selenium	Less than 0.01mg/ltr	Less than 150mg/ltr
Flourine	Less than 0.8mg/ltr	Less than 4,000mg/ltr
Boron	Less than 1mg/ltr	Less than 4,000mg/ltr

## 1.5 Literature review

### 1.5.1 Physical properties

#### 1) Particle density

Clinker ash has been found<sup>1)2)7)-11)</sup> to have a particle density of between 1.9-2.6g/cm<sup>3</sup>, which compared with typical natural soils, which have a particle density in the region of 2.6-2.8g/cm<sup>3</sup>, makes clinker ash a relatively light material.

#### 2) Particle distribution

Clinker ash has an intended maximum particle diameter of 2cm, and so as shown in Figure 1.9 there is large sand and gravel content and a wide range of particle diameters<sup>1)</sup>. Also, for use as a road material, particle distribution curves were taken before and after corrected CBR tests. In comparing these curves, as shown in Figure 1.10, it can be identified that clinker ash is a material in which particle breakage occurs.



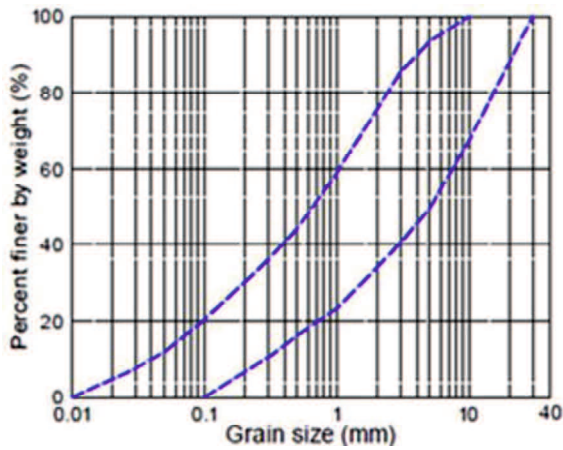


Figure 1.9 Particle distribution curves<sup>12)</sup>

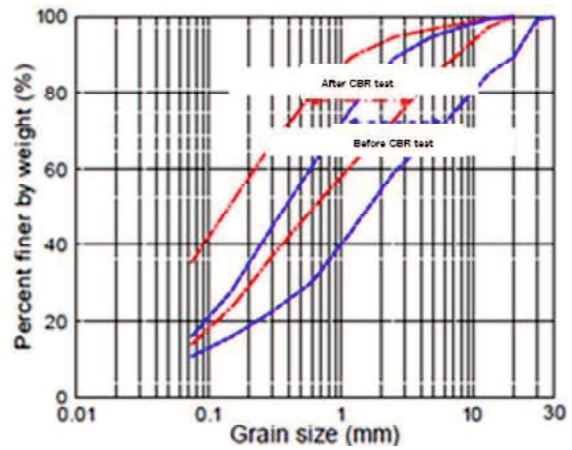


Figure 1.10 Particle distribution curves before and after road surface loading<sup>12)</sup>

### 3) Maximum and minimum density

The maximum density  $\rho_{dmax}$  and minimum density  $\rho_{dmin}$  were found to be in the regions of  $0.83 \pm 0.17 \text{g/cm}^3$  and  $0.67 \pm 0.13 \text{g/cm}^3$  respectively<sup>7)</sup>. A correlation between the maximum and minimum density also exists, and is calculated as follows:

$$\rho_{dmax} = 1.22\rho_{dmin} + 0.01 \quad (1.1)$$

### 4) Specific surface area

The specific surface area of clinker ash is in the region of  $3.8\text{-}4.5 \text{m}^2/\text{g}$  and is around 4 to 5 times larger than that of Masado, shown in Table 1.5.

Table 1.5 Specific surface area<sup>1)</sup>

Type	Diameter mm	Specific Surface Area m <sup>2</sup> /g
Clinker Ash	1	3.76
	2~3	4.54
Granite	—	0.21
Masado	—	0.94

#### 5) Water retention

Available water capacity tests were performed by the Environmental Technology Association and Japan Fly Ash Association on loose and dense clinker ash, as well as Masado and course soil. The available water content for each is shown in Table 1.6. The available water content is a percentage of how much moisture in a soil can be used efficiently by plants, with a higher value meaning higher water retention. As can be seen, clinker ash has high water retention. It can be thought that this is due to the porous nature of the particles, with surface pores connecting to the inside of the particle, as will be shown in Chapter 2.

Table 1.6 Available water capacity test results for clinker ash and general soil<sup>1)</sup>

	Clinker Ash (Dense)	Clinker Ash (Loose)	Masado	Coarse
Available Water Content (%)	9.4	5.8	4.0	2.0~3.0

## 1.5.2 Mechanical properties

#### 1) Compaction characteristics

Results from compaction tests on clinker ash performed by the Environmental Technology Association and Japan Fly Ash Association are shown in Figure 1.11. As can be seen, the maximum dry density of clinker ash is relatively small compared with typical sandy soil, and the optimum water

content is quite high. Also, the results from other researchers are given in Table 1.7, and similar trends can be observed.

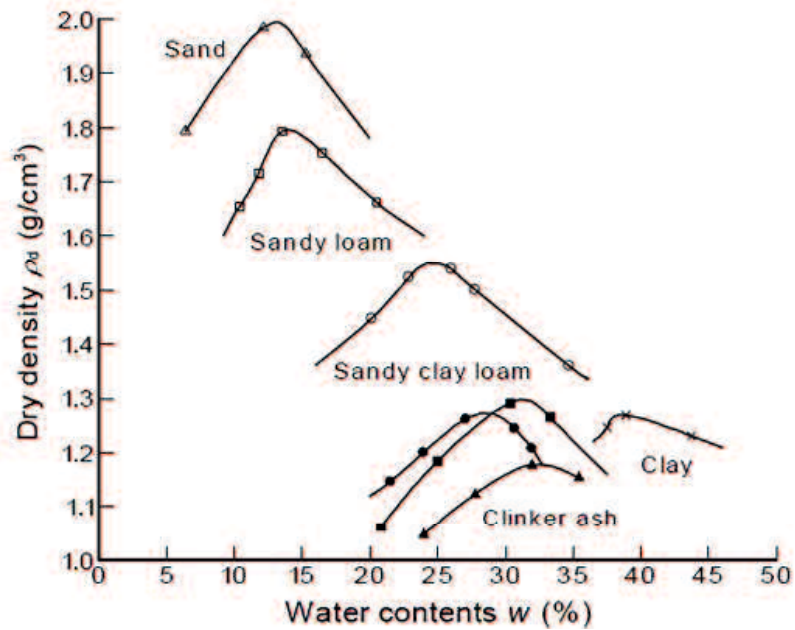


Figure 1.11 Compaction curves<sup>1)</sup>

Table 1.7 Compaction test results

	Natural Water Content %	Maximum Dry Density g/cm <sup>3</sup>	Optimum Water Content %
Environmental Technology Association/Japan Fly Ash Association <sup>1)</sup>	16.2	1.29	28.2
	17.4	1.29	27.2
	18.5	1.21	30.4
	15.9	1.502	18.0
	21.8	1.254	26.1
	26.2	1.151	32.2
	20.4	1.248	28.5
Japan Regional Development Corporation <sup>13)</sup>	-	1.385	21.3
	-	1.04	33
	-	0.88	32
Tori/Kawamura <sup>14)</sup>	-	0.925	51.7
	-	1.082	31.3

## 2) Monotonic shear characteristics

Due to clinker ash particles being crushable in nature, the internal friction angle decreases with increasing compression stress. The shear strength of clinker ash investigated by various researchers is shown in Table 1.8. As the strength properties of clinker ash vary by sample, there is some deviation in the results as different researchers use different samples and different test conditions, and as such the complete strength characteristics of clinker ash are not fully known.

Table 1.8 Monotonic shear strength

	Cohesion $c$ (kPa)	Internal Friction Angle $\Phi$ (°)	Conditions
Takahasi/Tezuka <sup>15)</sup>	201±50	46.6±8.5	Simple Shear Test ( $D_r=65\%, \sigma_c'=98\text{kPa}$ )
Ikeda/Sumikawa <sup>16)</sup>	0	37.4	CD Triaxial Compression Test ( $D_c=90\%$ )
Ogawa/Kawaguchi <sup>17)</sup>	9	36.7	CD Triaxial Compression Test (Density Unknown)
Naemura/Ono <sup>10)</sup>	39-108	29-33	Triaxial Compression Test (Density Unknown)

## 3) Permeability characteristics

Coefficients of permeability for clinker ash investigated by various researchers are shown in Table 1.9. According to the Environmental Technology Association/Japan Fly Ash Association, the coefficient of permeability for clinker ash is almost the same as that of sand.

Table 1.9 Coefficient of permeability

	Dry Density $\text{g/cm}^3$	Coefficient of Permeability $\text{cm/s}$
Environmental Technology Association/Japan Fly Ash Association <sup>1)</sup>	1.23	$3.2 \times 10^{-2}$
	1.20	$3.4 \times 10^{-2}$
	1.14	$3.2 \times 10^{-2}$
Ikeda/Sumikawa <sup>16)</sup>	Unknown ( $D_c=90\%$ )	$8.75 \times 10^{-3}$
Ogawa/Kawaguchi <sup>17)</sup>	Unknown	$7.2 \times 10^{-3}$

### 1.5.3 Chemical composition

#### 1) Chemical composition

The Environmental Technology Association and Japan Fly Ash Association found that, based on data from the Ministry of Natural Resources and Energy<sup>18)</sup>, there were slight differences in the chemical composition of coal ash, depending on the type of coal it was from. However, around 70%-80% of the chemical composition was made up of silicon dioxide (SiO<sub>2</sub>) and aluminum oxide (Al<sub>2</sub>O<sub>3</sub>), with trace elements of oxides such as FeO<sub>3</sub>, CaO, SO<sub>3</sub>, Na<sub>2</sub>O and K<sub>2</sub>O also being reported (refer to Table 1.10). Also, from these results the JSCE Energy Committee<sup>2)</sup> stated that as the chemical composition is similar to clay, coal ash can be used in large amounts as a substitute to clay in cement material. Compared with slag the CaO content is exceptionally small, and so it can be understood that it is a material which is difficult to self-cure.

Table 1.10 Chemical composition content of coal ash (%)

Chemical Composition	Domestic Coal <sup>18)</sup>	Foreign Coal <sup>18)</sup>	Mountain Soil <sup>18)</sup>	Clay (Japan) <sup>18)</sup>	Blast Furnace Slag <sup>18)</sup>	Granulated Slag <sup>19)</sup>
Si <sub>2</sub>	50-55	40-75	59.6	60-75	33.4	30-36
Al <sub>2</sub> O <sub>3</sub>	25-30	15-35	22.0	-	14.5	12-15
Fe <sub>2</sub> O <sub>3</sub>	4-7	2-20	-	5-8	0.4	-
CaO	4-7	1-10	0.4	10-25	41.0	40-43
K <sub>2</sub> O	0-1	1-4	-	-	-	-
MgO	1-2	1-3	0.8	-	6.0	5-8
Na <sub>2</sub> O	1-2	1-2	-	-	-	-
SO <sub>3</sub>	-	-	-	-	-	-
FeO	-	-	-	-	-	0-1
S	-	-	-	-	-	0-1

The chemical composition of clinker ash has been investigated by various researchers and the results are shown in Table 1.11. It can be seen that there are differences in the chemical compositions between research results and regions.

Table 1.11 Chemical composition content of clinker ash (%)

Chemical Composition	Takahashi/Tezuka <sup>15)</sup>	Tori/Kawamura <sup>14)</sup>	Kito/Yoneda <sup>20)</sup>						
			Okinawa	Kyushu	Shikoku	Chugoku	Chubu	Tohoku	Hokuriku
SiO <sub>2</sub>	55-66	53.1	68.3	61.2	57.9	62.7	55.9	62.0	54.2
Al <sub>2</sub> O <sub>3</sub>	16-26	22.9	25.3	21.6	24.5	23.6	25.7	23.6	26.5
Fe <sub>2</sub> O <sub>3</sub>	2.4-7.6	6.8	2.2	8.3	10.1	7.0	10.2	6.2	9.9
CaO	0.6-4.6	3.9	0.7	5.6	2.6	3.5	3.8	4.7	4.6
K <sub>2</sub> O	-	1.1	0.3	0.8	0.7	1.0	1.5	0.8	2.1
MgO	0.5-1.5	1.6	0.6	1.3	0.6	1.2	1.5	1.1	0.9
Na <sub>2</sub> O	-	2.1	0.8	0.0	0.0	0.0	0.0	0.0	0.0
SO <sub>3</sub>	-	0.1	0.0	0.0	1.6	0.0	0.0	0.0	0.0

## 2) Heavy metal content

Due to clinker ash coming from coal which is formed from different minerals and mixed in rocks and clay, there is the possibility that depending on where the coal is from there may be trace elements of heavy metals such as total mercury, cadmium, lead and arsenic.

The Ministry of Land, Infrastructure and Transport, Tohoku Regional Development Bureau have carried out tests using a mixture of unsuitable soil and clinker ash as a fill material. At that time dissolution tests were also performed, the results of this are shown in Table 1.12. From these results, we can see that for the test results for “clinker alone”, it satisfies all of the environmental quality standards for soils.

Table 1.12 Dissolution test results (mg/L)<sup>21)</sup>

Type	Environmental Quality Standards for Soil	Only Clinker Ash	Only Unsuitable Soil	Mixture (5:5)
Cadmium	<0.01	<0.0005	<0.0005	<0.0005
Lead	<0.01	<0.001	0.003	<0.01
Hexavalent Chromium	<0.05	<0.005	<0.005	<0.005
Arsenic	<0.01	<0.001	0.002	<0.001
Total Mercury	<0.0005	<0.0005	<0.0005	<0.0005
Selenium	<0.01	<0.001	<0.002	<0.001
Flourine	<0.8	0.2	-	<0.1
Boron	<1	0.04	-	0.03

### 3) Hydrogen ion concentration

According to the Japan Fly Ash Association, Japan Institute of Country-ology and Engineering <sup>12)</sup>, the hydrogen ion concentration is in the region of 8.2 to 10.8, and according to the JSCE Energy Committee<sup>2)</sup> it is, in general, about  $9 \pm 1.5$ . Therefore, it can be understood that clinker ash is slightly alkaline.

## **1.6 Objective and structure of this paper**

### **1.6.1 Objective of paper**

The objective of this paper is to investigate the material properties and shear characteristics of clinker ash. Clinker ash is an artificial byproduct of coal incineration, and the incineration and forming processes lead to clinker ash having light, porous particles with angular and complex shapes. The properties of clinker ash vary not only from power plant to power plant, but also change over time even with clinker ash from the same location. Therefore, in order to get a better range of results and understanding of the behaviour of clinker ash, samples have been taken from 6 power plants across western Japan. The material properties of each sample of clinker ash, along with the particle properties such as shape and strength, are first thoroughly investigated. After this, the shear characteristics of clinker ash are investigated through a wide range of experiments including triaxial compression tests, bender element tests, cyclic liquefaction tests and dynamic deformation tests. These tests are performed under various conditions such as differing densities of the specimen and confining pressures, in order to also investigate the influence of such conditions on the shear behaviour of coal ash. Through investigation of both the material properties and shear characteristics it is hoped that relationships can be found in order to explain the shear behaviour of clinker ash.

## **1.6.2 Structure of paper**

This paper is made up of the following chapters:

Chapter 1 Introduction

Chapter 2 Material properties of clinker ash

Chapter 3 Static shear characteristics of clinker ash

Chapter 4 Dynamic shear characteristics of clinker ash

Chapter 5 Conclusions and future research

In Chapter 1, the production process and basic characteristics of coal ash are given, along with an outline of the changes in amount of production and amount being put to effective use and the necessity to promote the effective use of coal ash is also given. Also, the environmental impact and laws relating to it for clinker ash, which is designated as industrial waste, are looked into. A review of literature is also given in which results of research carried out thus far regarding the physical, dynamic, and chemical properties of clinker ash are given.

In Chapter 2, taking into consideration the fact that clinker ash particles are artificially produced, investigation into particle characteristics was carried out in order to evaluate the shape and single particle strength. Also, in order to handle clinker ash as a ground material, the same kind of physical and dynamic experiments were performed on natural sands and the differences were compared in order to investigate the features of clinker ash.

In Chapter 3, the static shear characteristics of the 6 clinker ash samples are investigated using monotonic triaxial compression tests with varying degrees of compaction and confining pressures. These properties are then evaluated to see if a relationship could be found to the particle properties such as shape and strength. An equation is also proposed which can estimate the peak strength of



clinker ash samples.

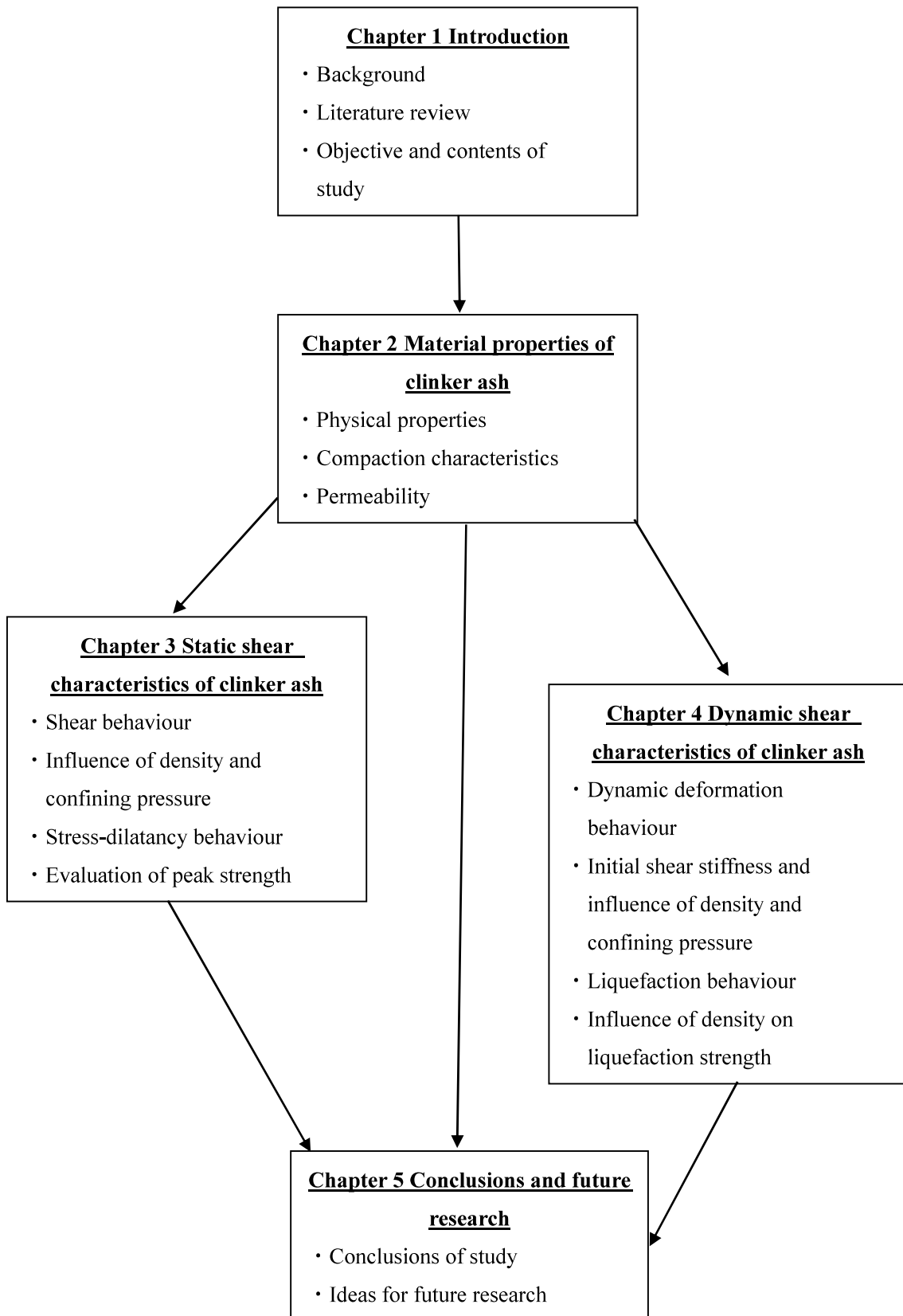
In Chapter 4, the dynamic shear characteristics of the clinker ash samples are investigated through dynamic deformation tests, bender element tests and cyclic triaxial liquefaction tests and these too are evaluated.

In Chapter 5, the conclusions of this research are given. Recommendations are also made for future research.

## **1.7 Previous group research and innovation of this study**

Previous research from our group has mainly focused on loose state specimens of clinker ash taken from the same power plants as the samples used in the current research. In this research, a range of densities from loose to very dense are investigated so that the influence of change in degree of compaction on the shear behaviour of the clinker ash samples can also be investigated. Although the properties of clinker ash vary from sample to sample, the amount of tests performed in this research can give an understanding of clinker ash properties and characteristics as a whole. A method for the prediction of the peak shear strength eliminates the need for numerous experiments on new clinker ash samples and various static and dynamic characteristics and behaviour of the clinker ash samples are made clear from this research.

### Flowchart of this study



## References

- 1) Environmental Technology Association, Japan Fly Ash Association (2005) Coal Ash Handbook.
- 2) JSCE Energy Committee (2003) Effective utilization technology of coal ash – Toward a recycling-orientated society.
- 3) Japan Coal Energy Center (2006) Coal to be used cleanly (Aiming at a world where economics and the environment are compatible).
- 4) Japan Coal Energy Center (2011) World Coal Report 4.
- 5) Japan Coal Energy Center (2011) JCOAL Journal 18.
- 6) Ministry of Environment (2009) Annual Report on the Environment, the Sound Material-Cycle Society and Biodiversity in Japan.
- 7) Takahashi K, Izutsu Y. (2005) Effective geotechnical application of construction and industrial byproducts (8) Coal Ash, *Soils and Foundations*, 53, 43-52.
- 8) Takahashi K, Umehara Y, Tezuka M, Okumura I, Ono S. (1995) Soil properties of electric coal ash (Part 1) - Physical and chemical properties of newly-formed ash, *Outline of the 30th Geotechnical Research Presentation Meeting*, 757-760.
- 9) Sunaga M, Yamada M, Sano H, Ieda, H. (1988) Overview of usage of coal ash (By-product of thermal power plants) in earth structures and future prospects, *Journal of Japan Railroad Facilities Association*, 197-200.
- 10) Naemura S, Onodera S. (1990) Embankments using coal ash, *Foundation Engineering*, 18(12), 59-67.
- 11) Ikeda H, Takahashi M, Hayasaka Y, Mori K. (2000) Application of clinker ash in frost inhibiting layers, *The 55th Annual Scientific Lecture by the Japan Society of Civil Engineers V*, 57-58.
- 12) Japan Fly Ash Association, Japan Institute of Country-ology and Engineering (1989) Research

report on the use of coal ash for road paving.

13) Regional Development Assistance Corporation (1984) Survey report on landfill of coal ash.

14) Torii K, Kawamura M, Hasaba S. (1986) A fundamental study on reaction products and strength of compacted coal ashes, *Journal of Japan Society of Civil Engineers*, 5(372), 65-74.

15) Takahashi K, Tezuka M, Imashio H, Kobayashi M, Asada H. (1995) Soil properties of electric coal ash (Part 2) - Mechanical properties and reactivity of newly formed ash, *Outline of the 30th Geotechnical Research Presentation Meeting*, 757-760.

16) Ikeda T, Sumikawa T, Ano T. (2001) Effective utilization of clinker ash as Terre Armee embankment, *The 56th Annual Scientific Lecture by the Japan Society of Civil Engineers*, 410-411.

17) Ogawa N, Kawaguchi K, Okano M, Amano M. (1992) Design and construction of reinforced earth wall using clinker ash, *27th Geo Engineering Research Presentation*, 2461-2462.

18) Ministry of Natural Resources and Energy, Resources and Fuel (2003) Call Note.

19) Japan Construction Benefit Association (2006) Civil Engineering Design Manual.

20) Kito C, Yoneda T, Fujihara T, Okada T. (2005) Evaluation based on consistency limit after one year of bentonite press block using clinker ash, *Civil Engineering Society Annual Scientific Lecture*, 129-130.

21) Ministry of Land, Infrastructure and Transport, Tohoku Regional Development Bureau, Tohoku Technical Office (2003) Coal ash in road embankments and guidelines for use of earth from construction (clinker ash version).

## **Chapter 2 Material properties of clinker ash**

### **2.1 Outline**

Behaviour of ground depends on various factors such as stress history, density, water content and stress state. Also, there are many types of soils that exist in nature, and the physical and mechanical properties of these also vary. Furthermore, due to the difference in stress regions particle breakage can occur, and this in turn can make it difficult to predict the strength and deformation behaviour of the ground. In the Chugoku region of Japan, “Masado”, which comes from weathered granite-type rocks, has long been used as a ground material in embankments and fills. In the Kyushu region, the non-welded pyroclastic flow deposits “Shirasu” are widespread, and the opportunities to use it as a ground material or fill material have been increasing. However, when investigating the ground engineering properties and engineering behaviour of these materials using generally used soil tests, it may not always be possible to clarify results completely. There have also been many occurrences of engineering-type problems such as slope failure due to rainfall and liquefaction, and so they are designated as special soils by the Geotechnical Society. One of the reasons for this is particle breakage occurring, and with crushable materials such as these it is extremely important to understand that they must be handled very carefully.

Due to the production process of clinker ash in which it is crushed in a grinder after being rapidly cooled at the coal fired power plants, when observing the particles, the first thing to be noticed is that the particle shape is very complex. For this reason, when the clinker ash becomes aggregate it can be imagined that the interlocking between particles has an influence on shear strength. In addition, in some cases the angularities of the particle can be easily broken simply by pressure from the fingers

and so clinker ash must be handled as a crushable material. Further, when clinker ash particles are observed closely, it can be seen that the particles are very porous and breaking the particle shows many apertures inside the particle. This is due to the rapid cooling during production and it can be understood that clinker ash contains pores both on the surface and within the particle. It can be considered that these pores have a large influence on the ability for water retention and light-weight of clinker ash.

From the above, it can be thought that the porous nature, complex shape and crushability of clinker ash particles will have a large influence on the physical and mechanical properties for use as a ground material.

In section 2.2, the samples of clinker ash used in this research are introduced. In section 2.3, the physical properties such as particle density, particle distribution and maximum and minimum void ratio are made clear in order to grasp the basic physical characteristics of clinker ash. In section 2.4, building on clinker ash being a material that is artificially ground when produced, the particle characteristics are investigated through microscopic observation and calculation of a particle's roundness coefficient and aspect ratio, along with a series of single particle crushing tests being performed in order to quantitatively measure particle shape and strength. In section 2.5, compaction tests by tamping and saturated permeability tests are carried out in order to understand the mechanical properties of clinker ash. In section 2.6, the findings of this chapter are summarized. A table of the material properties for the clinker ash samples is provided in Appendix A.

## 2.2 Samples Used

Clinker ash taken from 6 power plants in western Japan, labelled CA-CF was gathered and used in this research. A representative observation of particles exterior and shape is shown in Figure 2.1. From the figure it can be seen that clinker ash particles have many pores. These pores are formed when the clinker ash particles fall from the hot incineration boiler (around 1,500°C) into a water tank below where they rapidly cool and harden. Because of this, as shown in Figure 2.2 there are pores connected to the surface as well as within the particle itself. Also, clinker ash particles have very angular surfaces due to the particles being crushed in a grinder to maximum diameters of around 2cm. These particle shape features can be thought to have a large influence on the physical and mechanical properties of aggregate clinker ash.



Figure 2.1 Observation of clinker ash

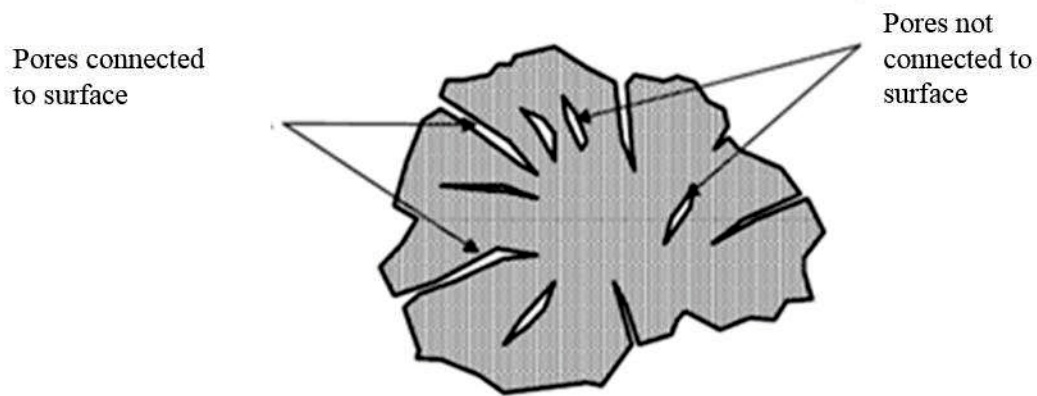


Figure 2.2 Conceptual diagram of clinker ash pores

The clinker ash is ground so that when it is to be transported from the power plant it is easier to handle. Although different power plants use different methods of transport, such as a conveyor -type or water pipe-type, the same kind of 2 drum-type grinder is used and so the particles which are produced all have relatively the same maximum diameter. However, the particle distribution of the clinker ash varies based on such factors as the performance of the boiler used and the type of coal.



## 2.3 Physical Properties

For reference, some results for samples previously obtained from the same power plants as those in this research are also shown. It can be seen that even from the same power plants, the physical properties of clinker ash can vary over time. This is most likely due to changes in equipment at the power plants, or the source of the coal being used itself.

### 2.3.1 Particle Density

Particle density tests were carried out following JIS A 1202:2009, soil particle density test method, on particles which passed through a 9.5mm sieve. As can be seen in Figure 2.3, the particle densities were found to be between 2.07-2.17g/cm<sup>3</sup>, which is a relatively low value. This is due to the porous nature of the particles.

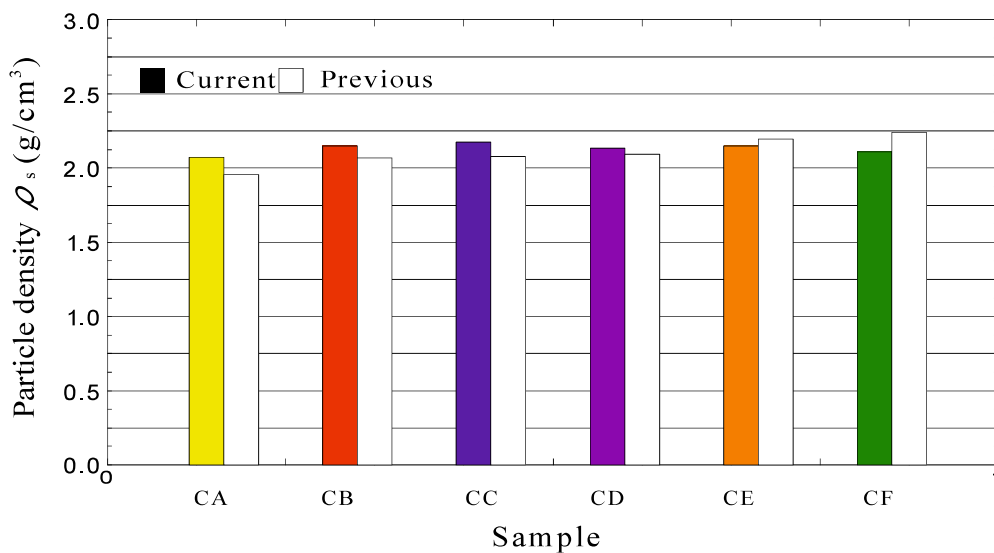


Figure 2.3 Particle density for each clinker ash sample

### 2.3.2 Particle Distribution

The particle distribution was found following JIS A 1204:2009, the soil particle distribution test method. Figure 2.4 shows the particle distributions of the 6 clinker ash types used in this research. The black lines indicate the range of results from 60 different clinker ash types taken from 15 power plants in Japan<sup>1)</sup>, and it can be seen that the particle distributions of the samples used in this research give a good representation of the particle distributions of clinker ash as a whole.

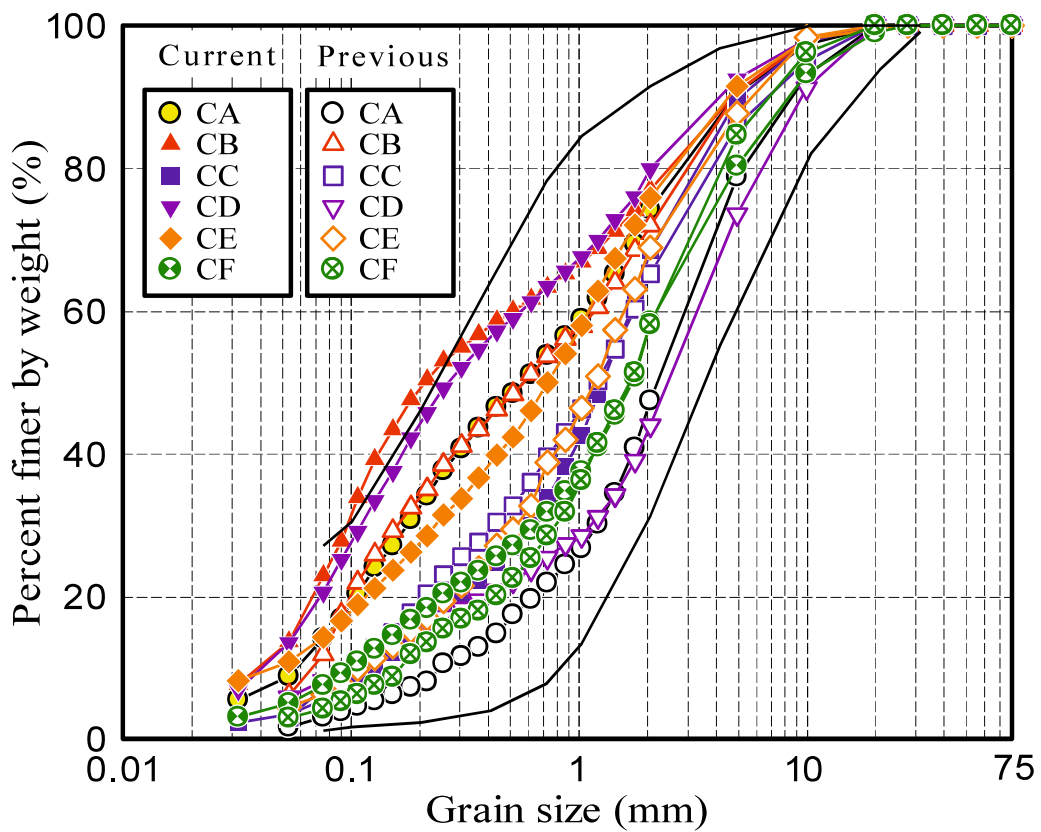


Figure 2.4 Particle distribution curves

The gravel content of the clinker ash samples used in this research was in the region of 19-43%, classifying it as a sandy or gravelly soil. The coefficient of uniformity  $U_c$  is between 12.5-26.7, which

shows that there is wide particle distribution.

### 2.3.3 Maximum and Minimum Density

As clinker ash contains particle sizes above 2mm, the tests were carried out following JGS 0162-2006<sup>2)</sup>, the maximum and minimum density of gravel test method. The maximum and minimum densities of the clinker ash samples were found and are displayed as maximum and minimum void ratios in Figure 2.5. Clinker ash displays relatively high maximum and minimum densities due to the porous nature of the particles, and the void space between the particles is increased due to the complex shapes of the particles.

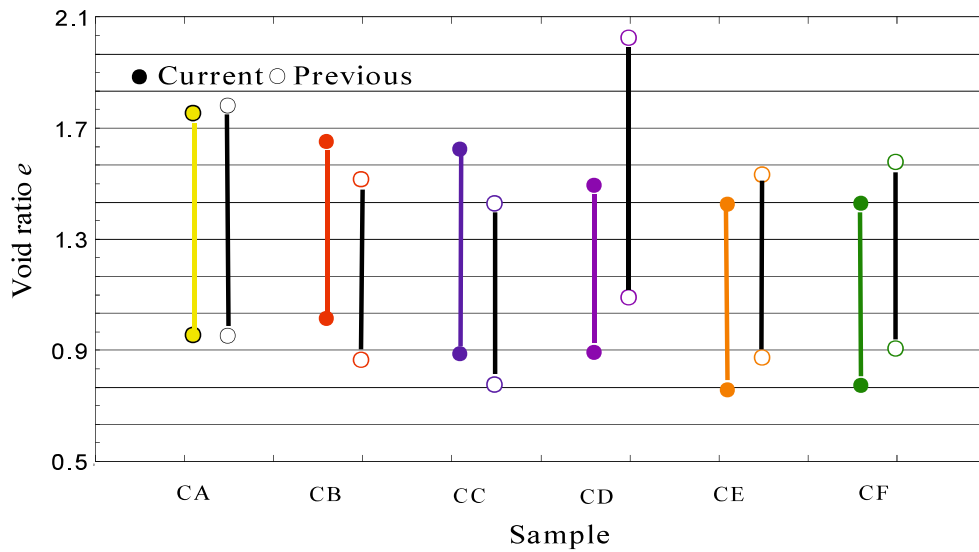


Figure 2.5 Maximum and minimum void ratios

## 2.4 Particle Characteristics

### 2.4.1 Particle Shape

Typical microscopic photographs of particles for each for each type of clinker ash are shown in Figures 2.6 (a)-(f). From the pictures, the porous nature of the particles can be clearly observed. The reasons for the porous particles and complex, angular particle shapes have been explained previously.

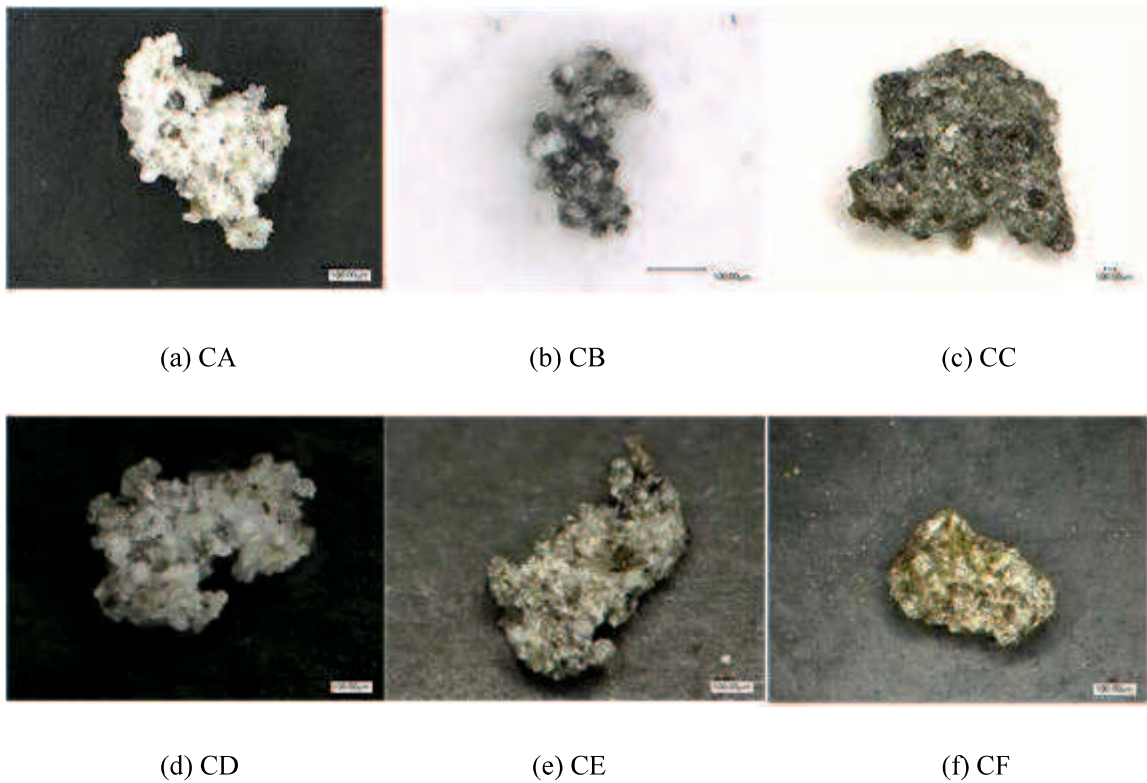


Figure 2.6 Observation of clinker ash particles

Clinker ash particles are very sharp and angular due to being produced in a grinder. Here, microscopic observation of particles has been performed using a 1.92-million-pixel camera at a resolution of 1600\*1200. The sizes of the observed particles are those with the average particle size

$d_{50}$ . It has been proposed<sup>3)</sup> that taking 20 particles at random from a sample and then taking the average of the results is sufficient in representing the shape characteristic of a sample. Based on this, in this research 30 particles from each sample were tested. There are various methods for expressing particle shape, although in this research the roundness coefficient  $R_c$  and aspect ratio  $A_r$ <sup>4)</sup> was used. The value for the roundness coefficient is calculated as follows:

$$R_c = \frac{L^2}{4\pi A} \quad (2.1)$$

Here,  $L$  is the circumference of the particle and  $A$  is the cross-sectional area. A roundness coefficient closer to 1 indicates that the particle shape is closer to a circle, with higher values indicating more angularity. The aspect ratio is calculated using the following equation.

$$A_r = \frac{b}{a} \quad (b \geq a) \quad (2.2)$$

Here,  $b$  is the length of the longest dimension of the particle and  $a$  is the length of the shortest dimension of the particle. A higher value for aspect ratio indicates a more elongated particle. Figure 2.7 shows the relationship between roundness coefficient and aspect ratio for the clinker ash samples used.

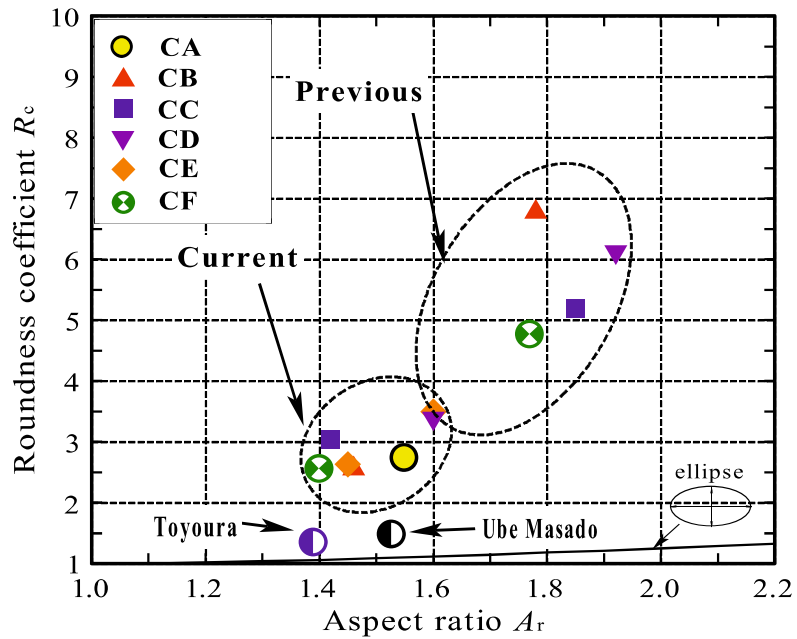


Figure 2.7 Relationship between roundness coefficient and aspect ratio

As can be seen from the figure the roundness coefficient of clinker ash is relatively high compared with natural sands, an indication of the complex particle shapes. It can be presumed that differences in  $R_c$  and  $A_r$  of the clinker ash samples could be due the type of coal used, the method of incineration used and the process of formation in the water tanks before crushing in the grinder.

#### 2.4.2 Single Particle Crushing Tests

As the particles of clinker ash are artificially formed it is important to understand the strength characteristics in order to compare with natural soils. Therefore, a series of single particle crushing tests<sup>3)4)</sup> were performed in order to investigate the particle strength of clinker ash and other natural sands.

A picture of the single particle crushing test equipment is shown in Figure 2.8. In the test, a particle is placed in its most stable state before a load is applied from above in order to cause particle crushing.

The test covers most of the particle distribution and 20 particles were taken from each range of 0.5-1.0mm, 1.0-2.0mm, 2.0-4.75mm, for a total of 60 particles per sample.

The crushing patterns based on results from single particle crushing tests on natural sand are shown as the four patterns in Figure 2.9. In general particles with crushing behaviour close to pattern 1 have higher strength and those that exhibit crushing behaviour similar to pattern 4 have low strength. The crushing stress  $\sigma_f$  was calculated using the following equation:

$$\sigma_f = \frac{F_f}{d_0^2} \quad (2.3)$$

Here,  $F_f$  is the load at point of initial crushing and  $d_0^2$  is the initial particle height (initial diameter).



Figure 2.8 Particle crushing test equipment

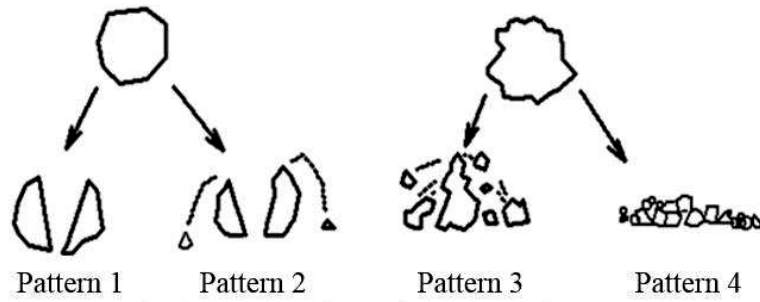


Figure 2.9 Breakage patterns

Figure 2.10 shows representative crushing strength and displacement relationships for the breakage patterns. The patterns do not differ by type of coal so much as by colour of particle. The initial strength was taken at the point at which initial crushing occurs, as highlighted by red circles.

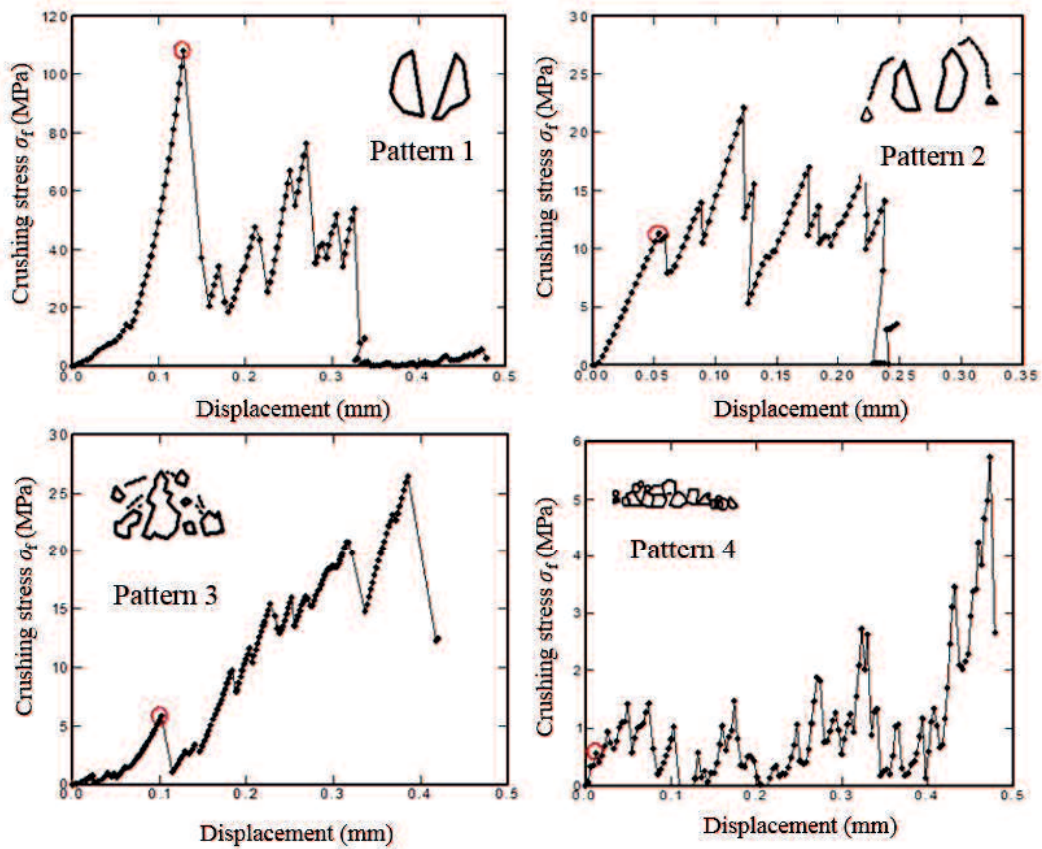


Figure 2.10 Strength-displacement relationships for each pattern



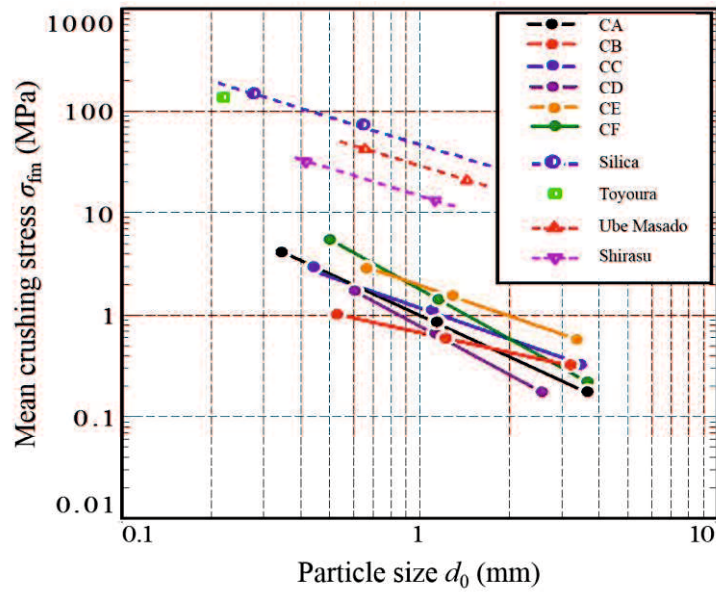


Figure 2.11 Mean crushing stress-particle size relationships for clinker ash and natural sands

Table 2.1 Average crushing stress  $\sigma_{fm}$  (MPa)

Sample	CA	CB	CC	CD	CE	CF
$\sigma_f$ (MPa)	4.27	1.99	2.56	1.04	4.75	3.12

Figure 2.11 shows the relationship between particle crushing stress and particle size, with Table 2.1 showing the values for average crushing stress for each clinker ash sample. From the picture, it can be seen that the particle crushing stress at the same particle diameter decreases in the order of Silica, Ube Masado, Shirasu and then clinker ash. Shirasu is formed from pyroclastic flow deposit and is relatively porous when compared with other natural sands, which is why it also displays lower particle crushing strength among other natural sands. It can be seen that there is a trend that a larger value for initial diameter gives a lower particle crushing strength. For natural sand, it has previously been shown<sup>3)5)</sup> that single particle crushing strength is influenced by particle diameter. For clinker ash, as it is forcibly broken by a grinder there are large deviations in the results, however for a certain

sample there is the same trend of crushing strength becoming smaller with increasing particle diameter. It can be seen that the crushing strength is around 1/5-1/10 smaller when compared with natural sands and is an easily crushable material.

## 2.5 Compaction and Permeability Characteristics

### 2.5.1 Compaction Characteristics

Compaction tests were carried out following JIS A 1210:2009, compaction of soil through tamping test method. The test conditions are shown in Table 2.2. Figure 2.12 shows the compaction curves gained from the tests performed on the clinker ash samples. As can be seen in the figure, the compaction curves do not give such a clear peak, as with Ube Masado, and give a smoother curve. This is due to the complex shapes of the clinker ash particles, which do not rearrange easily during compaction. As such it can be thought that the regulation of the water content of clinker ash during compaction is not so important.

Table 2.2 Test conditions for compaction test by tamping

Name	Rammer Weight	Drop Height	Mold Diameter	Mold Volume	Layers	Tamping per Layer	Specimen Preparation
A-b	2.5kg	30cm	10cm	100cm <sup>3</sup>	3	25	Drained Cyclic and Dry Method

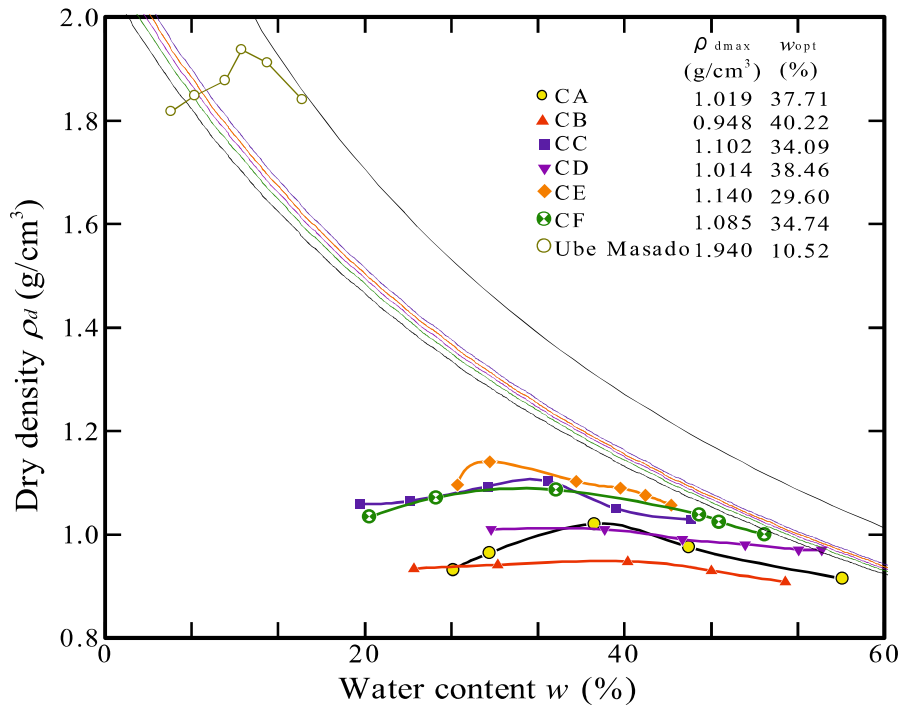
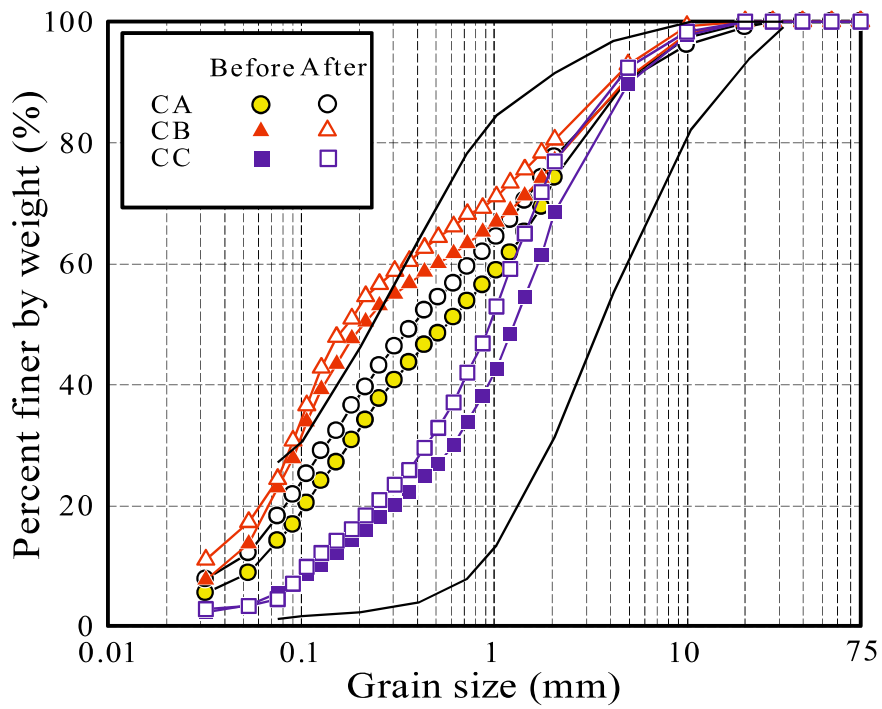
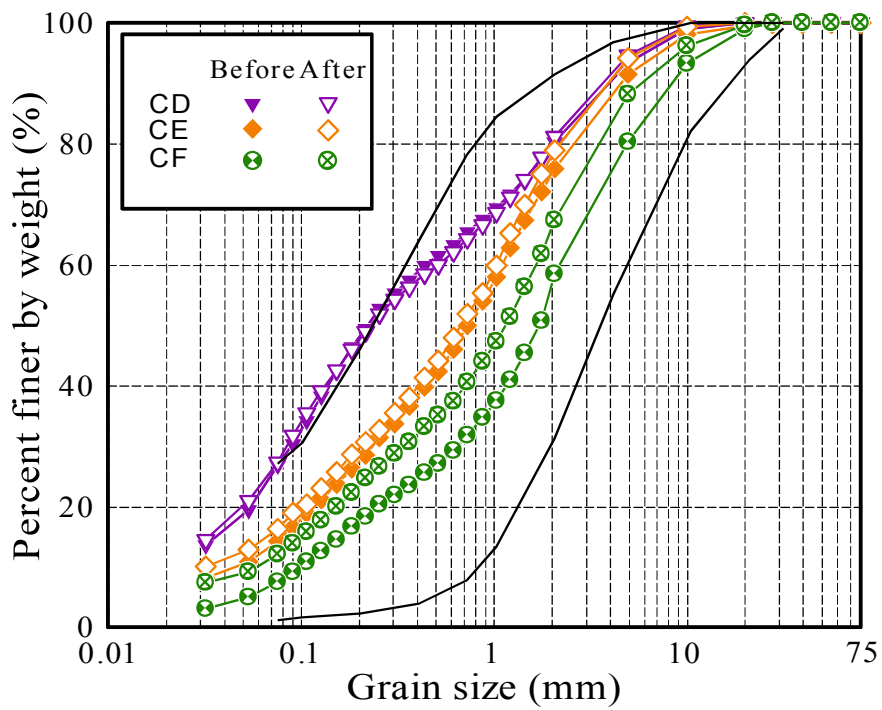


Figure 2.12 Compaction curves for clinker ash and Ube Masado

As there is no unified definition for the relative density  $D_r$  of clinker ash, and as it is to be used as a fill material, where the density is managed by degree of compaction,  $D_c$ , the densities of specimens used in this research are also defined by  $D_c$ . Here,  $D_c$  is defined as the dry density  $\rho_d$  divided by the maximum dry density  $\rho_{dmax}$  obtained from the above compaction curves.



(a) CA-CC



(a) CD-CF

Figure 2.13 Particle distribution curves before and after compaction tests

Figures 2.13 (a)-(b) show the particle distribution curves for each sample of clinker ash before and after compaction tests. As can be seen, there is an increase in fines content after the tests have been performed, showing that particle breakage has occurred.

## 2.5.2 Permeability Characteristics

Saturation of a specimen is an important factor for permeability tests as air trapped in the voids of the particles means that water can no longer move through the entire pore space but only the remaining area occupied by water, which leads to a reduced result of permeability. Due to the porous nature of clinker ash particles, it is a relatively difficult material to saturate, and as such it is first placed in de-aired water in a vacuum chamber for between 2-3 days in order to remove as much of the air as possible, and is then inserted into a mold with a diameter of 5cm and height of 20cm using the water pluviation method. The specimens were prepared using intended degrees of compaction  $D_c=75\%-90\%$  and the tests were carried out under a low confining pressure  $\sigma_c'=10\text{kPa}$  in order to keep the specimen stable.

The test conditions for the tests performed are given in Table 2.3.

Table 2.3 Test conditions for permeability tests

Sample	$D_c$ (%)	$\sigma_c'$ (kPa)	Sample	$D_c$ (%)	$\sigma_c'$ (kPa)	
CA	80	10	CD	80	10	
	85			86		
	88			89		
CB	81		CE	78		
	85			84		
	90			86		
CC	74			CF		80
	86					83
	83					89

The tests were carried out using the apparatus shown in Figure 2.14. The test method is as follows:

1) A rubber sleeve is placed around a base porous stone and secured to it by applying three tightly fastened wires.

2) A metal mold is placed around the sleeve in order to keep it in position during insertion of the sample, and is secured in place using two screws.

3) The sample is inserted into the sleeve in even layers to the desired degree of compaction, and care is taken to ensure as little air as possible enters the sample.

4) The metal mold is removed before an upper cap containing a porous stone is placed inside the top of the rubber sleeve and again secured by applying three tightly fastened wires.

5) A chamber is placed around the specimen and secured using screws in order to allow a confining pressure to be applied.

6) A tube from the water tank is connected to the bottom outlet of the apparatus and a receiver is connected to the top in order to collect any water which comes out.

7) The water tank is adjusted to a height to give the maximum hydraulic gradient, and time is given to allow a steady flow to be achieved.

8) Once a steady flow has been reached, water is collected in the receiver for 5 minutes. After 5 minutes, the amount of water is measured and the test is repeated 2 more times

9) Step 8) is repeated for hydraulic gradients between 0.1-0.7

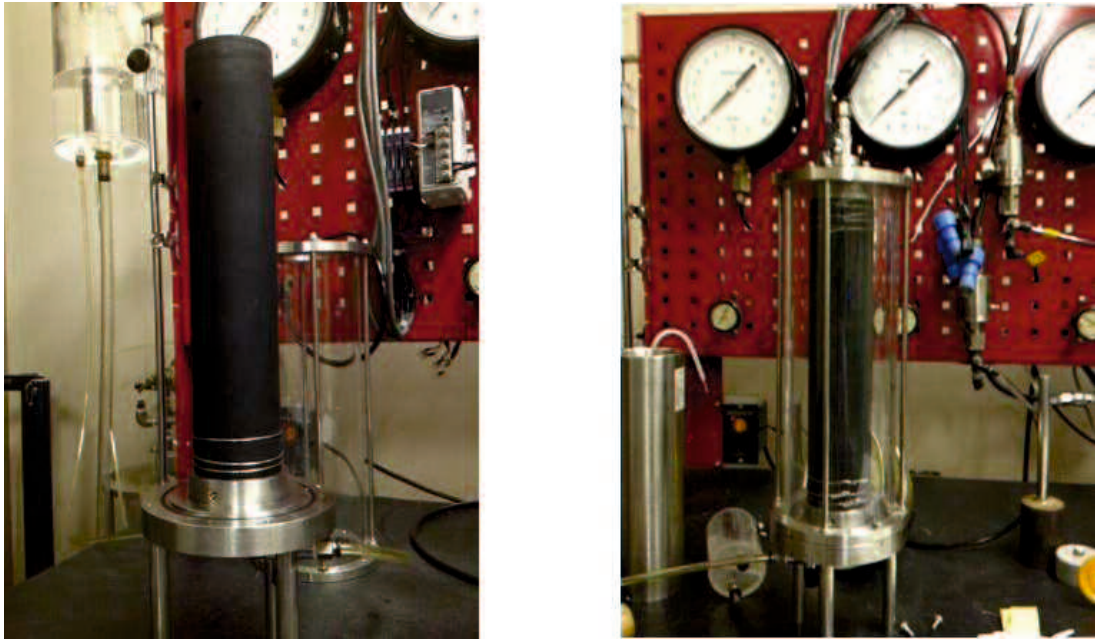


Figure 2.14 Permeability test apparatus

The coefficient of permeability  $k$  was calculated using the following equation:

$$k = \frac{QL}{Aht} \quad (2.4)$$

where,  $k$  is the coefficient of permeability,  $Q$  is the volume of water collected,  $L$  is the length of the specimen,  $A$  is the cross-sectional area of the specimen and  $t$  is the time taken during the test.

The tests were conducted between hydraulic gradients of 0.1-0.7 as it was hoped that the region of laminar flow for the clinker ash samples could be found. It is necessary to find the region of laminar flow as this is where it is supposed that the water flows at a uniform velocity and should not disturb the sample.

Kozeny<sup>6)</sup> proposed that the coefficient of permeability  $k$  correlated to the void ratio function  $e^3/1+e$ , as shown in Figure 2.15.

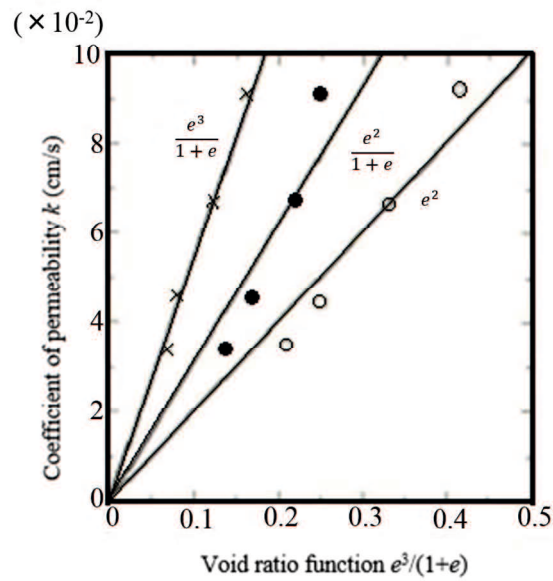


Figure 2.15 Relationship between coefficient of permeability and void ratio function<sup>6)</sup>

To investigate if this correlation existed with results gained from the permeability tests the coefficients of permeability were plotted against the void ratio  $e$  and the void ratio function  $e^3/1+e$ , as shown in Figures 2.16 and 2.17, respectively.

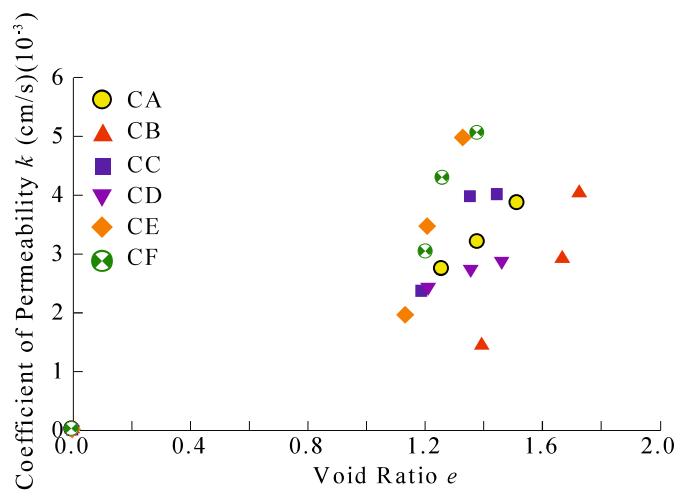


Figure 2.16 Relationship between coefficient of permeability and void ratio



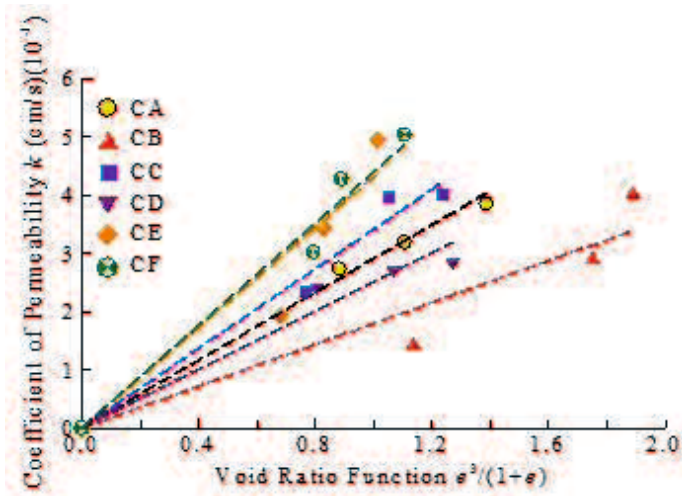


Figure 2.17 Relationship between coefficient of permeability and void ratio function

As can be seen from the above figures, the void ratio function  $e^3/1+e$  appears to correlate strongly with the coefficient of permeability  $k$ , and much more strongly than the void ratio  $e$ .

From this relationship, it was investigated to see if a shape factor for the clinker ash samples could be calculated using an adaptation of Taylor's<sup>7)</sup> equation, which is as follows:

$$k = CD_s^2 \frac{\gamma_w}{\eta} \frac{e^3}{1+e} \quad (2.5)$$

where  $k$  is the coefficient of permeability,  $D_s$  is the particle diameter,  $\gamma_w$  is the unit weight of water,  $\eta$  is the viscosity of water  $e$  is the void ratio and  $C$  is a shape factor.

In the case of clinker ash, which has a very wide particle distribution, it was found to not be very effective to use a particular particle diameter in calculating the shape factor. After investigation, it became clear that a parameter representing this wide particle distribution could give better results, and as such the coefficient of uniformity  $U_c$  was chosen.  $U_c$  is calculated using the following equation:

$$U_c = \frac{d_{60}}{d_{10}} \quad (2.6)$$

where  $d_{60}$  is the diameter that 60% of the sample is finer than and  $d_{10}$  is the diameter that 10% of the sample is finer than.

Also, the shape factor  $C$  was replaced with a new clinker shape factor  $C_T$ , to give:

$$k = C_T U_c \frac{\gamma_w}{\eta} \frac{e^3}{1+e} \quad (2.7)$$

From this equation, it was possible to calculate the clinker shape factor  $C_T$  using the results from the permeability tests. These values are shown in Table 2.4.

Table 2.4  $C_T$  values

	CA	CB	CC	CD	CE	CF
$C_T$ (cm <sup>2</sup> )	0.49	0.56	0.65	0.29	1.20	0.71

## 2.6 Summary

### 1) Physical Characteristics

Clinker ash displays relatively low particle density in the region of 2.07-2.17g/cm<sup>3</sup> due to the porous nature of the particles.

The gravel content of clinker ash lies in the region of 19-43%, classifying it as a sandy or gravelly soil. The coefficient of uniformity  $U_c$  is in the region of 12.5-26.7, giving it a wide particle distribution.

The maximum void ratio is between 1.42-1.75 and the minimum void ratio is between 0.75-1.0, displaying a relatively large value. This is due to the many pores in the clinker ash particles and also

the complex particle shapes.

## 2) Particle Characteristics

Due to the formation process of clinker ash, there are many pores both inside and on the surface of the particles.

As clinker ash is crushed in a grinder before transportation from the power plants, the particles have very complex and angular shapes, and display a roundness coefficient in the region of 2.55-3.39, which is relatively high when compared with natural soil.

The particle crushing strength of clinker ash is around 1/5-1/10 lower than natural sand, and as such indicates that clinker ash particles can easily suffer crushing. Also, as with natural sands, the crushing strength decreases with increase in particle diameter.

## 3) Mechanical Properties

The compaction curves of clinker ash give relatively smooth curves when compared with those of natural sands, and display relatively low maximum dry densities. Also, due to the particle strength being relatively low and the complex particle shape making the particles difficult to rearrange during compaction, clinker ash displays very low maximum dry density values of between 0.95-1.14g/cm<sup>3</sup>.

The coefficients of permeability  $k$  for the clinker ash samples exist within the range of 10<sup>-3</sup>cm/s and the relationship between the coefficient of permeability and the void ratio function can be used to calculate a clinker shape factor for the various samples of clinker ash, which gives a representation of the size and shapes of the whole particle distribution.

## References

- 1) Wakatsuki Y, Tanaka H, Uchida Y, Irie K, Hyodo M, Yoshimoto N (2007) Material characteristics of clinker ash and examination of applicability, *Japanese Geotechnical Journal*, 2(4), 271-285.
- 2) The Japanese Geotechnical Society (2009) Test method for minimum density and maximum density of gravel (JGS 0162-2009), *Method and Explanation of Ground Material Tests (Part 1 of 2)*, 198-221.
- 3) Yoshimura Y, Ogawa S (1993) A simple quantification method of grain shape of granular materials such as sand, *Journal of Japan Society of Civil Engineers*, 463(III-22), 95-103.
- 4) Kato F, Nakata Y, Hyodo M, Murata S (2001) Single particle crushing characteristics of ground materials, *Journal of Japan Society of Civil Engineers*, 673(III-54), 189-194.
- 5) Nakata Y, Kato Y, Hyodo M, Hyde A. F. L, Murata H. (2001) One dimensional compression behaviour of uniformly graded sand related to single particle crushing strength, *Soils and Foundations*, 41(2), 39-51.
- 6) Kozeny J. (1927) On the capillary conduction of water in soil, *Sitzungsber Akad. Wiss., Wien*, 136(2a), 271-306.
- 7) Taylor D. (1948) *Fundamentals of Soil Mechanics*. New York: Wiley, 161.

## **Chapter 3 Static shear characteristics of clinker ash**

### **3.1 Outline**

From previous research<sup>1)-3)</sup>, it has been found that it is possible to use clinker ash as a ground material in such applications such as embankments. In particular, it has been made clear that clinker ash possesses high shear and liquefaction strengths. However, in order to take advantage of clinker ash generated from many power plants and use it in broader applications, further research is necessary. When clinker ash is used in the field such as in embankments it is generally compacted to a high degree of compaction. However, due to the sharp particle shapes it is difficult to reproduce these conditions in laboratory tests as the particles can easily rip the gum membranes during compaction. As such, the shear strength characteristics of clinker ash at the same high levels of compaction as in the field are not yet fully clear.

### **3.2 Static shear characteristics from triaxial compression tests**

#### **3.2.1 Specimen preparation method and test conditions**

In order to ensure the sample was as close to a saturated condition as possible, it was first placed in de-aired water in a vacuum chamber for 2-3 days in order to remove as much air as possible. For specimens with intended degrees of compaction  $D_c=85\%$  and  $90\%$ , the sample was then inserted into a membrane inside a metal mold with a diameter of 10cm and a height of 20cm using the water pluvation method. For degrees of compaction of  $D_c=95\%$  or higher though, it proved problematic to

make the specimen in this way, as tamping of the sample to attain the desired degree of compaction could often lead to tearing of the membrane due to the sharp and angular clinker ash particles. Therefore, for higher degrees of compaction, a freezing method was used. The specimen was first prepared in a separate mold using a 2.5kg rammer dropped 24 times for each layer from a height of 30cm, repeated for a total of five layers in order to attain above  $1E_c$  as gained from compaction tests. The test conditions are shown in Table 3.1 and test data on clinker ash is given in Appendix B.

Table 3.1 Test conditions for triaxial compression tests

	$D_c$ (%)	$\sigma_c'$ (kPa)		$D_c$ (%)	$\sigma_c'$ (kPa)		$D_c$ (%)	$\sigma_c'$ (kPa)
CA	83	50	CA	88	100	CA	83	200
	88			88			87	
	97			98			99	
CB	88		CB	-		CB	86	
	91			93			93	
	103			100			100	
CC	84		CC	-		CC	83	
	-			-			-	
	100			103			104	
CD	85		CD	-		CD	85	
	92			91			-	
	99			100			100	
CE	85		CE	83		CE	-	
	88			86			90	
	100			100			98	
CF	85		CF	83		CF	-	
	89			92			-	
	100			97			100	
Ube Masado	84	Ube Masado	85	Ube Masado	84			
	98		97		97			

### 3.2.2 Testing apparatus and test method

Low pressure triaxial compression testing apparatus was used to carry out consolidated undrained triaxial compression tests. Figure 3.1 shows the testing apparatus used and the test method is as follows:

- 1) The specimen is placed in the membrane using the water pluviation method for lower degrees of compaction and the freezing method for higher degrees of compaction.
- 2) A cell is placed around the specimen and is then filled with water.
- 3) Pressure is changed from negative to positive to support the specimen.
- 4) If the freezing method has been used then the specimen is left for around an hour until thawing can be confirmed through passing of water.
- 5) Water is passed through the specimen.
- 6) Back pressure is applied to the specimen for an amount of time.
- 7) The B-value is measured, and if it is above 0.95 then consolidation begins.
- 8) Lateral pressure is increased to a predetermined value and the specimen is left until the volumetric change has become stable.
- 9) Shear is applied at a rate of 0.2%/min until an axial strain of 20%, at which the test is ended.
- 10) After the cell has been removed, the specimen is placed in an oven to dry, after which the dry weight of the specimen can be measured and the density calculated.

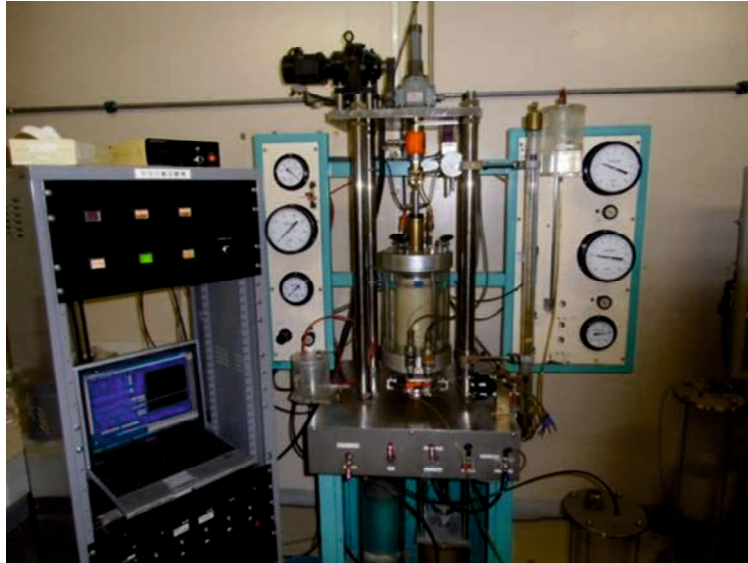


Figure 3.1 Static triaxial compression test equipment

The mean effective stress  $p'$  and deviator stress  $q$  were the stress parameters used, calculated as follows:

$$p' = \frac{\sigma_a' + 2\sigma_r'}{3} \quad (3.1)$$

$$q = \sigma_a' - \sigma_r' \quad (3.2)$$

Here,  $\sigma_a'$  is the mean effective stress in the axial direction and  $\sigma_r'$  is the mean effective stress in the radial direction. Volumetric strain  $\varepsilon_v$  and axial strain  $\varepsilon_a$  were used as the strain parameters for  $p'$  and  $q$ .

$$\varepsilon_v = \varepsilon_a + 2\varepsilon_r \quad (3.3)$$



$$\gamma = \frac{2}{3}(\varepsilon_a - \varepsilon_r) \quad (3.4)$$

Here,  $\varepsilon_a$  is strain in the axial direction and  $\varepsilon_r$  is strain in the radial direction. Also,  $\gamma$  is the deviatoric strain. The stress ratio parameter is also important:

$$\eta = \frac{q}{p} \quad (3.5)$$

The secant angle, used in evaluation of shear strength, is calculated as follows:

$$\varphi_s = \sin^{-1} \frac{\sigma_a - \sigma_r}{\sigma_a + \sigma_r} \quad (3.6)$$

### 3.2.3 Stress-Strain relationship

Figure 3.2 shows the stress-strain relationship for CC at an intended degree of compaction  $D_c=100\%$  with confining pressures  $\sigma_c'=50, 100$  and  $200\text{kPa}$ . As can be seen in the figure, the peak deviator stress increases dramatically with an increase in confining pressure to  $\sigma_c'=200\text{kPa}$  and the axial strain at which it reaches its peak also increases. In relation to the volumetric strain, the amount of expansive dilation is suppressed as the confining pressure increases.

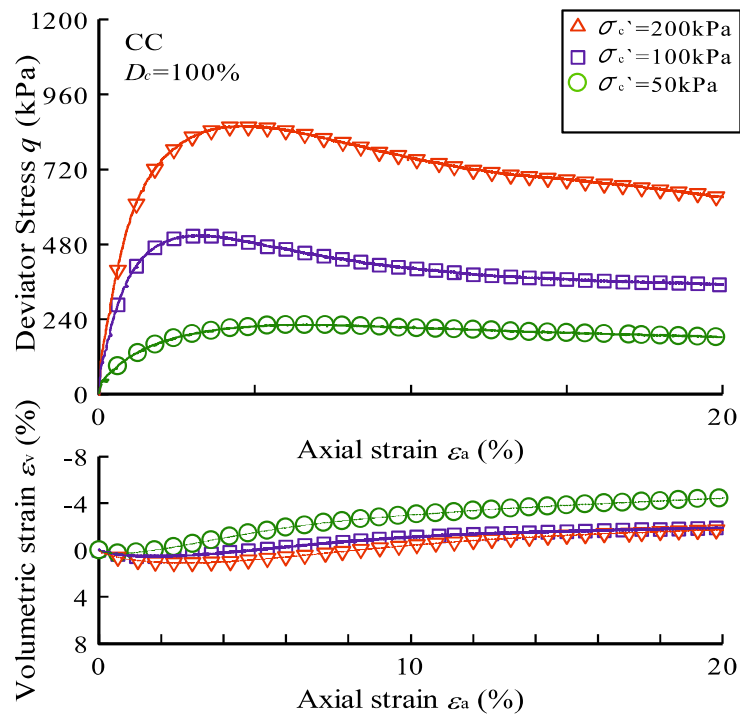


Figure 3.2 Stress-strain relationships for CC ( $D_c=100\%$ )

From these results it is possible to plot a Mohr's stress circle diagram, as shown in Fig. 3.3, and in turn calculate the peak secant angle for each sample of clinker ash at each confining pressure and degree of compaction. As clinker ash is classified as a sandy or gravelly soil, and does not contain clay, it would be assumed that the value for cohesion  $c$  of clinker ash would be zero. However, as can be seen on the diagram, when a failure line is plotted we can see that it gives a positive value for  $c$ . It is believed that this is due to more particle crushing occurring with increase of confining pressure, and so the shear strength does not increase proportionately with confining pressure.

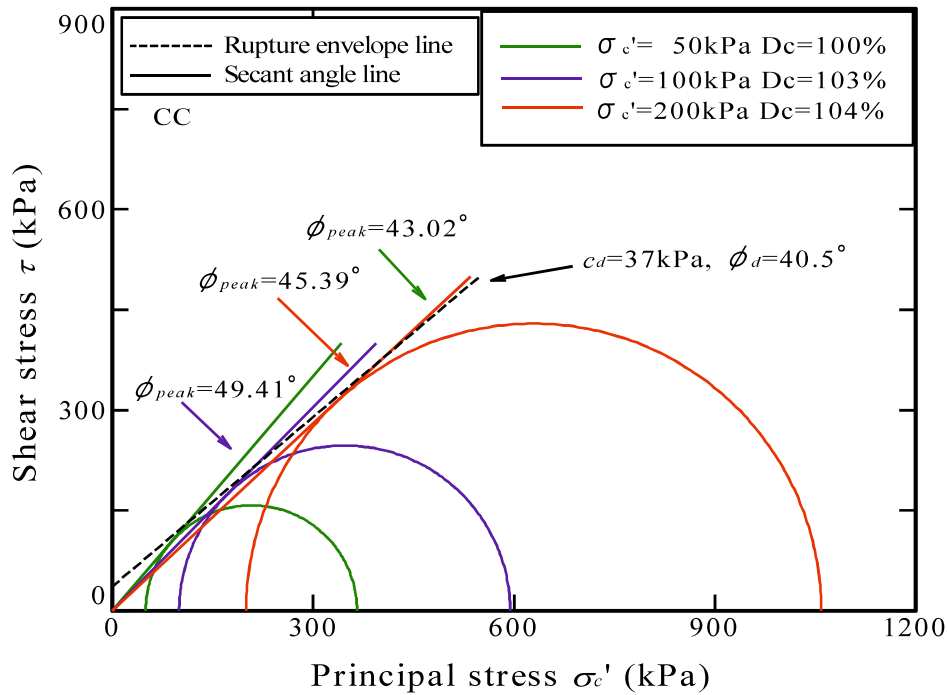


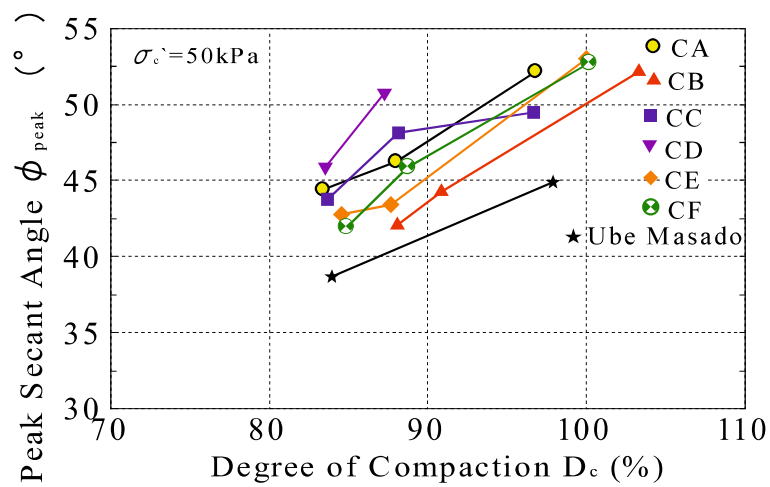
Figure 3.3 Mohr's Stress Circle for CC ( $D_c=100\%$ )

Additional results for Mohr's stress circles plotted from the triaxial compression test results are given in Appendix C.

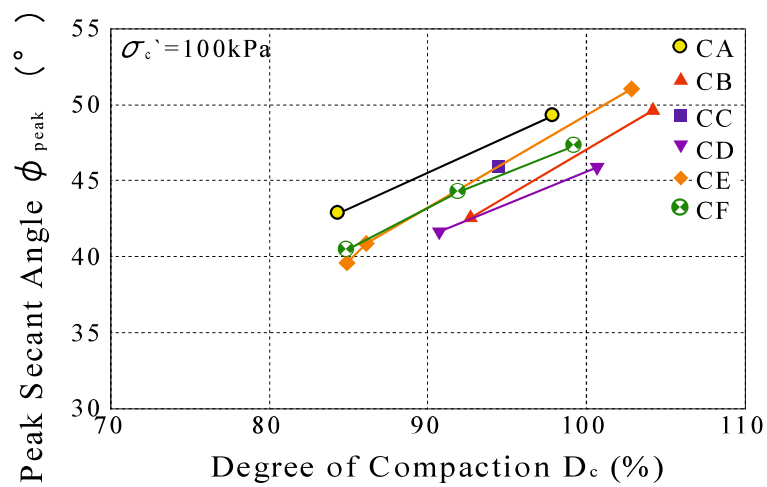
### 3.2.4 Relationship between peak strength $\Phi_{peak}$ and degree of compaction $D_c$

Figures 3.4 (a)-(c) show the relationship between peak secant angle and degree of compaction for the six samples of clinker ash at confining pressures of  $\sigma_c'=50, 100$  and  $200\text{kPa}$ . The results from tests on Ube Masado are also given in (a) and (c) for comparison. As can be clearly seen, an increase in degree of compaction leads to an increase in peak secant angle. The amount of increase of peak secant angle becomes less with an increase in confining pressure, although even at a high confining pressure of  $\sigma_c'=200\text{kPa}$ , all of the clinker ash samples display a peak secant angle of over  $42^\circ$  at a degree of compaction  $D_c=100\%$ . Compared with Ube Masado, all clinker ash samples show higher

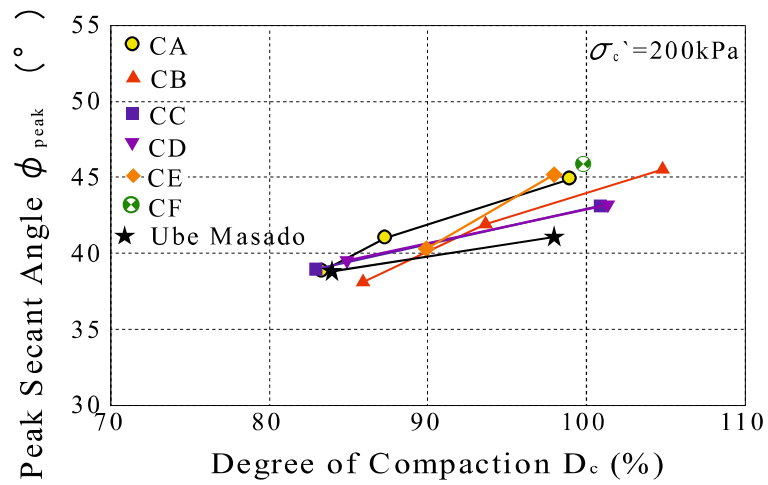
strength under low confining pressure. At high confining pressure however, clinker ash in a loose state gives similar results to that of Ube Masado, due to a loss in strength from particle crushing occurring. It can be seen that clinker ash benefits from compaction more than that of Ube Masado as even under high confining pressure where particle breakage is more prevalent, the clinker ash samples show higher strength with increased degree of compaction.



(a)  $\sigma_c' = 50 \text{ kPa}$



(b)  $\sigma_c' = 100 \text{ kPa}$

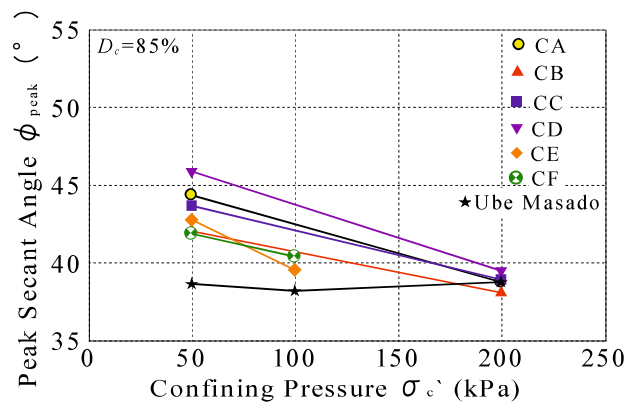


(c)  $\sigma'_c=200\text{kPa}$

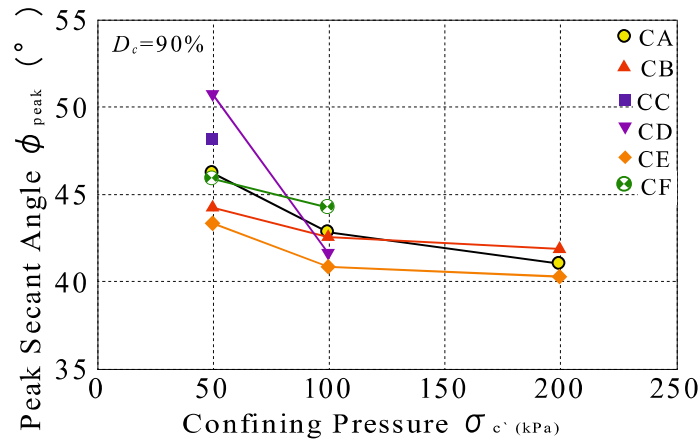
Figure 3.4  $\Phi_{\text{peak}}-D_c$  relationships

### 3.2.5 Relationship between peak strength $\Phi_{\text{peak}}$ and confining pressure $\sigma'_c$

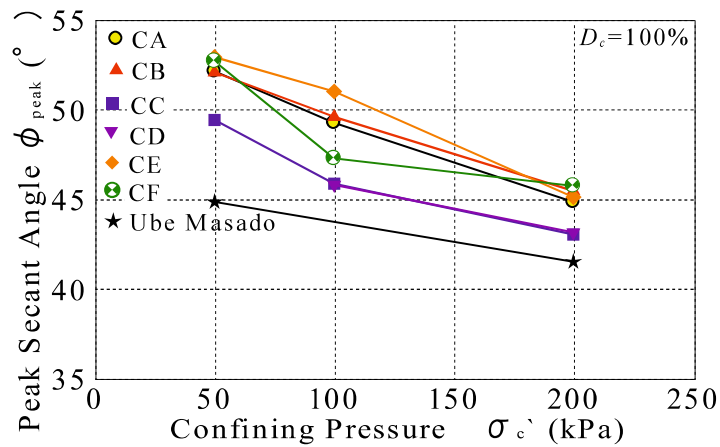
Figures 3.5 (a)-(c) show the relationship between the peak secant angle  $\Phi_{\text{peak}}$  and confining pressure  $\sigma'_c$  at degrees of compaction  $D_c=85, 90$  and  $100\%$ . Ube Masado is also shown in (a) and (c) for comparison. As can be seen, there is a clear trend for the peak secant angle  $\Phi_{\text{peak}}$  to decrease with increasing confining pressure.



(a)  $D_c=85\%$



(b)  $D_c=90\%$



(c)  $D_c=100\%$

Figure 3.5  $\Phi_{peak}-\sigma_{c'}$  relationships

From the above two relationships it can be confirmed that the peak strength of clinker ash is strongly influenced by the degree of compaction and the confining pressure to which it is subjected, with an increase in degree of compaction leading to an increase in peak strength and an increase in confining pressure leading to a decrease in peak strength. Of interest to also note is the effect of particle shape and crushing strength on the peak strength under differing conditions. Under low confining

pressure and in a loose state, it can be seen that CD has the highest peak strength. CD has the weakest mean crushing stress of all the samples, but it has also been evaluated to have the most complex particle shapes, and it would appear that this has more influence on the peak strength under such conditions. On the other hand, under conditions of high confining pressure and high density, CD gives some of the lowest results for peak strength and it is the samples with high particle crushing strength that give the best results.

### **3.2.6 Stress-dilatancy behaviour of clinker ash**

The feature of the stress-dilatancy relationship is to capture the evolution of strain increment and stress ratio of granular material in drained triaxial compression tests. Properly modelling the stress-dilatancy relationships of a granular material is an important criterion in the usefulness of any elasto-plastic constitutive model of granular material. Figures 3.6 and 3.7 show the stress-dilatancy relationships of CA and CF with different degrees of compaction and at different confining pressures. It is noted that the stress-dilatancy relationship of clinker ash is less dependent on the degree of compaction and level of confining pressure. A unique trend line of the stress-dilatancy curves can be drawn for a specific type of clinker ash. The inclination of the trend line and the intercept  $M$  on the vertical axis are unique to each type of clinker ash. It should be highlighted that the inclination of the trend line for clinker ash is lower than that which would be adopted in the cam-clay model due to the high crushability of clinker ash.

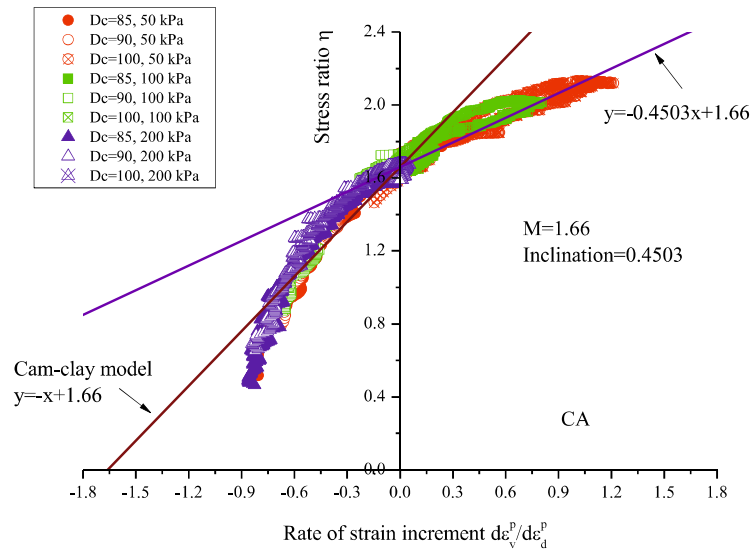


Figure 3.6 Stress-dilatancy relationship of CA under various test conditions

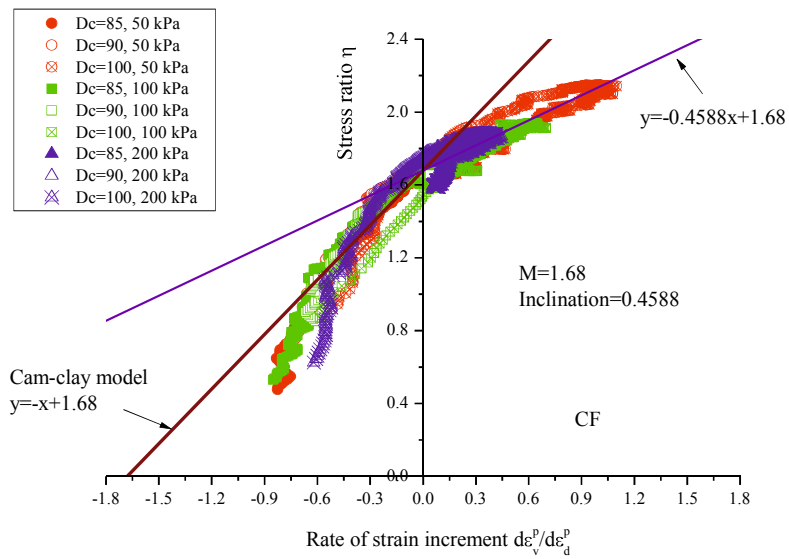


Figure 3.7 Stress-dilatancy relationship of CF under various test conditions

Figure 3.8 shows the stress ratio at critical state  $M$  plotted against the average particle strength and a good correlation can be obtained. The stress ratio at critical state increases with the rise in the average particle strength.



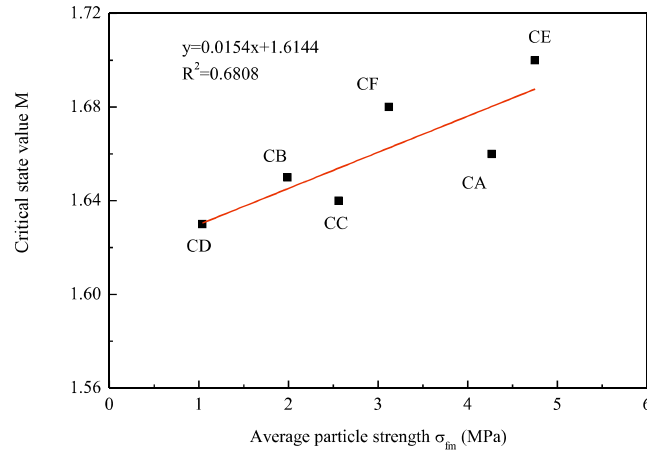


Figure 3.8 Stress ratio at critical state and inclination of CSL plotted against the average particle strength

The flow rule proposed by Nova<sup>3)</sup> in Equation 3.7 is employed to evaluate and model the dilatancy behaviour of clinker ash.

$$D = \frac{(M-\eta)}{(1-N)} \quad (3.7)$$

where  $D = d\varepsilon_v/d\varepsilon_s$  is the dilatancy function and  $M$  is the stress ratio at critical state.  $d\varepsilon_v$  and  $d\varepsilon_s$  are the total volumetric strain rate and total shear strain rate. As the shearing stress continues, the elastic strain portion is far smaller than the corresponding plastic portion. Thus, the dilatancy function  $D$  is approximately treated as the same as the rate of dilation  $d\varepsilon_v^p/d\varepsilon_s^p$ .  $N$  is a density-independent material property and viewed as a volumetric coupling coefficient. Due to the compression-positive convention, the stress ratio at peak point  $\eta_{\text{peak}}$  corresponds to the minimum value of the dilatancy function  $(D_f)_{\text{min}}$ .

Figure 3.9 presents the  $(\eta_{\text{peak}}-M)/(1-N)$  plotted versus  $(D_f)_{\text{min}}$  data of clinker ash at different degrees of compaction and the trend line computed using the Nova stress-dilatancy equation.  $N$  can be

determined from the slope of the approximation line for experimental results between  $(\eta_{\text{peak}}-M)$  and  $D_{\text{min}}$ .  $N$  for clinker ash takes a value ranging from 0.4868 to 0.6075, which is much higher than that of natural sand. It is revealed by Jefferies<sup>4)</sup> that  $N$  can be regarded as a crushability index of sand, with a larger  $N$  value representing a more crushable material. The parameter  $N$  is solely determined by the type of clinker ash.

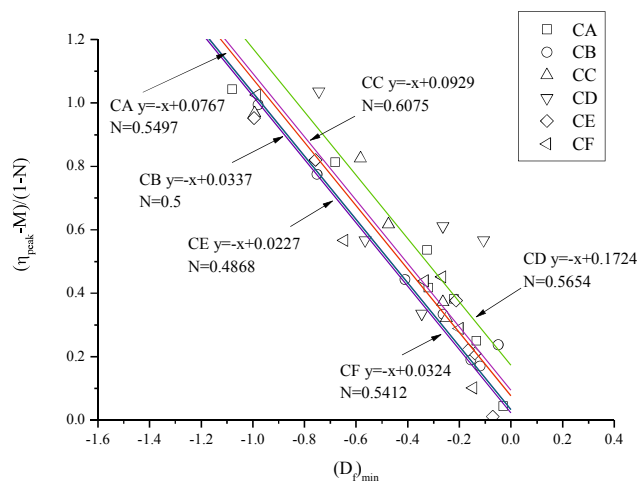


Figure 3.9 Measured dilatancy of clinker ash at various confining pressures

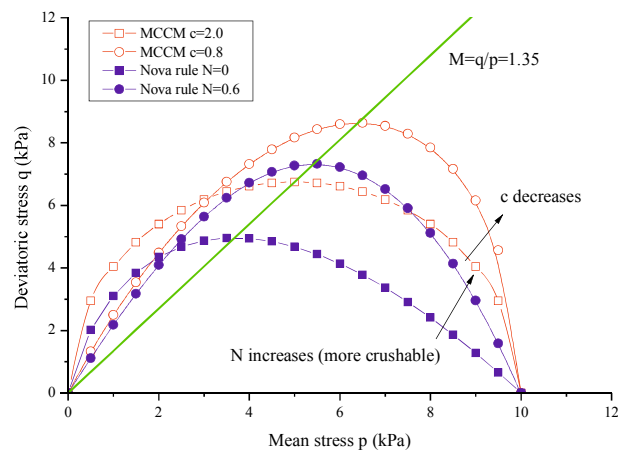


Figure 3.10 Yield surface of Nova model and modified cam-clay model with  $N$  and  $c$

Figure 3.10 shows the yield surface of the Nova model and modified cam-clay model with variable parameters  $N$  and  $c$  to examine the influence of crushability on the shape of yield surface. The parameter  $c$  is introduced into the stress-dilatancy relation in the modified cam-clay model as shown in Equation 3.8.

$$\frac{\eta^2 - M^2}{c\eta} = \frac{de_v^p}{de_d^p} \quad (3.8)$$

It can be seen that the top points of the yield surfaces of the Nova rule and modified cam-clay model move up and to the right, with  $N$  varying from 0 to 0.6 and  $c$  varying from 2 to 0.8. A larger volumetric strain increment is liable to be predicted with the rise in the parameter  $N$  and the reduction in parameter  $c$  which are the indices for highly crushable sand.

Figures 3.11 and 3.12 display the critical state line of CA and CF on the void ratio and mean stress plane. It is distinctive that the critical state line of clinker ash shifts downward with an increase in the degree of compaction. It seems that the critical state line of clinker ash at different degrees of compaction are parallel to each other. The shift of the critical state line is caused by the large amount of particle crushing. This type of behaviour has also been shown in previous investigation<sup>5)</sup> on similar recycled granular materials.

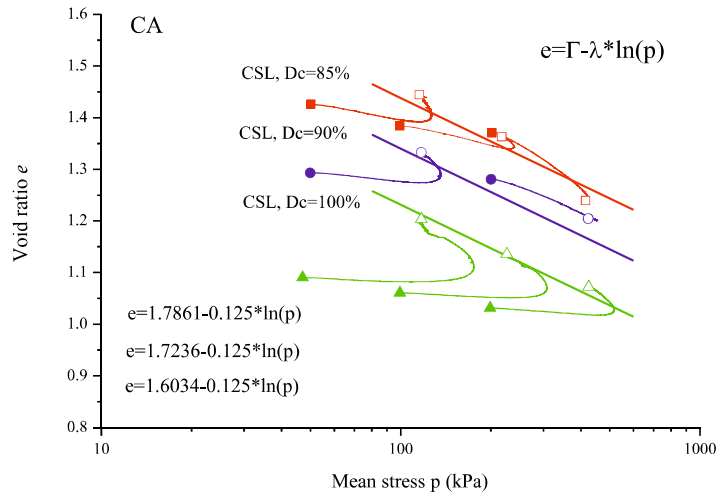


Figure 3.11 Critical state line of CA with various degrees of compaction

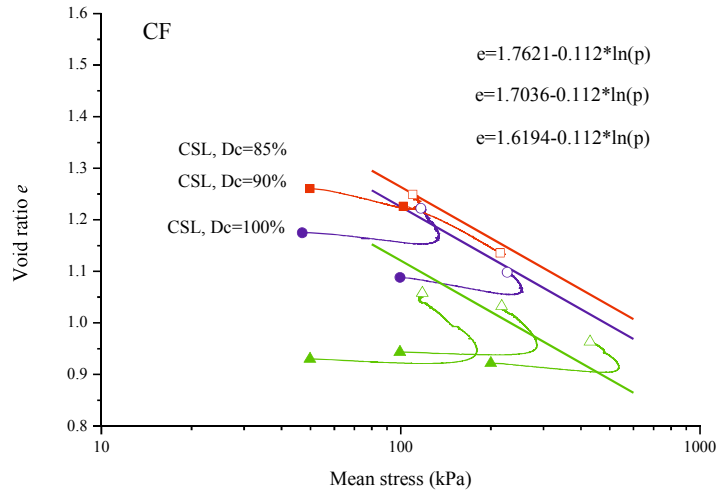


Figure 3.12 Critical state line of CF with various degrees of compaction

### 3.3 Evaluation of the static shear strength of clinker ash

In evaluating the monotonic shear strength of clinker ash, two of the most important factors are the peak strength  $\Phi_{peak}$  and the residual strength  $\Phi_{res}$ . Figure 3.13 shows an example of the points at

which  $\Phi_{peak}$  and  $\Phi_{res}$  are taken.  $\Phi_{peak}$  is taken at the point of peak deviator stress,  $q$ , and  $\Phi_{res}$  is taken at the point when axial strain  $\epsilon_a=20\%$ . It was taken at this point due to time restrictions for the experiments. As can be seen in the figure,  $\Phi_{res}$  shows a similar value, regardless of degree of compaction. As it is taken at an axial strain of 20%, it is possible that the residual secant angle may still become lower.

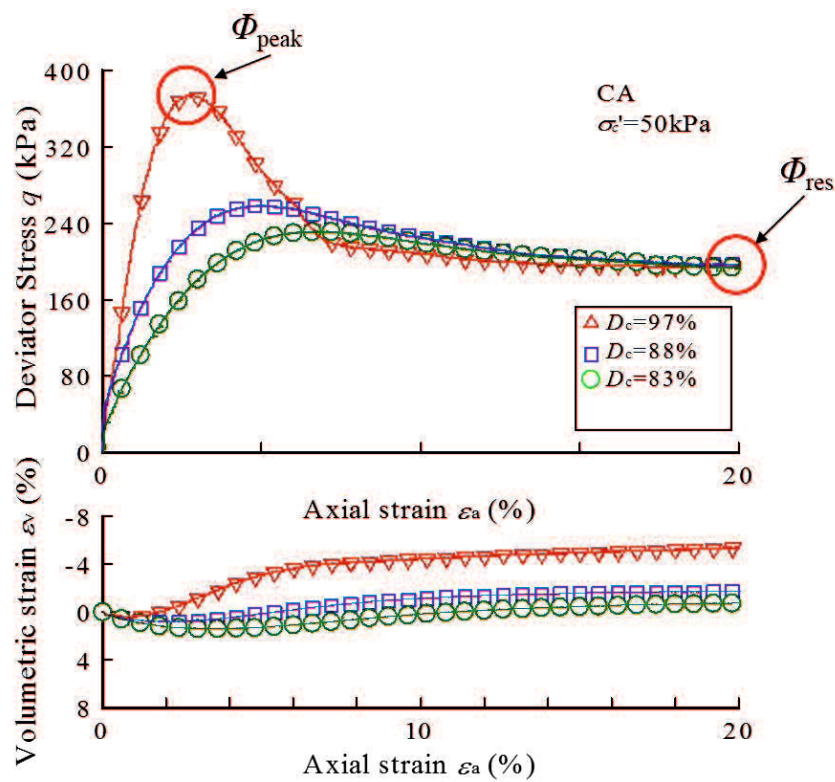


Figure 3.13 Stress-strain relationships for CA

It is found that  $\Phi_{res}$  is a material parameter, influenced by particle strength.  $\Phi_{peak}$ , however, is a mechanical factor, which as well as being influenced by particle strength is also affected by the degree of compaction and confining pressure.

For evaluation of the strength parameters used in this research, an adaptation of Bolton<sup>(6)</sup>'s equation (3.9) for the peak strength of sands is proposed. Here,  $\Phi_{cr}$  is changed to  $\Phi_{res}$ ,  $D_r$  is changed to  $D_c$  and

$p$  is replaced with  $\sigma_c$ , which gives Equation 3.10.

$$\Phi_{peak} = \Phi_{cr} + CD_r \ln\left(\frac{P_{cr}}{p}\right) \quad (3.9)$$

$$\Phi_{peak} = \Phi_{res} + CD_c \ln\left(\frac{P_{cr}}{\sigma_c}\right) \quad (3.10)$$

$C$  is a material parameter. If it is taken that  $\Phi_{res}$  is a constant regardless of  $D_c$ , then this equation shows that the difference in  $\Phi_{peak}$  and  $\Phi_{res}$  ( $\Phi_{peak} - \Phi_{res}$ ) is decided by the density and confining pressure. It shows that when  $p$  becomes equal to  $P_{cr}$ , the influence of initial density and confining pressure on  $\Phi_{peak}$  is lost. Therefore, if the residual strength  $\Phi_{res}$ , material parameter  $C$  and  $P_{cr}$  are known, then the peak strength  $\Phi_{peak}$  can be estimated. As shown in Figure 3.13 above, the degree of compaction has little influence on the residual strength, and as such the peak strength of clinker ash will be evaluated using the adaptation of Bolton's equation.

### 3.3.1 Evaluation of residual strength $\Phi_{res}$

The residual strength varies between the samples of clinker ash. It was thought that this is due to the difference in single particle crushing strength. Figure 3.14 shows the relationship between the mean average crushing stress  $\sigma_{fm}$  and residual strength  $\Phi_{res}$ . From the figure, a good correlation between the two parameters can be seen and as such the residual strength  $\Phi_{res}$  was evaluated in Equation 3.11.

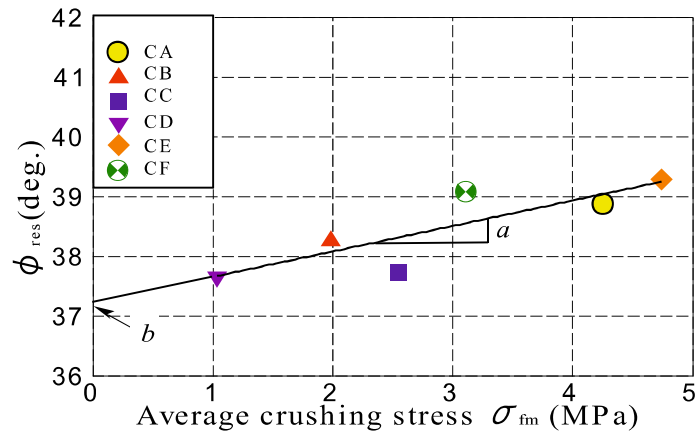


Figure 3.14  $\sigma_{fm}$ -  $\phi_{res}$  relationship

$$\phi_{res} = 0.4\sigma_{fm} + 37 \quad (3.11)$$

### 3.3.2 Evaluation of $P_{cr}$

Figure 3.15 shows the relationship between  $\phi_{peak}-\phi_{res}$  at each confining pressure. As the peak strength and residual strength become equal when the confining pressure exceeds  $P_{cr}$ , the confining pressure when  $\phi_{peak}-\phi_{res}=0$  is the  $P_{cr}$  for each clinker ash sample. Also,  $P_{cr}$  was found to have a high correlation with density and particle shape, and is evaluated with Equation 3.12. Figure 3.16 shows the relationship between experimental values for  $P_{cr}$  and calculated values. As the calculated values and experimental values show good correlation, Equation 3.12 was used to for the evaluation of  $P_{cr}$ .

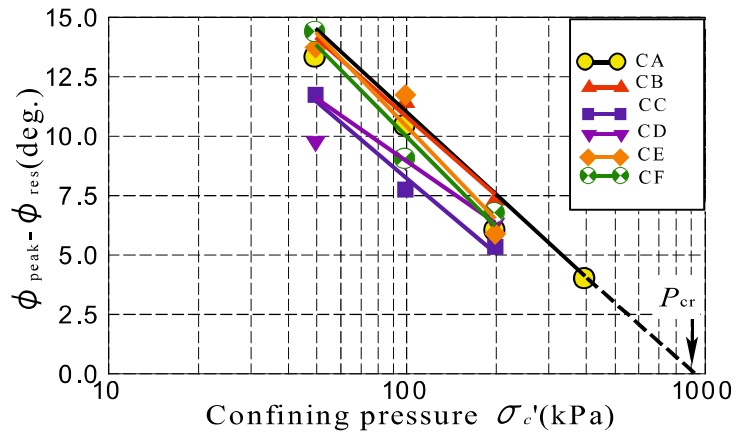


Figure 3.15 Relationship between  $\phi_{peak} - \phi_{res}$  and  $\sigma'_c$

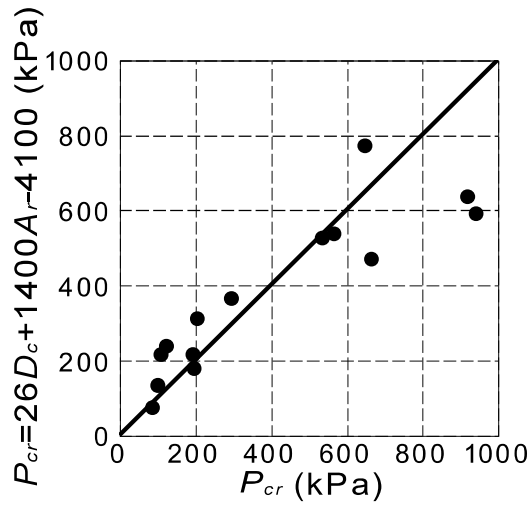


Figure 3.16 Relationship between experimental and calculated  $P_{cr}$

$$P_{cr} = 26D_c + 1400A_r - 4100 \quad (3.12)$$

### 3.3.3 Evaluation of material parameter $C$

Figure 3.17 shows the relationship between  $\phi_{peak} - \phi_{res} / D_c$  and  $P_{cr} / p$ . The gradient of the fitted line is  $C$  and from investigation of the material parameter it was found that there was high correlation



between the average particle crushing stress  $\sigma_{fm}$  and the values for  $C$ , as shown in Figure 3.18. The material parameter  $C$  was therefore evaluated through Equation 3.13.

$$C = 0.4\sigma_{fm}^{3.5} \quad (3.13)$$

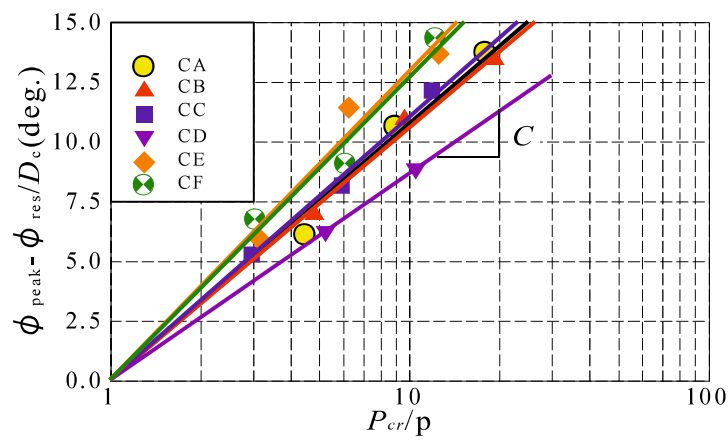


Figure 3.17 Relationship between  $\Phi_{peak} - \Phi_{res}/D_c$  and  $P_{cr}/p$

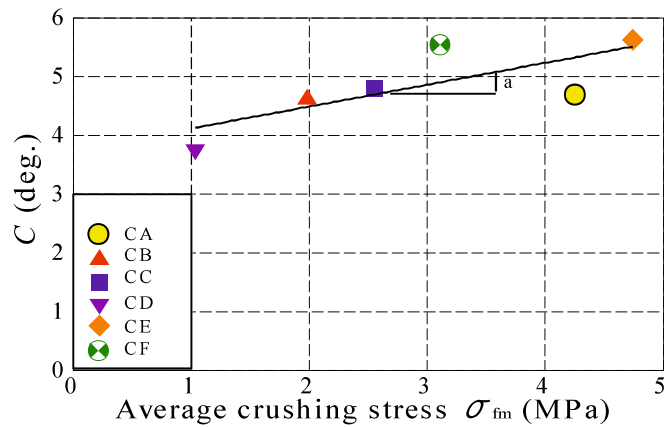


Figure 3.18 Relationship between  $C$  and  $\sigma_{fm}$

### 3.3.4 Evaluation of peak strength $\Phi_{\text{peak}}$

Through inserting the residual strength  $\Phi_{\text{res}}$ , material parameter  $C$  and  $P_{\text{cr}}$  as gained in the above method into Equation 3.10, it is possible to estimate the peak strength  $\Phi_{\text{peak}}$  for each sample of clinker ash. Figure 3.19 shows a comparison of the predicted line for peak strength  $\Phi_{\text{peak}}$  and experimental results at each confining pressure. Although there are some slight variations in the results, it can be seen that on the whole the experimental results are close to the predicted lines. Also, Figure 3.20 shows a comparison of estimated and experimental peak strength  $\Phi_{\text{peak}}$  at each degree of compaction. From the figure, it can be seen that at lower densities the aspect ratio has a large influence, with CD showing high peak strength, however at high densities this changes to single particle strength having more influence, and samples such as CE with high particle strength show higher peak strength. From this, it can be said that through using Equation 3.10 it is possible to some degree to estimate the peak strength  $\Phi_{\text{peak}}$  for each clinker at sample at each confining pressure and degree of compaction.

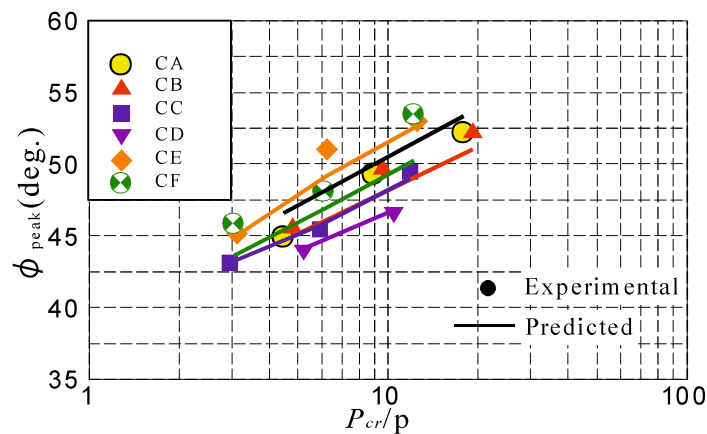


Figure 3.19 Relationship between  $\Phi_{\text{peak}}$  and  $P_{\text{cr}}/p$  with experimental and predicted results

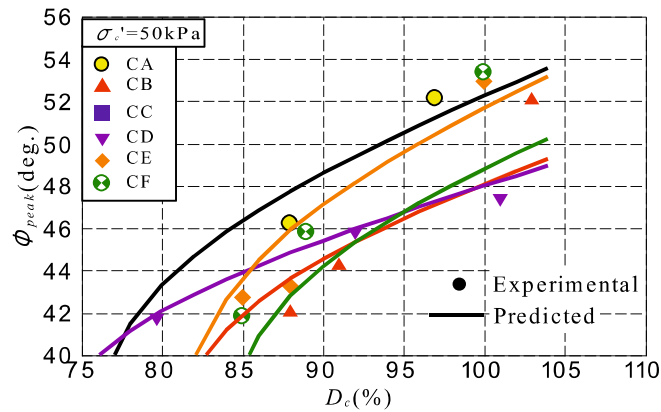


Figure 3.20 Relationship between  $\phi_{peak}$  and  $D_c$  with experimental and predicted results

### 3.4 Coloured particle crushing observation

In order to investigate if and how particle crushing occurs during shear, specimens used in triaxial compression tests were seeded with painted particles. Clinker ash contains particles of different colours, and in particle crushing tests it was found that average particle crushing stress varied between the different colours. The painted particles were observed under a microscope before and after the test in order to investigate any particle crushing occurring. Yellow particles were painted red, red particles were painted green, white particles were painted blue and black particles were painted yellow. The particles will be referred to as their original colour.

#### 3.4.1 Test procedure

The test was performed as follows:

1) Dried sample was sieved between the ranges of 2mm-4.75 and 20 particles of each colour were taken for observation.

2) Different coloured paint was applied to the different coloured particles, which were then

observed under the microscope.

3) The painted particles were mixed in with the sample for the test and triaxial compression was performed.

4) After the test was complete, the specimen was washed in a 700 $\mu$ m sieve and dried in an oven.

5) After the specimen was dried, the painted particles were retrieved and observation was again carried out as before the test.

Table 3.2 Average crushing stress  $\sigma_{fm}$  (MPa) for clinker ash particles

Sample	Black	Yellow	Red	White
CD	0.18	0.89	0.87	0.32
CE	2.86	1.15	0.53	0.56

### 3.4.2 Particle observation before and after shearing

Figure 3.21 shows the relationship between crushing stress and particle diameter for yellow CD particles. The average crushing stress of the yellow CD particles is almost the same as that of the red CD particles. It can be seen that there is a trend for the crushing stress to decrease with increasing particle diameter.

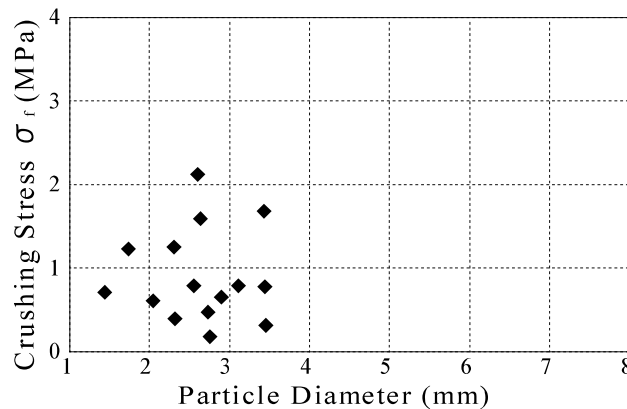


Figure 3.21 Relationship between crushing stress and particle diameter for yellow CD particles

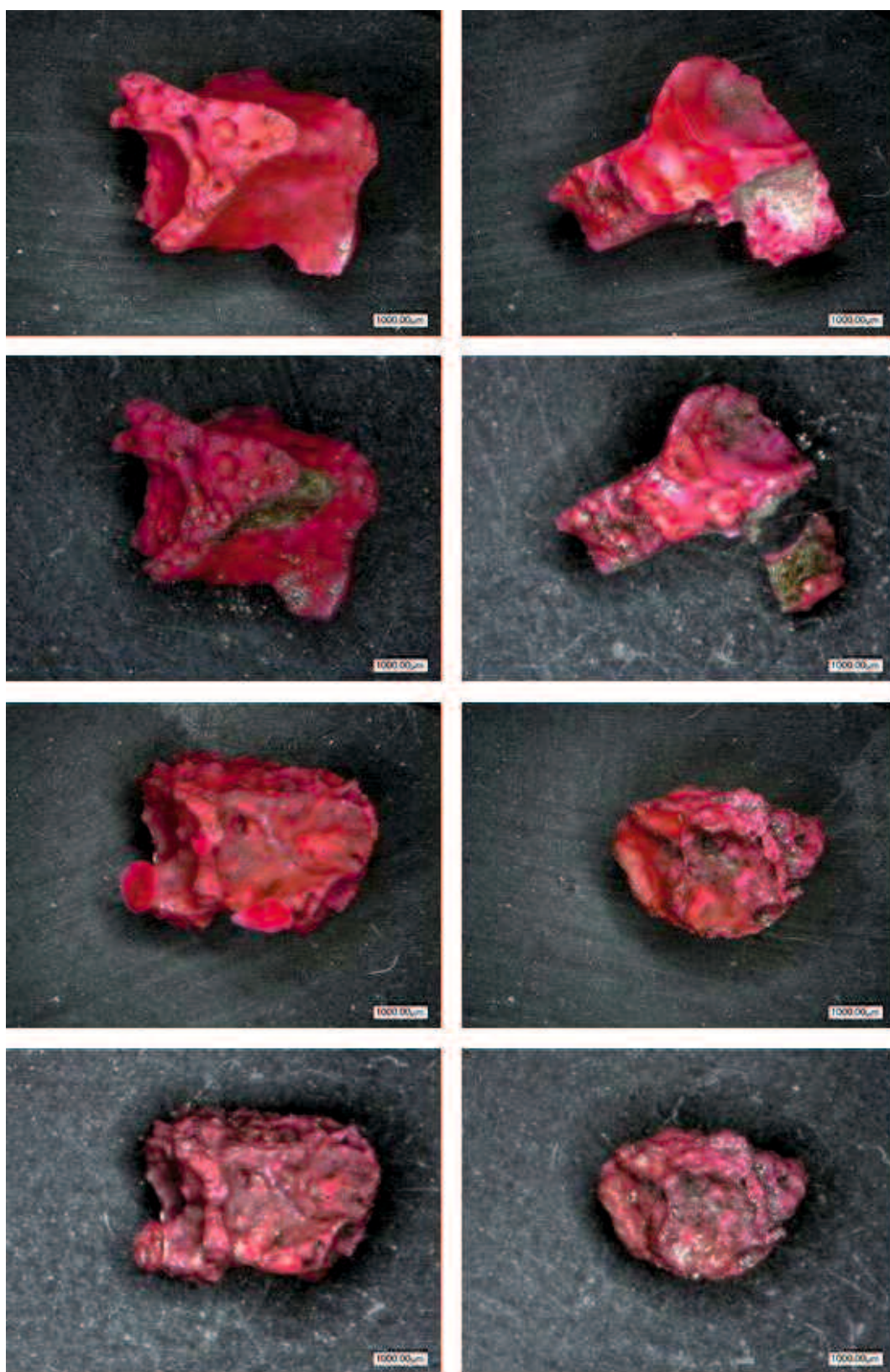


Figure 3.22 Yellow CD particles before (above) and after (below) shear

Figure 3.22 shows observations of the coloured yellow particles used in the experiment. The yellow particles exhibit a relatively high crushing stress, and this is reflected in the observation which does not show much breakage occurring. However, due to the very angular shapes of the yellow CD particles, there are quite a few instances of fracturing of these angularities being observed.

Figure 3.23 shows the relationship between crushing stress and particle diameter for red CD particles. The red particles show a comparatively higher particle strength for the most part compared with other coloured CD particles, and display a trend for decreasing crushing stress with increasing particle diameter.

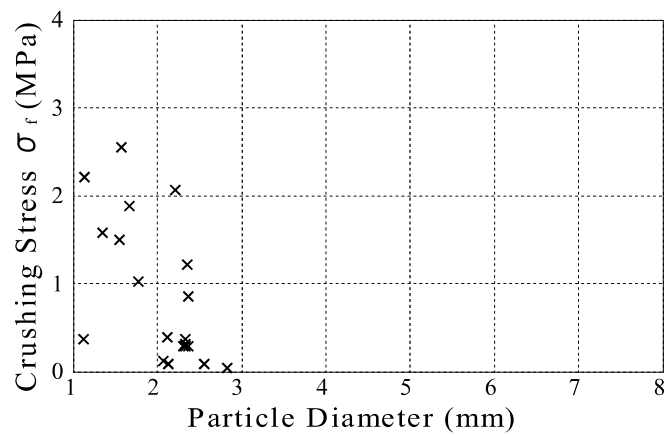


Figure 3.23 Relationship between crushing stress and particle diameter for red CD particles

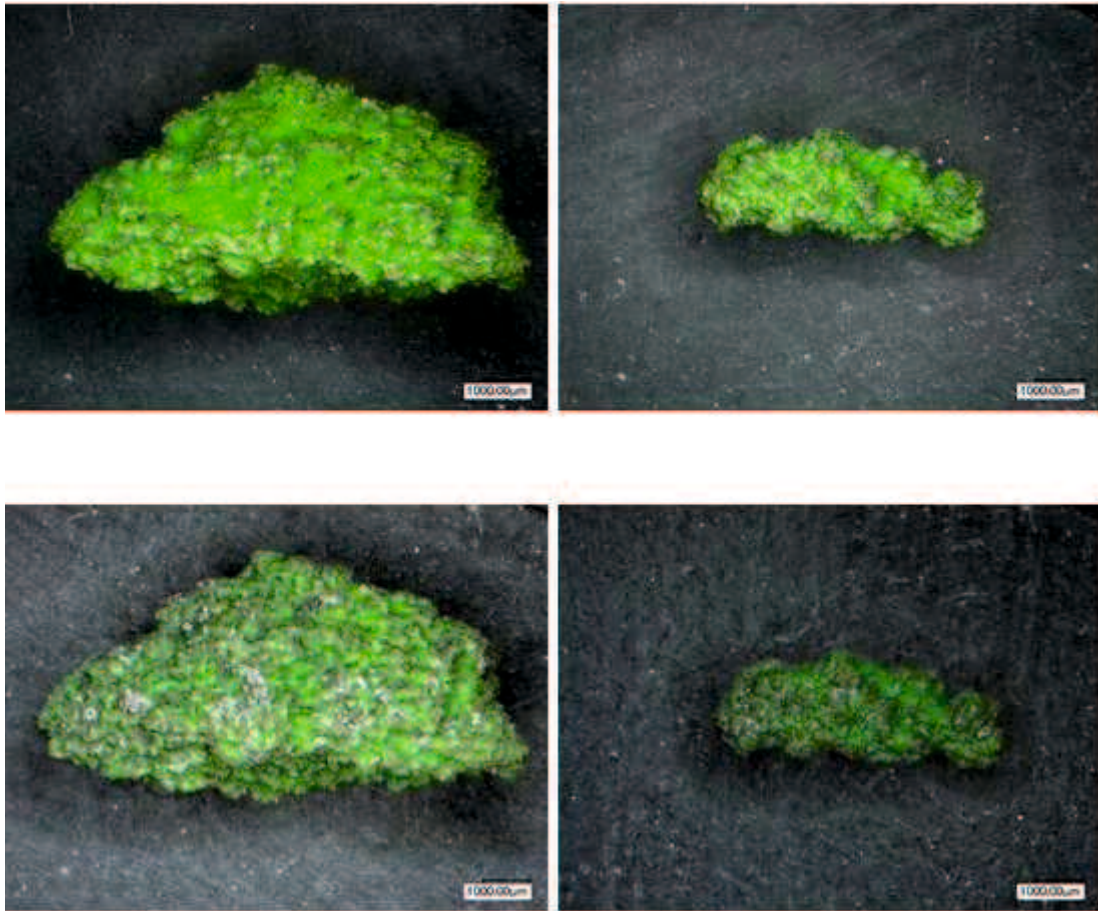


Figure 3.24 Red CD particles before (above) and after (below) shear

Figure 3.24 shows microscopic observations of red CD particles before and after shear. The red particles show the second highest average crushing stress out of the tested coloured particles, and this is reflected in the way that no apparent breaking or fracturing appears to have occurred. It is not known yet exactly what contributes to the difference in crushing stresses between the different coloured particles. The yellow CD particles, which have a very slightly higher average crushing stress, show quite a few instances of fracturing, compared with the red CD particles which show none, although this could be due to the yellow CD particles having more complex particle shapes.

Figure 3.25 shows the relationship between crushing stress and particle diameter for white CD particles. The white particles displayed the second lowest average crushing stress for the CD particles testes and display an overall trend of decreasing crushing stress with increasing particle diameter.

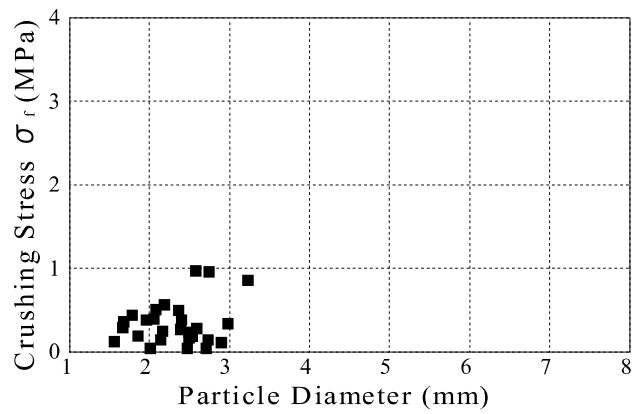


Figure 3.25 Relationship of crushing stress and particle diameter for white CD particles



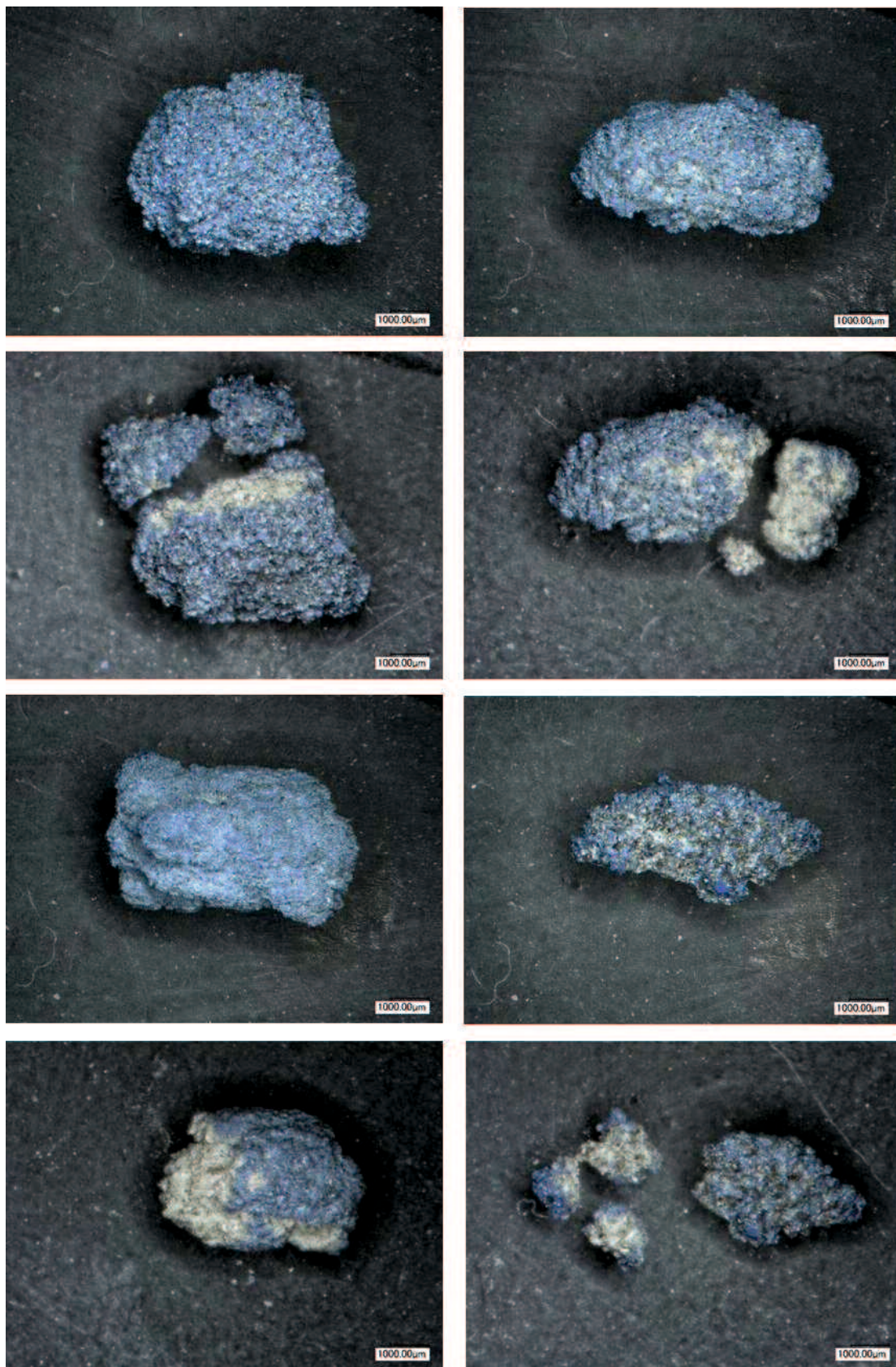


Figure 3.26 White CD particles before(above) and after(below) shear

Figure 3.26 shows microscopic observation of white CD particles before and after shearing. Having the second lowest average crushing stress of the CD particles, it is no surprise that multiple occurrences of particle breakage can be observed. Unlike the stronger yellow particles, which appeared to exhibit fracturing of the angular extremities, the white particles show breakage across the particle body itself, with some particles breaking into 3 or more pieces.

Figure 3.27 shows the relationship between crushing stress and particle diameter for black coloured particles from the CD sample. As can be seen, most of the particles display a low crushing stress, and the crushing stress shows a trend of decreasing with increasing particle diameter.

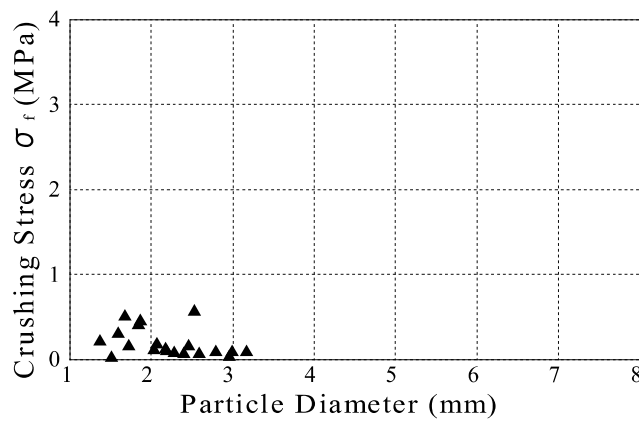


Figure 3.27 Relationship between crushing stress and particle diameter for black CD particles

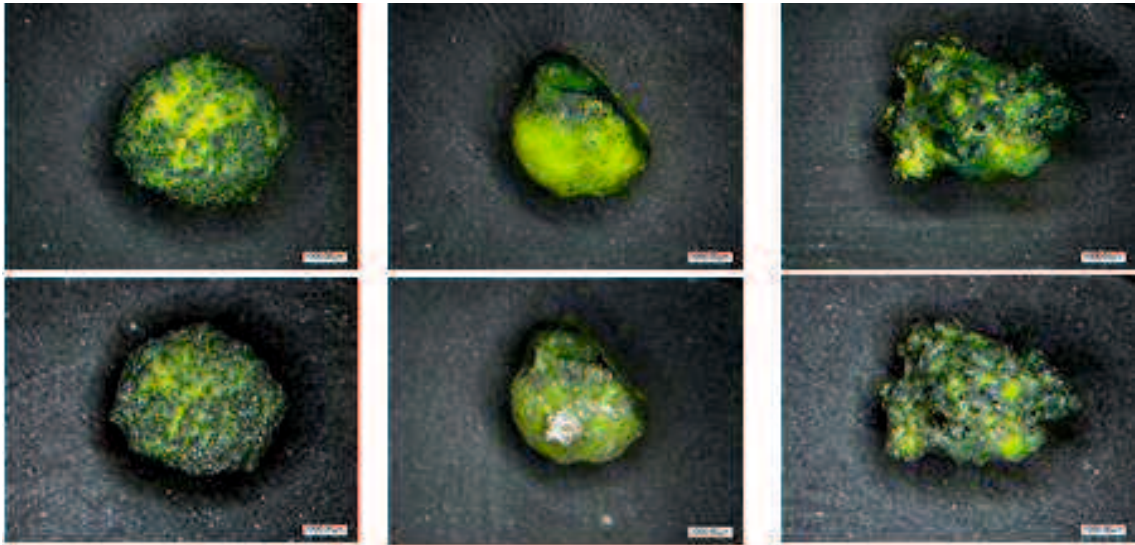


Figure 3.28 Black CD particles before (above) and after (below) shear

Figure 3.28 shows black CD particles before and after shear. As can be seen, there is no apparent breaking or fracturing of the particles, and only slight abrasion to the surface. Due to the very low particle strength of the black CD particles, it was not possible to find most of the coloured particles after shearing. The particles break easily simply when being handled, so it can be assumed that they crumble completely during the triaxial compression test process. Although for the most part the black CD particles exhibit a very low particle strength, there is also a small proportion with a relatively high particle strength, which would explain why some of the particles, for example those shown in Figure 3.28, do not display any clear sign of damage or breakage.

Figure 3.29 shows the relationship between crushing stress and particle diameter for black CE particles. The black CE particles displayed the highest average crushing stress, and as can be seen there is a tendency for crushing strength to decrease with increasing particle diameter.

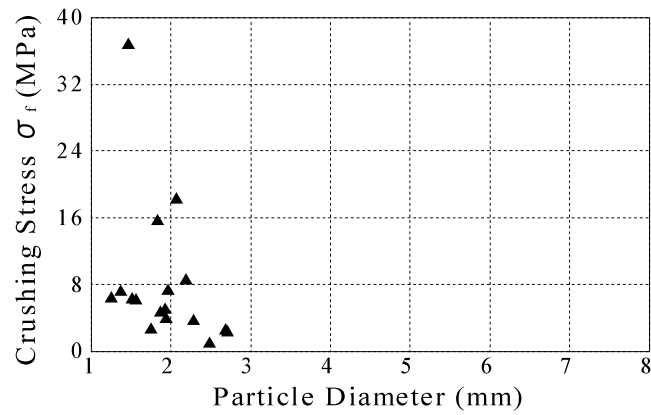


Figure 3.29 Relationship of crushing stress and particle diameter for black CE particles

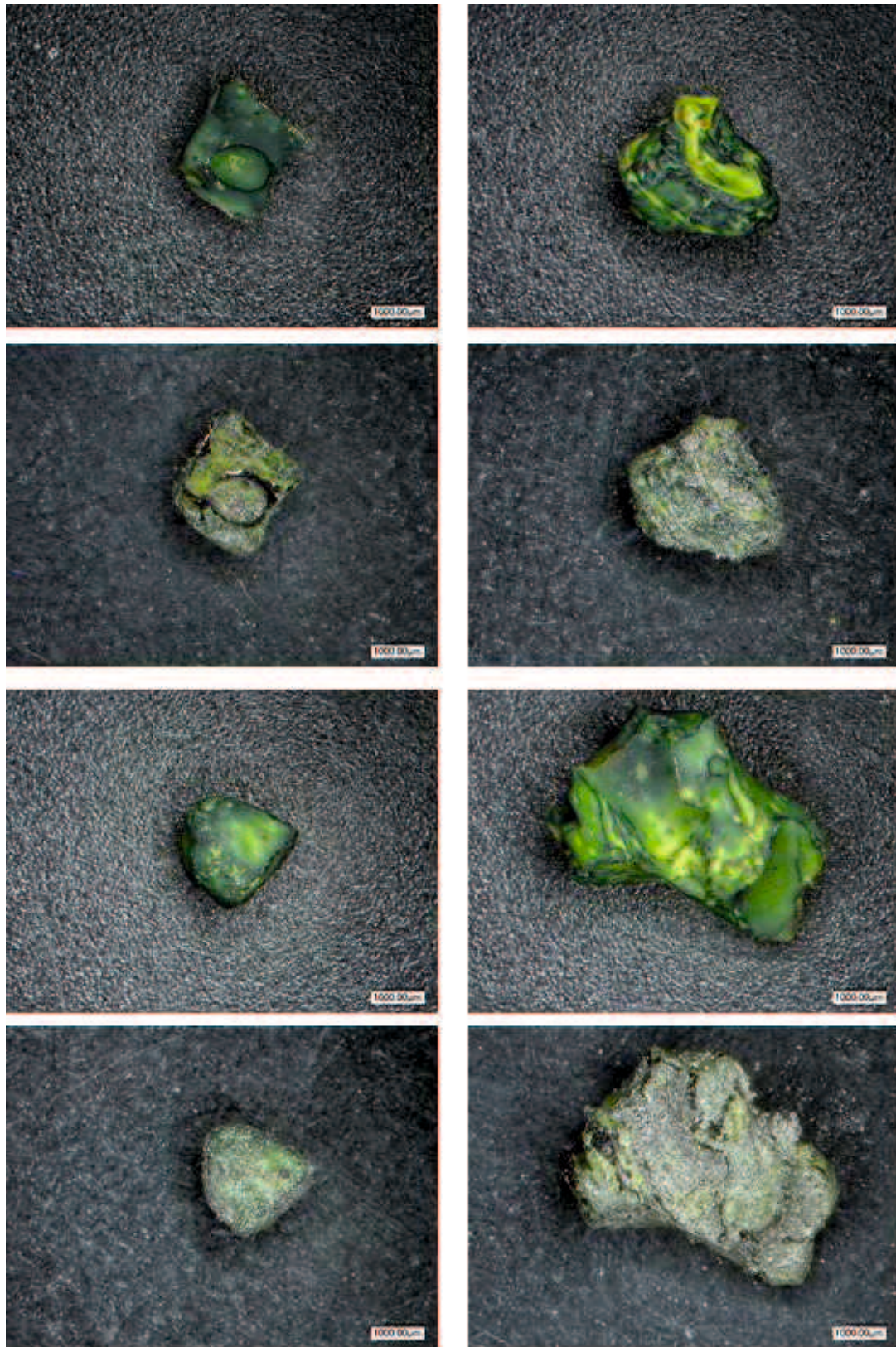


Figure 3.30 Black CE particles before (above) and after (below) shear

Due to the very high crushing strength displayed by the black CE particles, it was not possible to observe any kind of crushing or fracturing from the experiment. There is clear abrasion of the surface occurring, however there is no change in particle shape.

The Yellow CE particles displayed the second highest mean crushing stress of the CE particles. Unlike most of the other coloured particles, the crushing stress appears to remain almost steady, regardless of particle size, as can be seen in Figure 3.31.

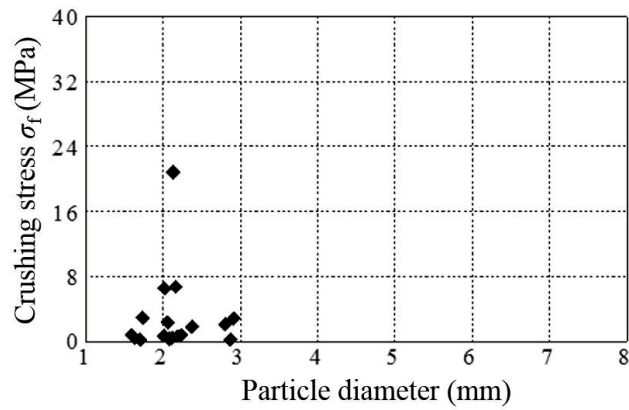


Figure 3.31 Relationship of crushing stress and particle diameter for yellow CE particles

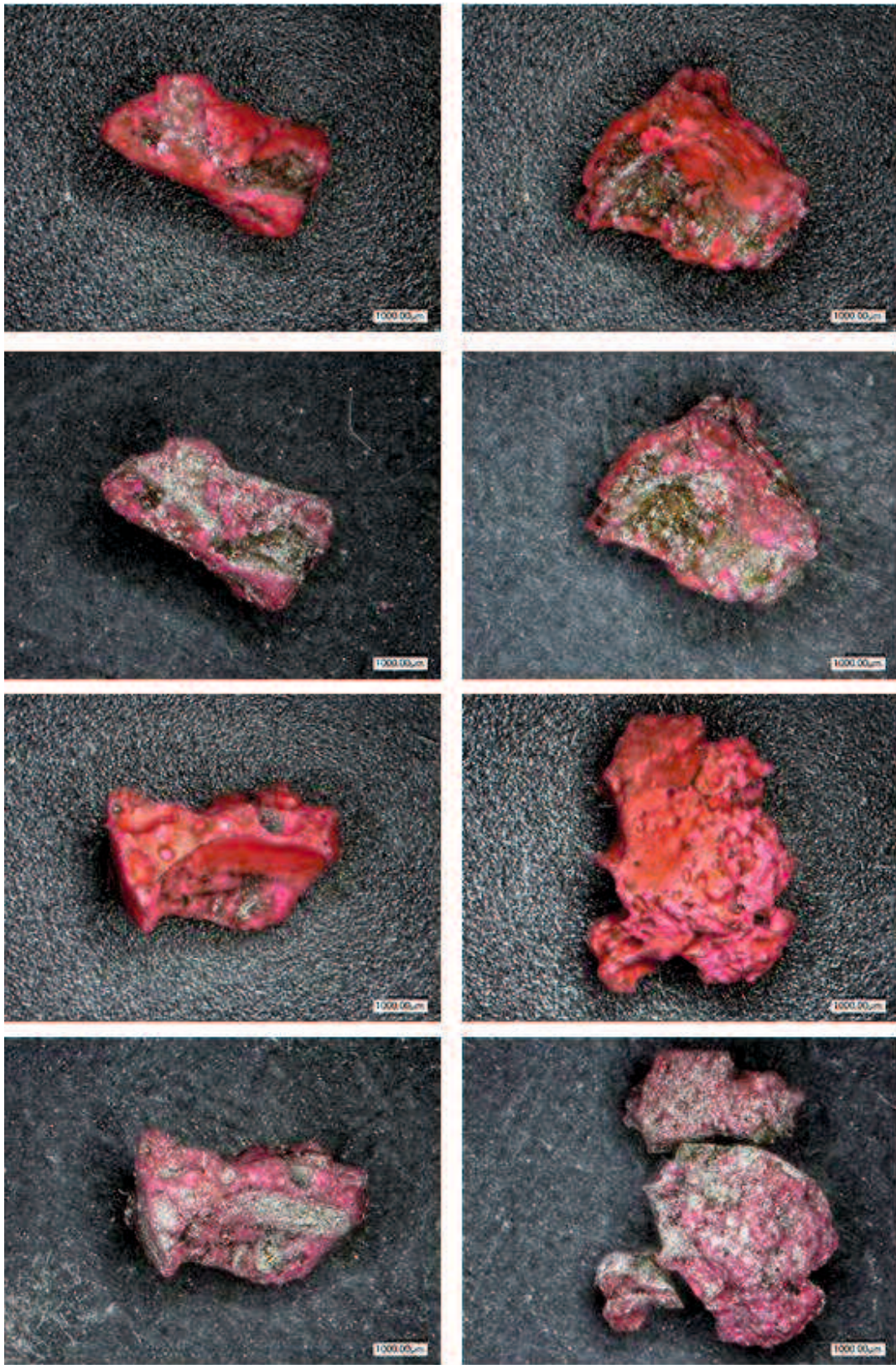


Figure 3.32 Yellow CE particles before (above) and after (below) shear

Figure 3.33 shows the relationship between the crushing stress and particle diameter for red CE particles. As can be seen, there is an overall trend for crushing strength to decrease with increase in particle diameter size.

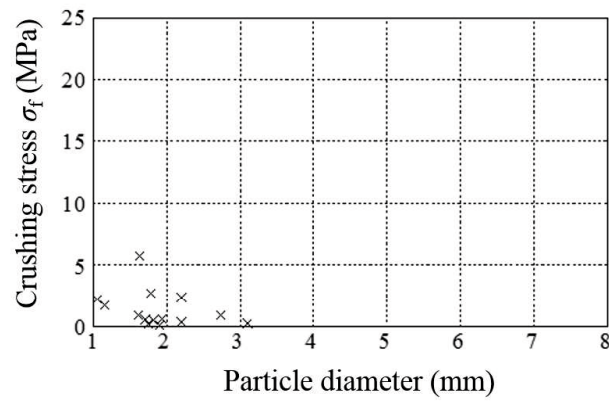


Figure 3.33 Relationship of crushing stress and particle diameter for red CE particles



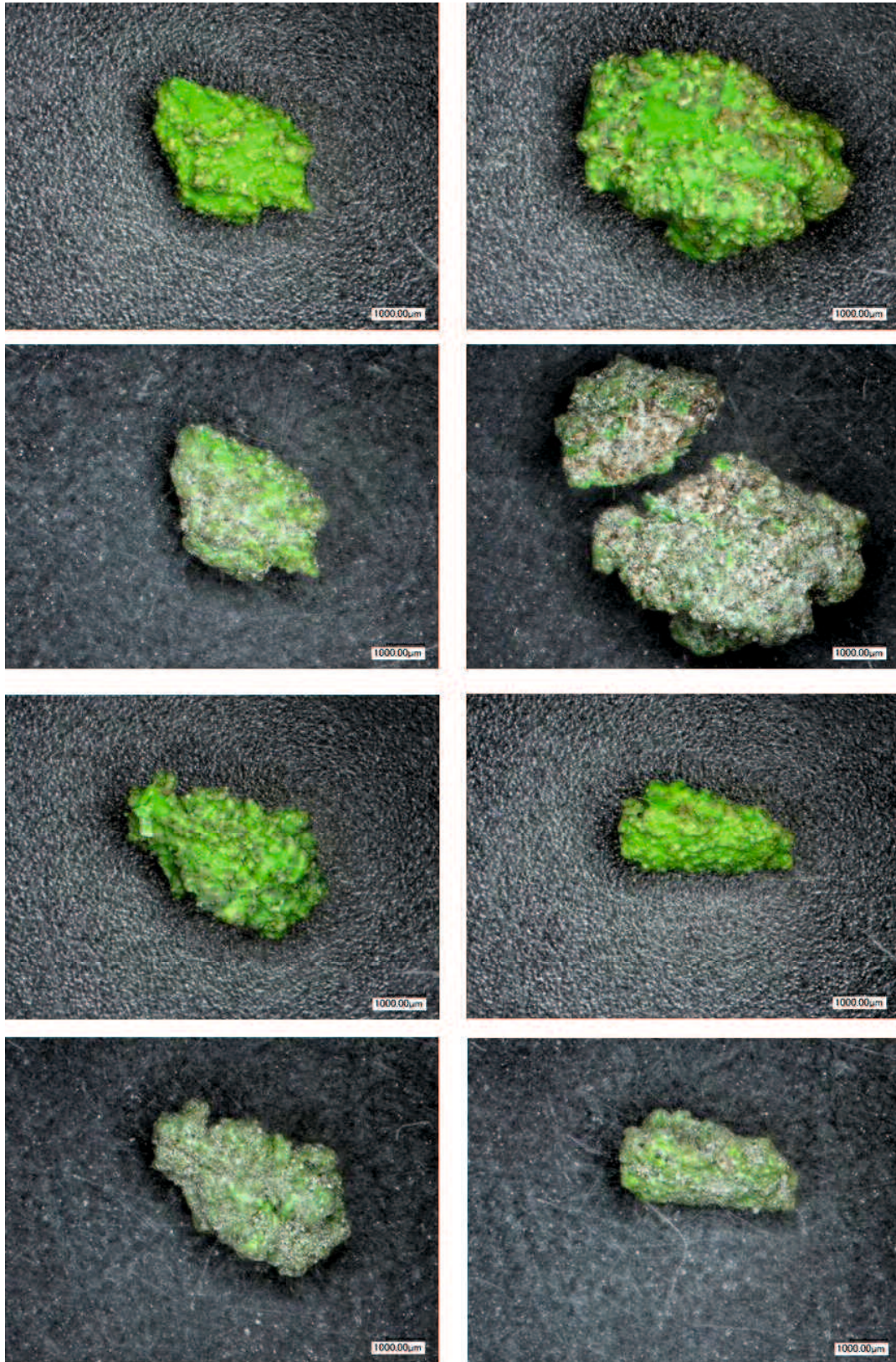


Figure 3.34 Observation of red CE particles before (above) and after (below) shear

As can be seen from Figure 3.34, there are a couple of instances of particle breakage occurring, with the particles breaking almost in half.

Figure 3.35 shows the relationship between crushing stress and particle diameter for white CE particles. The white CE particles displayed the lowest crushing stress of CE particles and as can be seen from the diagram, the crushing stress does not vary much with change in particle diameter.

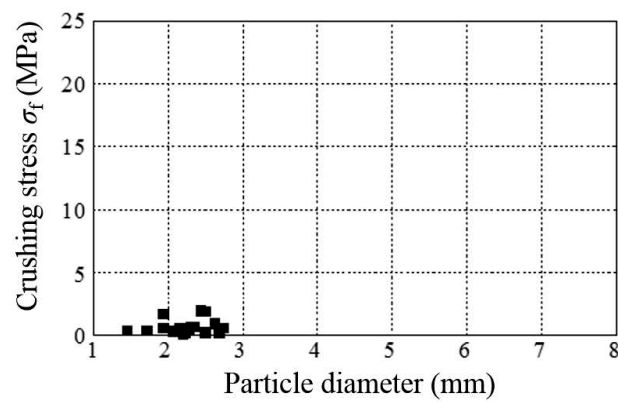


Figure 3.35 Relationship of crushing stress and particle diameter for white CE particles

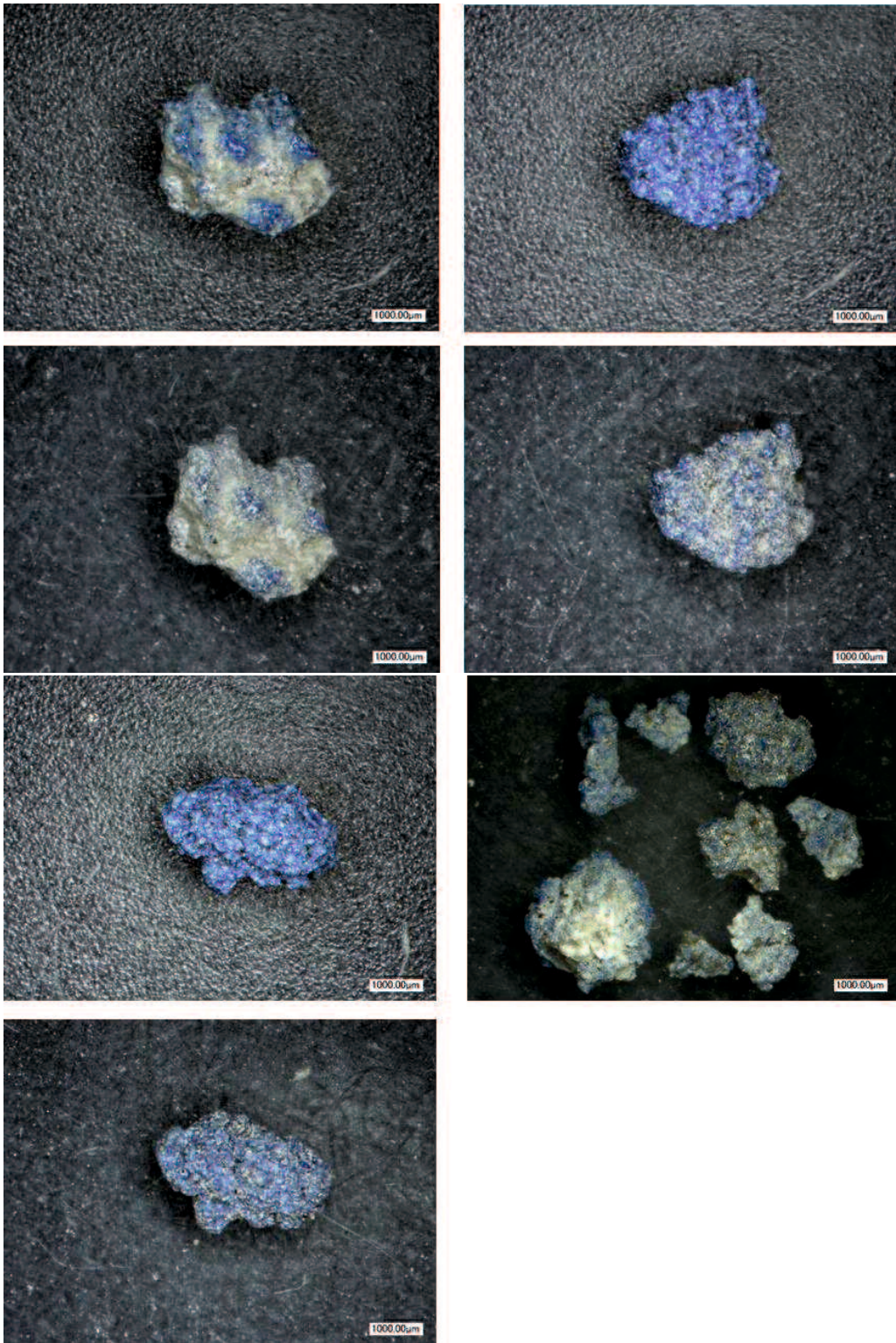


Figure 3.36 Observation of white CE particles before (above) and after (below) shear

Even though the white CE particles displayed the lowest crushing strength, not much particle crushing can be observed from Figure 3.36, with only a couple of instances of small chipping occurring. However, given the fact that only half of the initial coloured particles were found after testing, it is likely that much more crushing occurred, causing the particles to break into small pieces which could not be easily found. The final picture shows particle pieces that could not be matched to the original particles, but give evidence of multiple instances of particle crushing occurring during the shear test.

### 3.5 Summary

#### 1) Triaxial Compression Tests

An increase in confining pressure leads to a decrease in peak secant angle, it is believed that this is due to particle crushing occurring during consolidation.

An increase in degree of compaction leads to a large increase in peak secant angle.

The residual secant angle converges to a similar value, regardless of degree of compaction, and it was found that the average crushing stress gained from particle crushing tests correlates with the residual secant angle, with an increase in average crushing stress leading to a higher value for residual secant angle.

Through observation of the stress-dilatancy behaviour a single value for the stress ratio at critical state  $M$  could be obtained for each type of clinker ash.

Use of the Nova rule gave values for a crushability parameter for each type of clinker ash.

It was found that separate critical state lines exist for clinker ash depending on degree of compaction.

Through the use of an adapted equation for Bolton's equation for the peak strength of sands, it was found that the peak strength  $\Phi_{\text{peak}}$  of the clinker ash samples could be estimated to a good degree at

different densities and confining pressures.

The different coloured particles of the different clinker ash samples have varying strength properties, and the crushing behaviour during shear also changes based on the colour of the particles.

## References

- 1) Wakatsuki Y, Tanaka H, Uchida Y, Irie K, Hyodo M, Yoshimoto N (2007) Material characteristics of clinker ash and examination of applicability, *Japanese Geotechnical Journal*, 2(4), 271-285.
- 2) Wakatsuki Y, Hyodo M, Yoshimoto N, Anai R, Yoshinaga Y, Yoshioka I, Nakashita A (2009) Particle characteristics and strength, deformation characteristics of loose clinker ash, *Journal of Japan Society of Civil Engineers*, 65(4), 897-914
- 3) Fujishima T, Yoshimoto N, Hyodo M, Nakata Y, Yoshioka I, Nakashita A, Nakamura Y, Wakatsuki Y: Compression and shear strength characteristics of clinker ash, *46th Annual Meeting of Japanese Geotechnical Society*, 347-348.
- 3) Nova, R. (1984) A model of soil behaviour in plastic and hysteretic ranges. Part 1 – monotonic loading, in *Constitutive modelling of Soil Behavior*. Rotterdam: Balkema, 289-309.
- 4) Jeffries M.G. (1993) Nor-sand: a simple critical state model for sand, *Geotechnique*, 43, 91-103.
- 5) Heitor A, Indraratna B, Kaliboullah C. I, Rujikiatkamjorn C, and McIntosh G.W. (2016) Drained and undrained shear behavior of compacted coal wash. *Journal of Geotechnical and Geoenvironmental Engineering*, 142(5), 23-58.
- 6) Bolton M.D. (1986) The strength and dilatancy of sands, *Geotechnique*, 36(1), 65-78.

## **Chapter 4 Dynamic shear characteristics of clinker ash**

### **4.1 Dynamic deformation characteristics through small strain cyclic triaxial testing**

#### **4.1.1 Outline**

The stress-strain relationship of soil as a ground material shows strong nonlinearity according to the generated shear strain amplitude, and this makes it hard to perform analysis. Therefore, equivalent linear analysis using an equivalent linear model is often used. The basic input conditions of equivalent linear analysis are the equivalent shear stiffness factor and the damping ratio factor, which are known as the dynamic deformation coefficients for soil. In order to accurately predict the earthquake behavior of ground through analysis, it is necessary to obtain the dynamic deformation coefficients of the soil through laboratory testing and to properly evaluate the results. Therefore, in this section, the equivalent Young's modulus and the historical damping ratio of clinker ash were determined using a cyclic triaxial test device in order to clarify the dynamic deformation characteristics of clinker ash. In addition, from the test results, fitting between the model values and experimental values was also evaluated using the Hardin-Drnevich<sup>1)</sup> model.

#### **4.1.2 Specimen preparation and test conditions**

Samples were first placed in water in a vacuum chamber for up to 3 days in order to remove as much air as possible. The specimens had a diameter of 10cm and a height of 20cm and were prepared

using the water pluviation method. In order to reach a degree of compaction of 90%, the mold was struck with a hammer once the sample had been inserted to reach the set density. Table 4.1 shows the test conditions.

Table 4.1 Test conditions

Sample	$D_c$ (%)
CC	90
CD	
CE	

### 4.1.3 Outline of test equipment

#### 1) Test equipment

The dynamic deformation tests were performed using a hydraulic servo-type cyclic triaxial testing machine fitted with a Local Deformation Transducer (LDT). The full view of the testing machine is shown in Figure 4.1, and the accuracy of each measuring instrument is given in Table 4.2.

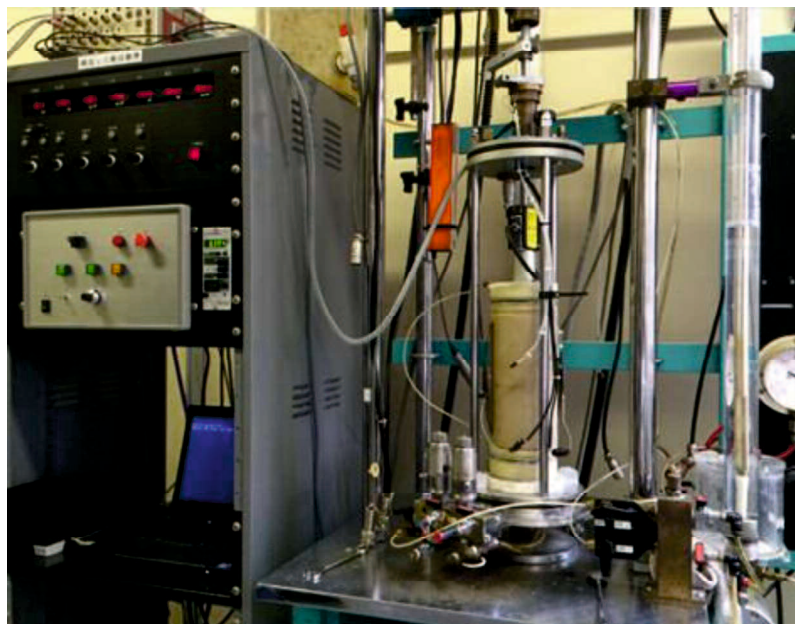


Figure 4.1 Cyclic triaxial apparatus

Table 4.2 Accuracy of each measurement device

Gauge	Type	Model	Max
Axial Load	Strain Gauge	TCLZ-100KA	0.98kN
Pressure	Strain Gauge	PW-10	1MPa
Pore Water Pressure	Strain Gauge	PW-10	1MPa
Axial Displacement	Strain Gauge	CDP-50	50mm

The main parameters in these tests are axial deviator stress  $q$ , mean effective stress  $p$ , cyclic deviator stress  $\sigma_d$  and cyclic shear ratio  $\sigma_d/2\sigma_c'$ . Axial deviator stress and mean effective stress were calculated as follows:

$$q = \sigma_a' - \sigma_r' \quad (4.1)$$

$$p' = \frac{\sigma_a' + 2\sigma_r'}{3} \quad (4.2)$$

## 2) Displacement gauge (outline of LDT)

In carrying out the dynamic deformation tests in this study, an LDT was used. The outline of the LDT is shown in Figure 4.2. The LDT is an axial strain measuring device attached to the side of the specimen, and it is possible to accurately measure very small strains with less influence of bedding errors.



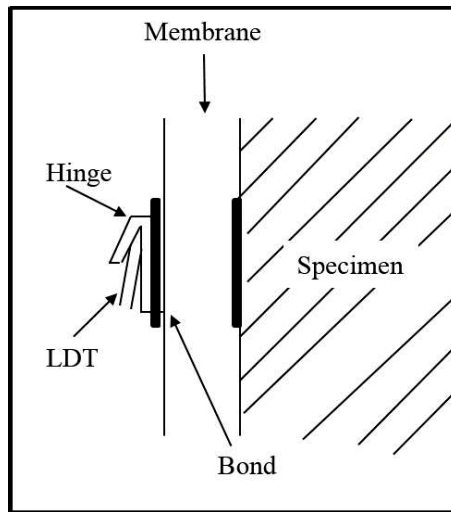


Figure 4.2 Outline of LDT displacement gauge

### 3) Calibration of LDT displacement gauge

In order to accurately measure the amount of minute strain, it is important to use an elaborate displacement gauge and perform precise calibration. Therefore, in this study, calibration was carried out using a highly accurate calibration apparatus with a micrometer as shown in Figure 4.3 (representative example). An example of a state where calibration of LDT is being performed is shown in Figure 4.4.

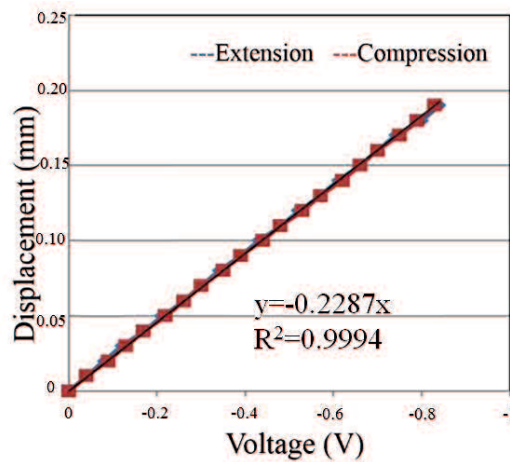


Figure 4.3 LDT calibration (amp range 50)

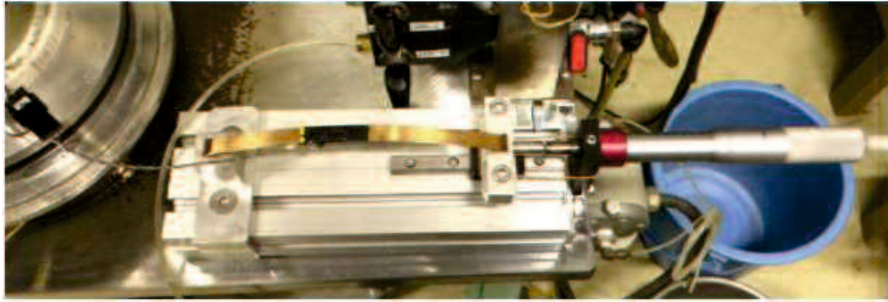


Figure 4.4 LDT calibration

#### 4) Reasons for use of LDT displacement gauge

When attempting to measure the axial displacement by compression with a conventional external displacement gauge method, unavoidable errors occurring in each part of the test equipment can be considered:

1. Deformation of the loading plate
2. Deformation of load cell and gain cushion
3. Misalignment of specimen cap
4. Deformation of loading piston
5. Deformation and movement of the displacement gauge touch panel
6. Piston friction

Care must be taken to minimize these errors. An example of the most frequent causes of these errors is given in in Figure 4.5. In order to eliminate these errors, it is possible to eliminate the influence of the bedding error by using the LDT displacement gauge, and perform accurate experiments.



a) End surfaces are not parallel

b) Disturbed by molding

c) End surface is not smooth

Figure 4.5 Examples of bedding errors<sup>2)</sup>

#### 4.1.4 Samples used and test procedure

The clinker ash samples CC, CD and CE were used in these experiments. The specimens had a height of 20cm and a diameter of 10cm, prepared to a degree of compaction  $D_c = 90\%$ . The consolidation condition was set to an isotropic consolidation state with an effective confining pressure  $\sigma'_c = 100\text{kPa}$  for each sample and cyclic loads of eleven cycles with a sinusoidal waveform of frequency  $f=0.1\text{Hz}$  were applied to the specimen under non-drainage conditions. After cyclic shearing, the excess pore water pressure was dissipated by allowing a drainage state. Figure 4.6 shows the dynamic deformation test method using the cyclic triaxial testing device.

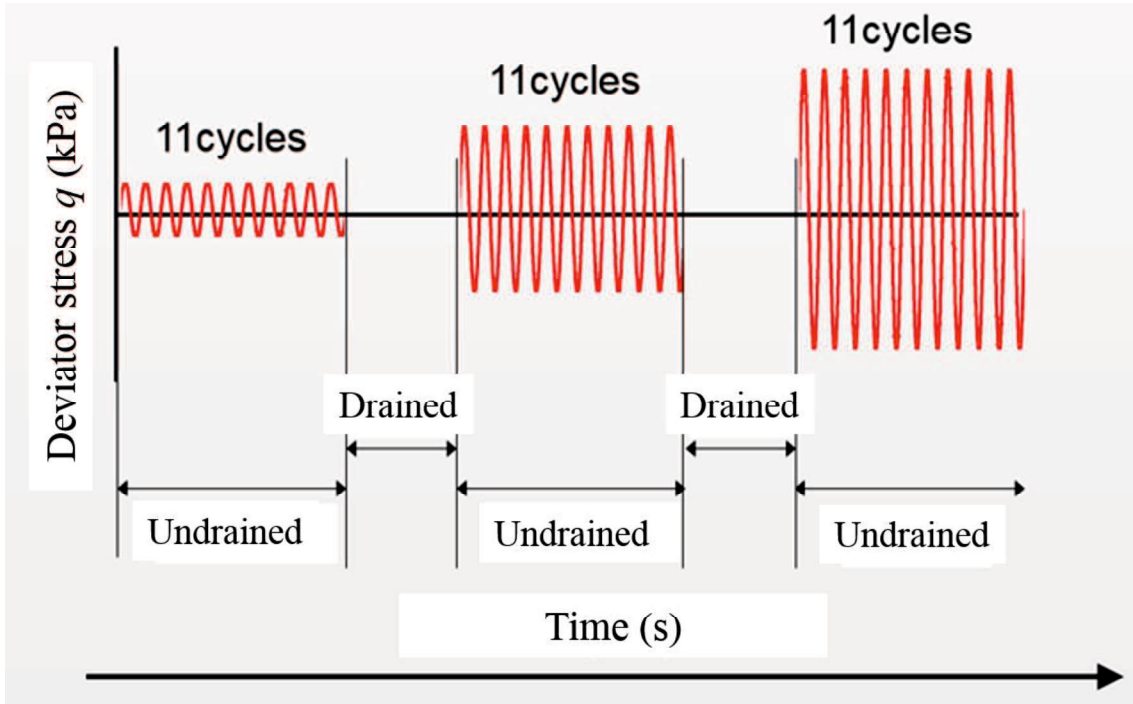


Figure 4.6 Outline of dynamic deformation test

The damping ratio is calculated as follows. The damping energy  $\Delta W$  during one cycle is the area of the hysteresis loop produced by the axial deviator stress  $q$  and the axial strain ( $\epsilon_a$ ). Since we collect about 2400 units of data per cycle in this study, the historical curve between 2 plots can be assumed to be a straight line, and so the area of the hysteresis loop between 2 plots is equivalent to the area of the trapezoid. The damping energy is obtained by subtracting the overlapping area from the sum of the area of the trapezoid.

The damping ratio  $h$  was calculated using Equation 4.4.

$$W = \frac{1}{4} q * (\epsilon_a) \quad (4.3)$$

$$h = \frac{1}{2\pi} * \frac{\Delta W}{W} * 100 \quad (4.4)$$

The equivalent Young's modulus is calculated as follows:

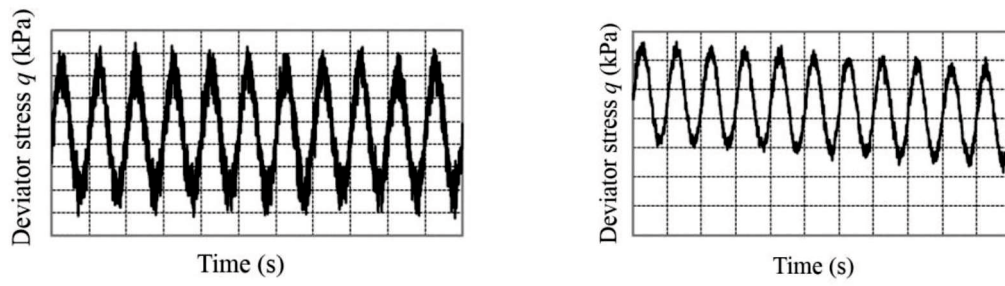
$$\sigma_d = \frac{q}{2A_n} * 10 \quad (4.5)$$

$$E_{eq} = \frac{\sigma_d}{(\varepsilon_a)_{SA}} * \frac{1}{10} \quad (4.6)$$

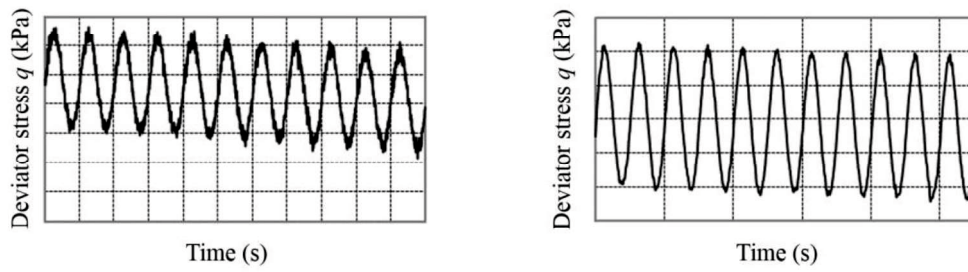
#### 4.1.5 Organization of results

In this study, the data obtained by the dynamic deformation test was subjected to waveform processing, and the equivalent Young's modulus  $E_{eq}$  and the damping ratio  $h$  were calculated. In order to remove the noise included in the experimental values, waveform processing (fast Fourier transform) of the data was performed using a computer.

Figures 4.7 (a)-(b) and 4.8 (a)-(b) show the time history of the axial deviator stress  $q$  and the axial strain  $(\varepsilon_a)_{SA}$  and the waveform of the historical curve obtained by the dynamic deformation test with a loading frequency of 0.1Hz. Experimental values and values after the waveform processing are shown. From these figures, comparing the waveforms before and after the waveform processing, it is found that the noise generated during the experiment is removed after the processing. Therefore, the data can be improved by performing waveform processing work.

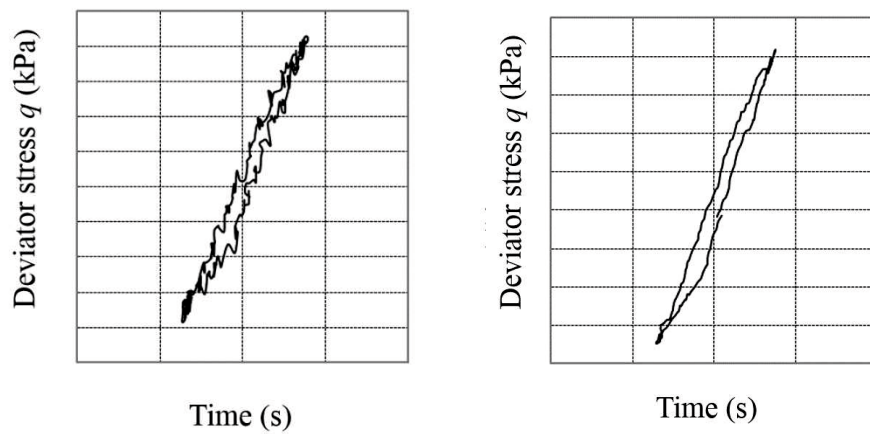


(a) Before waveform processing



(b) After waveform processing

Figure 4.7 Time history of axial deviator stress and axial strain



(a) Before waveform processing

(b) After waveform processing

Figure 4.8 Hysteresis loop

#### 4.1.6 Dynamic deformation characteristics

##### 1) Equivalent Young's modulus and damping ratio

Figures 4.9 and 4.10 show the equivalent Young's modulus  $E_{eq}$ , damping ratio  $h$  and the single amplitude axial strain  $(\varepsilon_a)_{SA}$ , at the 5th and 10th cycles. As shown in Figure 4.9, the damping ratio shows similar values, regardless of the type of clinker ash. In addition, Figure 4.10 also shows the results of Toyoura sand prepared with the same degree of compaction for comparison. Comparing Toyoura sand and clinker ash from each curve, the initial equivalent Young's modulus shows smaller values for all clinker ash samples. Also, looking at the single amplitude axial strain where the equivalent Young's modulus begins to decrease, Toyoura sand begins to decrease from the single amplitude axial strain of about 0.001%, whereas the clinker ash decreases to about 0.01% at the same equivalent Young's modulus. From this, it can be seen that clinker ash is a material with a wider elastic range than Toyoura sand.

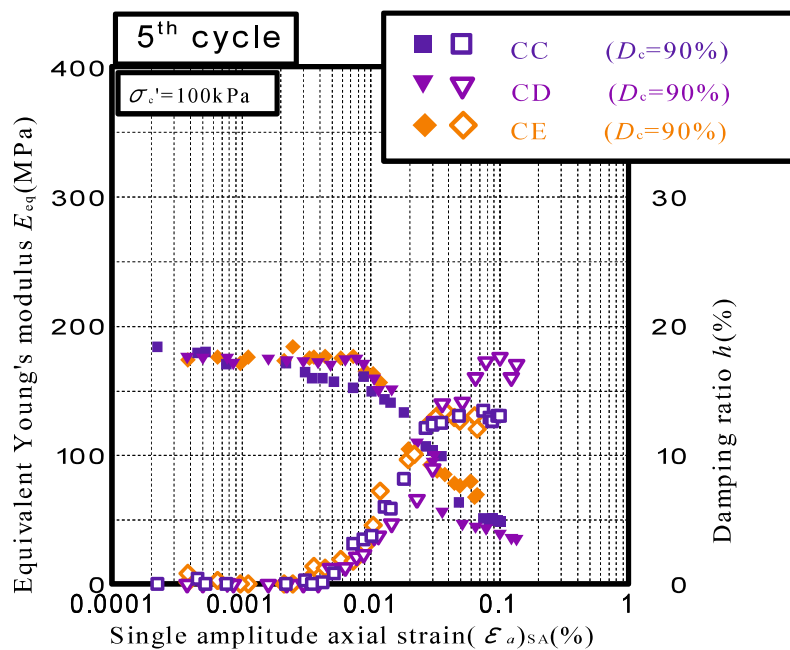


Figure 4.9 Dynamic deformation characteristics (5<sup>th</sup> cycle)

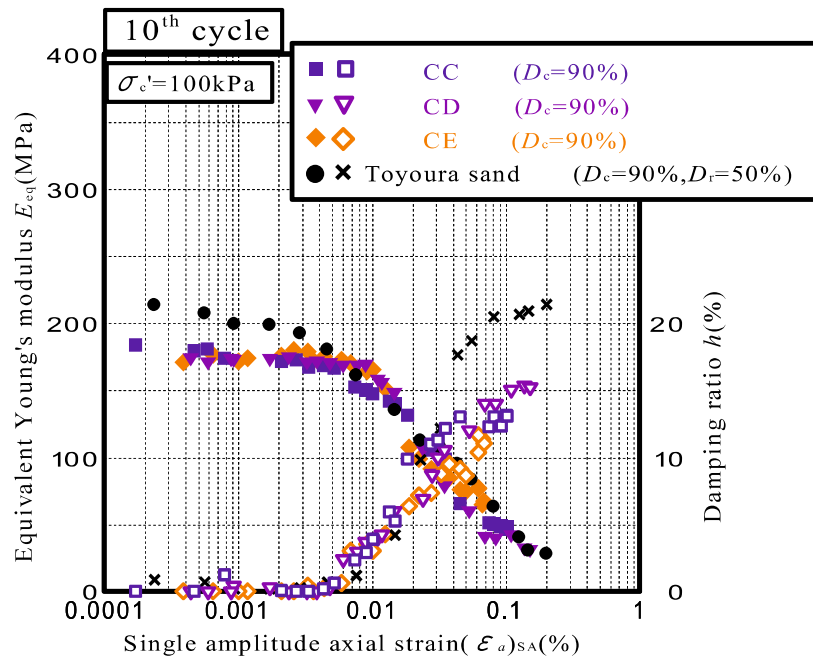


Figure 4.10 Dynamic deformation characteristics (10<sup>th</sup> cycle)

Also, as shown in Figure 4.10, for the damping ratio  $h$ , in the strain range where the single amplitude axial strain is less than 0.01%, there is no big difference between clinker ash and Toyoura sand. However, in the strain range where the single amplitude axial strain is larger than 0.01%, Toyoura sand tends to be higher than the clinker ash. The reason for this is that as the level of strain increases in Toyoura Sand, the decrease in rigidity due to liquefaction becomes remarkable, and so it is considered that  $h$  increases as a result.

## 2) $E/E_0 - (\varepsilon_a)_{SA}$ curve

Figure 4.11 shows the relationship between the equivalent Young's modulus  $E_{eq}$  normalized with the initial equivalent Young's modulus  $E_0$  and the single amplitude axial strain  $(\varepsilon_a)_{SA}$ . From this figure it can be seen that the equivalent Young's modulus of Toyoura sand began decreasing from about 0.0005% in single amplitude axial strain, while clinker ash maintained the equivalent Young's modulus up to 0.004% in single amplitude axial strain. From the above, it can be noted that clinker ash is a



material capable of suppressing a decrease in equivalent Young's modulus in the minute strain region and exhibits a wide elastic range.

This is considered to be attributed to the complicated particle shape of clinker ash compared with Toyoura sand. From the complicated particle shape of clinker ash, it is presumed that the particles are meshed with each other during consolidation and the equivalent Young's modulus is maintained to the vicinity of a single amplitude axial strain of 0.01%.

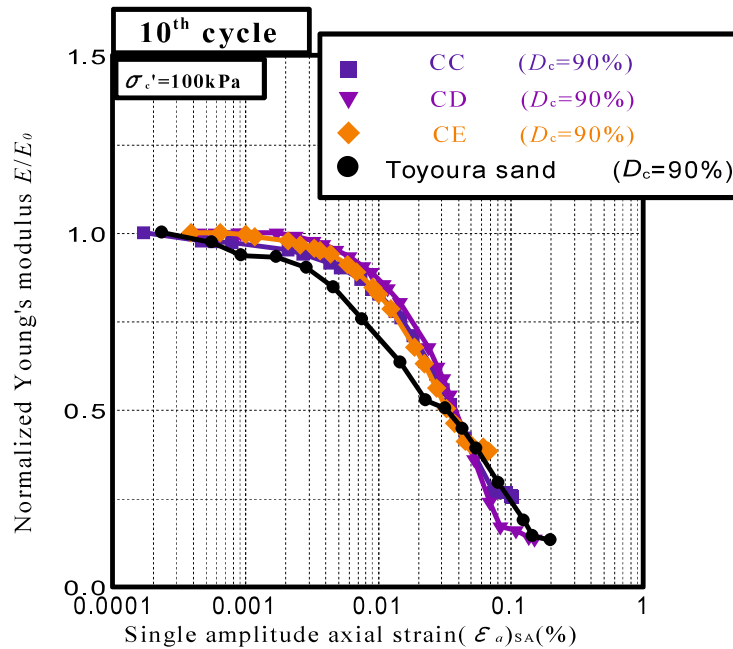


Figure 4.11  $E/E_0 - (\varepsilon_a)_{SA}$  curves (10th cycle)

#### 4.1.7 Hardin-Drnevich model

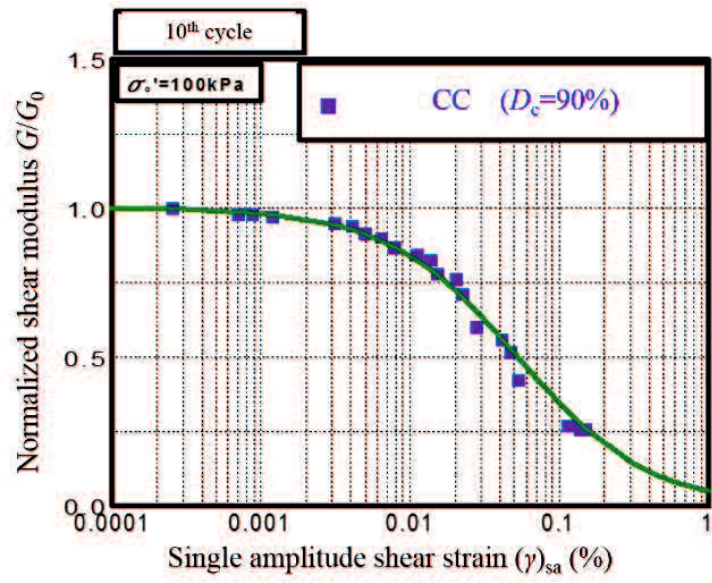
In modeling dynamic deformation characteristics, we adopted an adaptation of the Hardin-Drnevich model<sup>1)</sup> (hereafter abbreviated as HD model).  $G$  and  $h$  are represented by the Equation 4.7 and 4.8.

$$G/G_0 = 1/(1 + r/r_r) \quad (4.7)$$

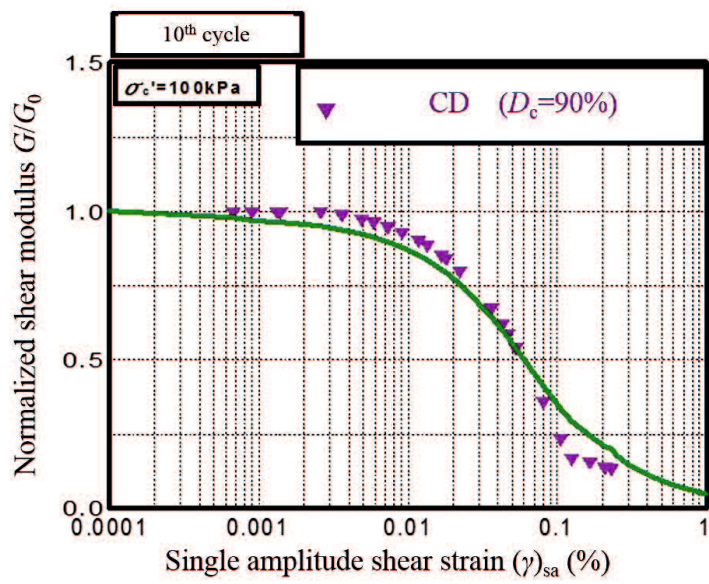
$$h = h_{max}(1 - G/G_0) \quad (4.8)$$

Here,  $\gamma_r$  is the reference strain and  $h_{max}$  is the maximum damping ratio.

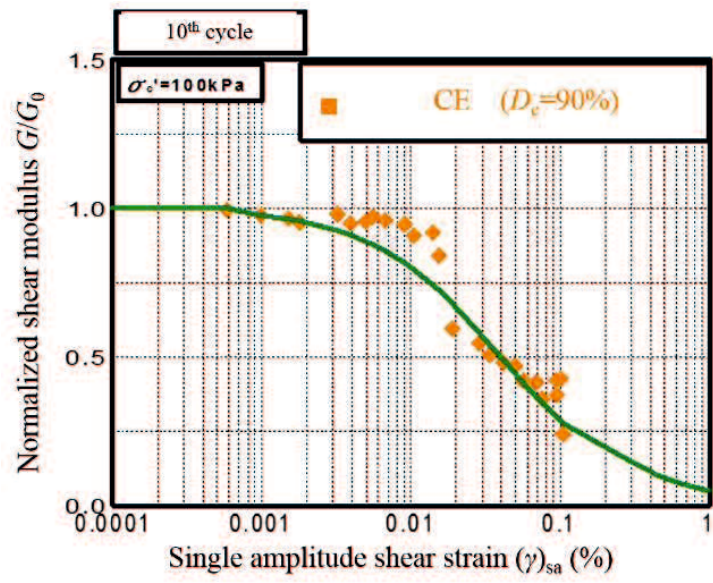
In this model, dynamic deformation characteristics can be expressed with two parameters  $h_{max}$  and  $\gamma_r$ , and these are often used as a method for evaluating experimental values. Therefore, the dynamic deformation characteristics of clinker ash obtained in this study are also evaluated using the HD model. The results are shown in Figures 4.12 (a)-(c) and Figures 4.13 (a)-(c). According to Figures 4.12 (a)-(c), the  $G/G_0 - \gamma$  curve varies depending on the coal type, but it is found that the experimental values and the HD models show close values for all clinker ash. Also, in Figures 4.13 (a)-(c), it can be seen that the experimental values and the HD model of the  $h - G/G_0$  curve show larger values in the experimental values than in the model for all coal types. This is considered to be due to a disadvantage with the HD model in that the damping ratio decreases dramatically as the strain increases. However, although there are some discrepancies in both Figures 4.12 (a)-(c) and Figures 4.13 (a)-(c), the experimental values and model values are close to each other as a whole, and by using the HD model it is thought that experimental values can be expressed.



(a) CC

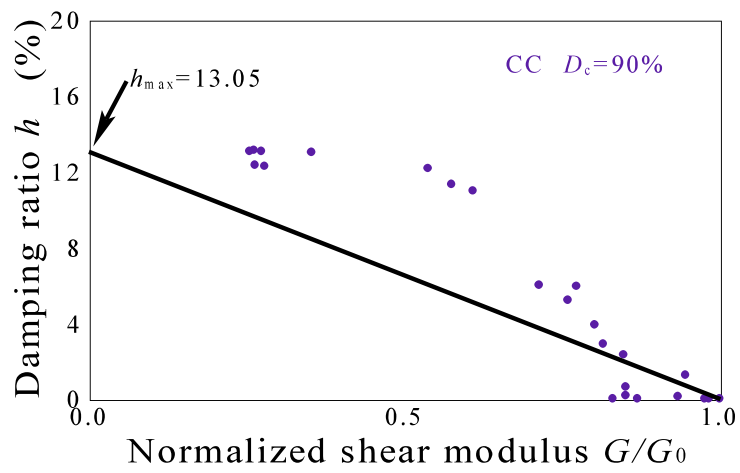


(b) CD

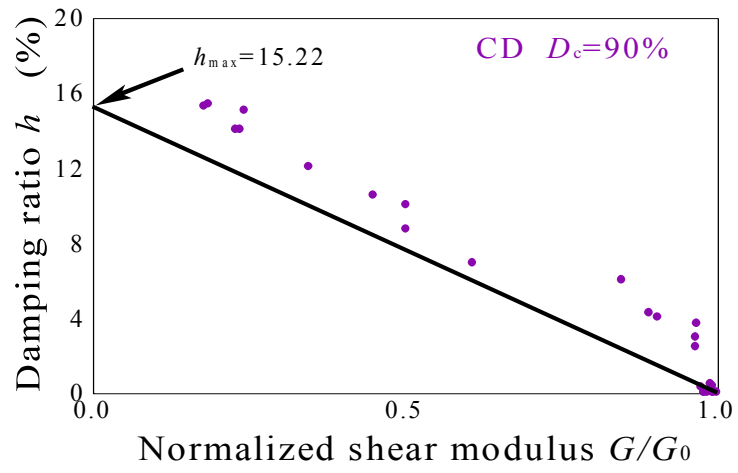


(c) CE

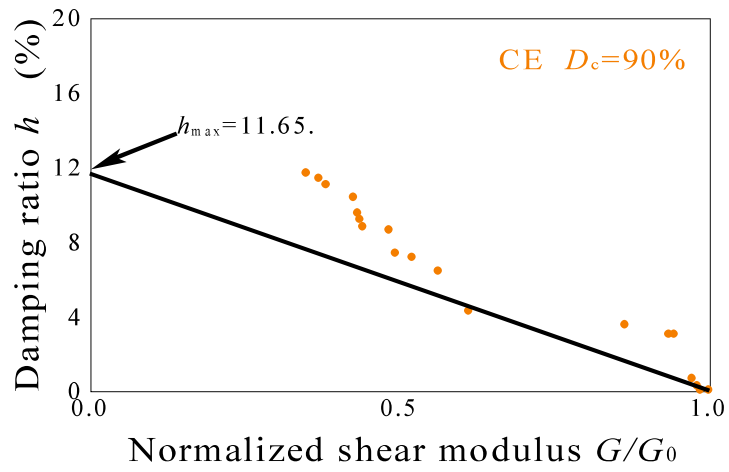
Figure 4.12 Experimental results and HD model



(a) CC



(b) CD



(c) CE

Figure 4.13 Experimental results and HD model

## 4.2 Initial shear rigidity characteristics through bender element testing

### 4.2.1 Outline of test equipment and method of measurement

The bender element test (BE test) is a test developed by Shirley and Hampton<sup>3)</sup> in which the initial shear modulus at very low strain can be obtained by measuring the velocity of a shear wave sent through a specimen. Bender elements are made of thin piezoceramic material with conductive plates which stretch or compress when a voltage pulse is received which in turn generates a voltage. Figures 4.14 and 4.15 show schematic diagrams of the wiring of the bender elements, the direction of deformation of the bender elements and the movement of the voltage. Figure 4.14 shows generation of a shear wave whilst Figure 4.15 shows the generation of a compression wave, known as the sending bender element (a) and the receiving bender element (b) respectively. When a voltage pulse is generated in the sending bender element, the element deforms in the direction shown in the figure. The deformation of the element is transmitted through the specimen as a shear wave or compression wave and when received by the receiving element another voltage is generated.

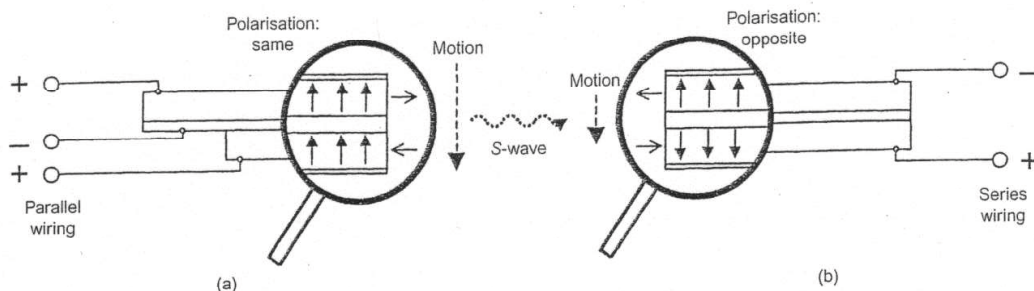


Figure 4.14 Schematic diagram of shear wave bender elements<sup>4)</sup>

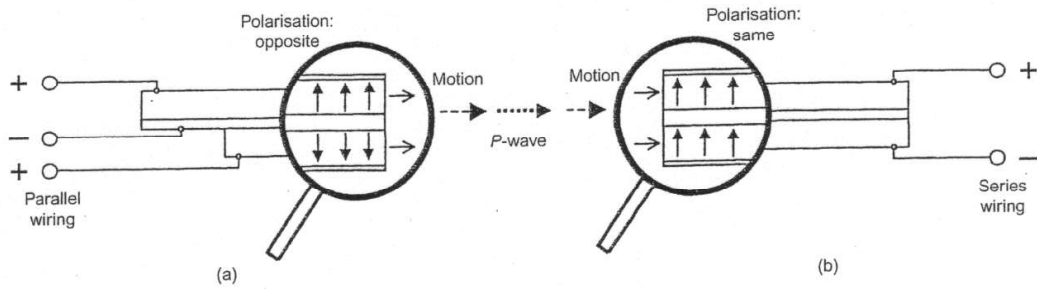


Figure 4.15 Schematic diagram of compression wave bender elements<sup>4)</sup>

In this research, the bender elements were set up to generate a shear wave. Figures 4.16 (a)-(b) show diagrams of the bender elements used in this research with the sending bender element attached to the bottom pedestal and the receiving bender element attached to the top cap. Also, the bender elements used in this research were self-monitoring style elements with the voltage generated by deformation of the sending element taken as the input voltage. The maximum voltage is 75V and the maximum water pressure is 1.0MPa.

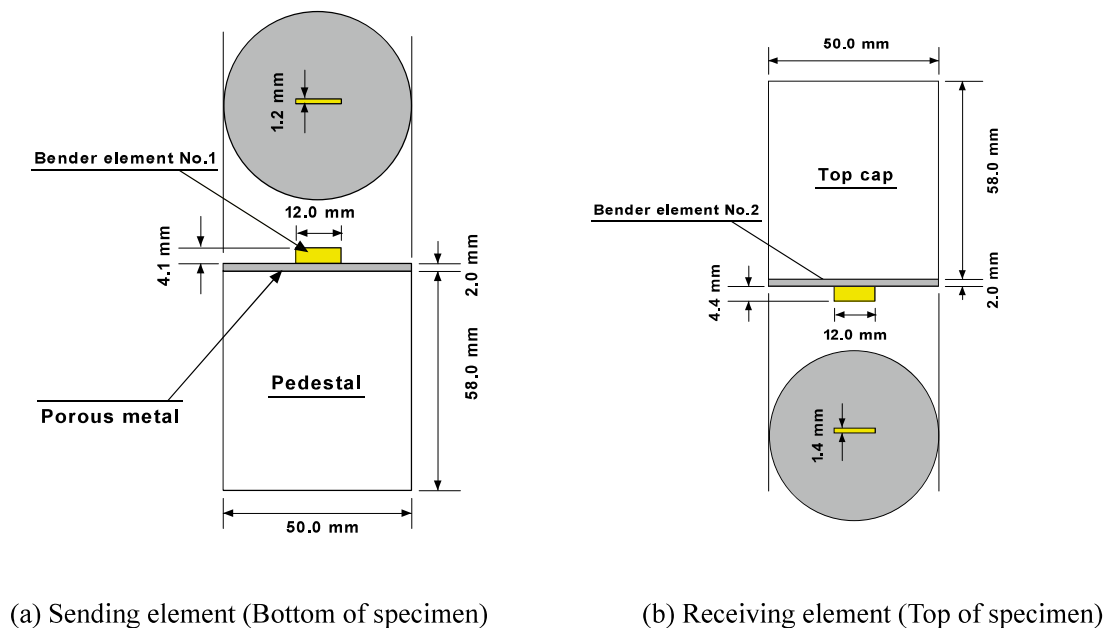


Figure 4.16 Measurements of elements

The bender element test apparatus used in this research was a typical triaxial compression shear test device with bender elements fitted in the bottom pedestal and top cap. Figure 4.17 is a diagram of the bender element triaxial test apparatus.

1. The input voltage, input waveform and frequency are set by the function generator (L)
2. The amplification factor of the input voltage is set by the voltage amplifier (M)
3. Through operation of the computer (PC), a trigger signal is sent to the function generator (L) and an input voltage is generated. The output voltage is amplified by a set factor by the voltage amplifier (M) and then deforms the sending bender element (H) set in the bottom pedestal of the apparatus.
4. The voltage generated in the sending element (H) and the receiving element (G), set in the top cap, are obtained through an oscilloscope (N).
5. The voltage data obtained through the oscilloscope (N) is converted and saved to the computer (PC).



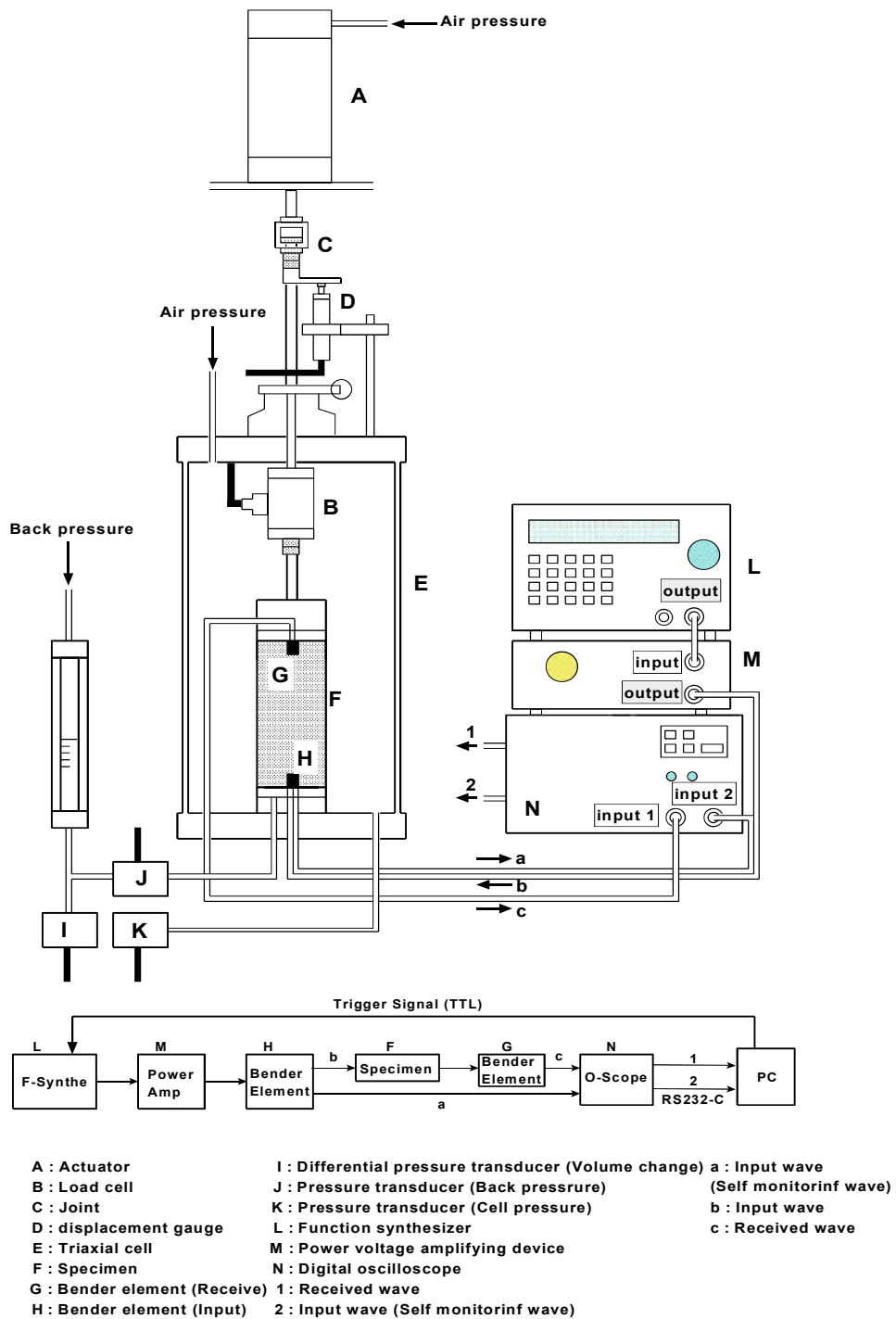


Figure 4.17 Bender element test apparatus

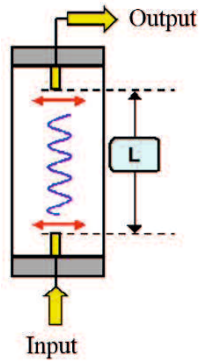


Figure 4.18 Diagram of bender element test

In the bender element test, the shear wave velocity is calculated by using the shear wave propagation time and the specimen length. Figure 4.18 shows a diagram of a specimen with bender elements set in the test apparatus, along with the shear wave. If the distance between the elements is taken as  $L$  (m), and the time taken for the sent wave to reach the receiving bender (shear wave propagation time) as  $\Delta t$  (s), then the shear wave velocity  $V_s$  (m/s) can be calculated using Equation 4.9, and the shear modulus  $G$  (N/m<sup>2</sup>) can be calculated using Equation 4.10 with the wet unit volume weight  $\rho_t$  (kg/cm<sup>3</sup>) and  $V_s$  (m/sec).

$$V_s = \frac{L}{\Delta t} \quad (4.9)$$

$$G = \rho_t \cdot V_s^2 \quad (4.10)$$

The time used in calculation of the shear wave velocity is calculated using equation 4.11<sup>5)</sup>.

$$\Delta t = \frac{\Delta t_s + \Delta t_p}{2} - \Delta t_d \quad (4.11)$$

Here,  $\Delta t_s$  is the time from the start of the input wave to the received wave,  $\Delta t_p$  is the time from the first peak of the input wave to the first peak of the received wave and  $\Delta t_d$  is the delay time of the system.

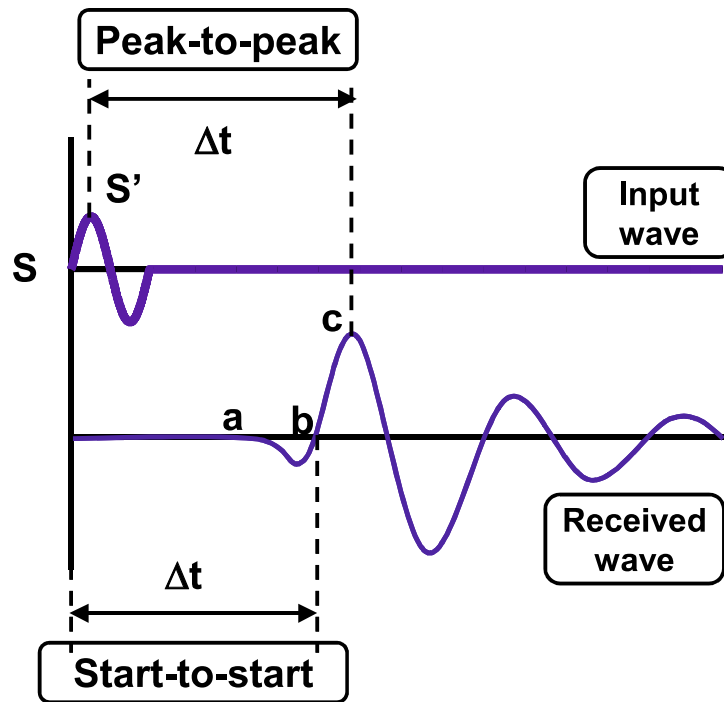


Figure 4.19 Calculation of shear wave propagation time with Peak-to-Peak and Start-to-Start

#### 4.2.2 Bender element test method

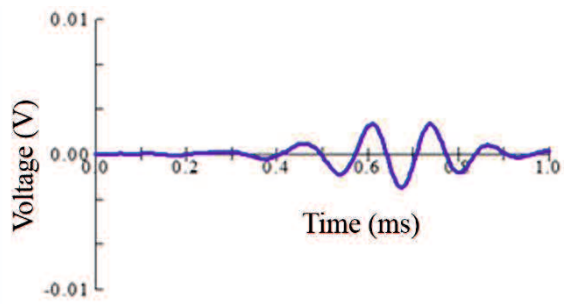
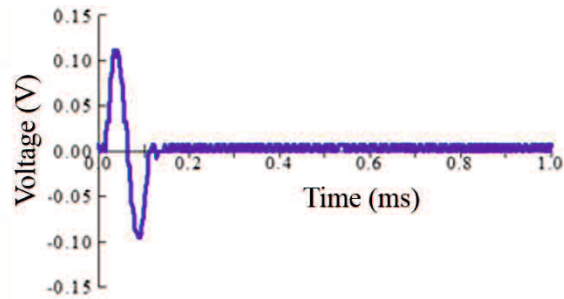
Table 4.3 shows the test conditions conducted in this research. Specimens with degrees of compaction of 85% and 90% were prepared using the water pluviation method, whilst those with degrees of compaction of 100% were compacted in 5 layers using a 111g rammer and then the specimen was frozen before being placed in a membrane. In order to saturate the specimen, a back pressure of 200kPa was applied with an effective confining pressure of 10kPa and left for over two hours before the B value was calculated. If the B value was at least 0.95 then consolidation was

performed. Effective confining pressures were applied as shown in the table until isotropic consolidation was complete and then the bender element test was conducted. The sent wave was a sine wave and a voltage of  $V=\pm 10V$  was used, with waves sent at frequencies of  $f=10, 15$  and  $20Hz$ . The propagation length  $L$  was taken as the distance between the tips of the elements and the propagation time was calculated as shown earlier. The shear modulus is taken as the average value from the shear velocities calculated at each frequency.

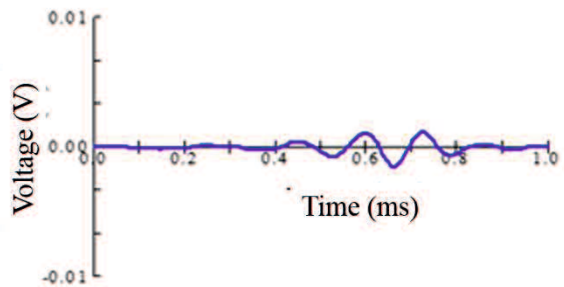
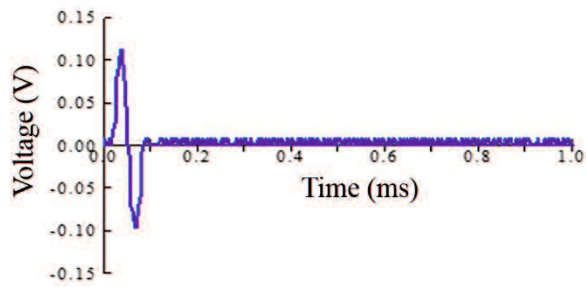
Table 4.3 Test conditions

Sample	Degree of compaction $D_c$ (%)	Confining pressure $\sigma_c'$ (kPa)
CA	85	50, 100, 200
	90	
	100	
CB	90	50, 100, 200, 400
CC	85	50, 100, 200
	90	
CD	90	50, 100, 200
CE	85	50, 100, 200
	90	
	100	
CF	90	50, 100, 200, 400
Toyoura	90	50, 100, 200

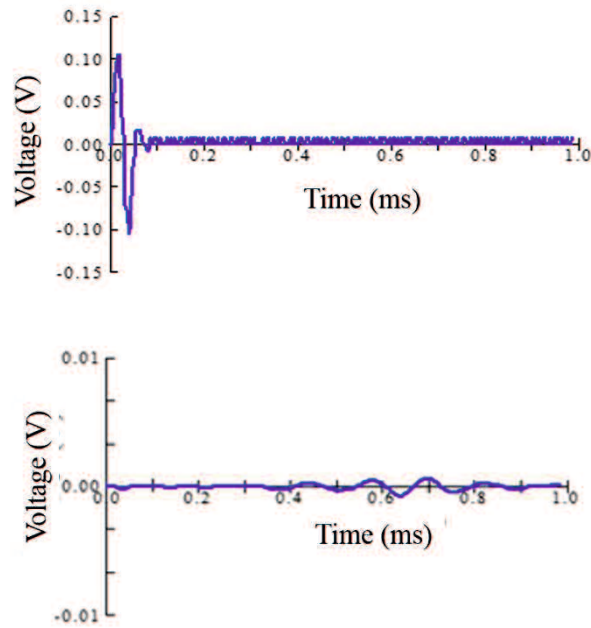
Figures 4.20 (a)-(c) show examples of sent and received waves at each frequency for CF.



(a) CF  $\sigma_c = 100\text{kPa}$ ,  $f = 10\text{kHz}$



(b) CF  $\sigma_c = 100\text{kPa}$ ,  $f = 15\text{kHz}$



(c) CF  $\sigma_c = 100\text{kPa}$ ,  $f = 20\text{kHz}$

Figure 4.20 Examples of sent and received waves at each frequency

### 4.2.3 Results

Figure 4.21 shows the relationship between the initial shear modulus and the confining pressure for specimens compacted to 90% degree of compaction. For comparison, the results for Toyoura sand are also shown. As can be seen in the figure, it can be confirmed that the initial shear modulus increases along with an increase in confining pressure, in the same way as natural sand. In comparison with Toyoura sand, CA and CC show results close to Toyoura, however clinker ash shows lower values of initial shear modulus.

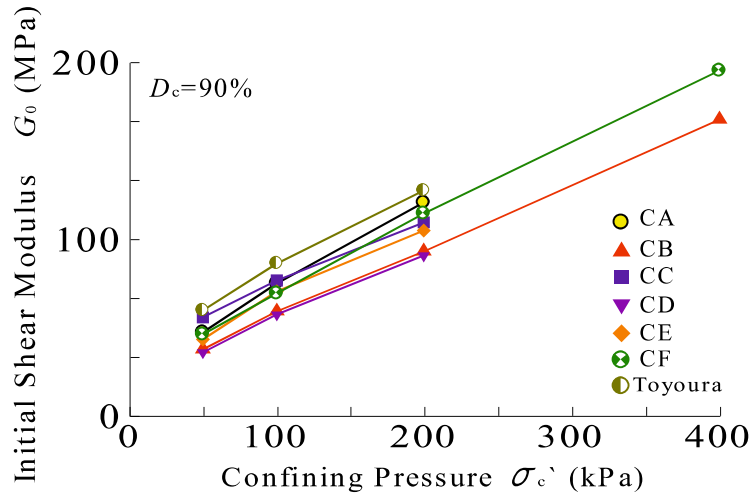


Figure 4.21 Relationship between initial shear modulus and confining pressure

In order to observe the effect of loading and unloading on the initial shear modulus, the confining pressure was raised to 400kPa and then reduced back to 200kPa, 100kPa and 50kPa in tests on CB and CF. Figure 4.22 shows the results. It can be seen that when unloading, larger values for the initial shear modulus are obtained than in the loading stage. It can be thought that this is due to the fact that the density of the specimen is increased.

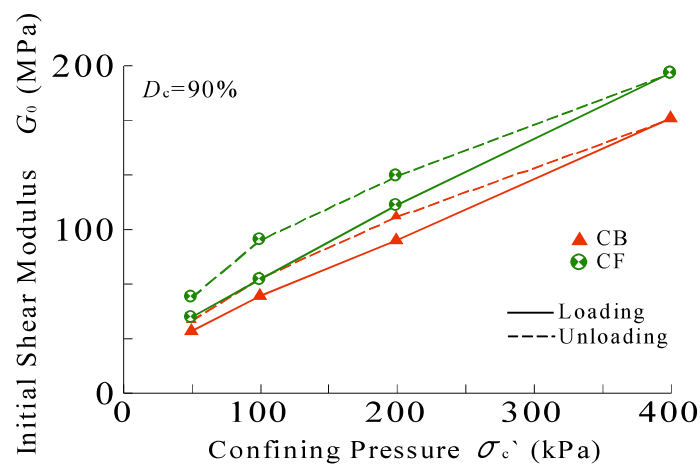


Figure 4.22 Relationship between initial shear modulus and confining pressure (loading and unloading)

Figure 4.23 shows the effect of degree of compaction on the initial shear modulus. From the figure, it becomes clear that as the degree of compaction increases there is a marked increase in the initial shear modulus.

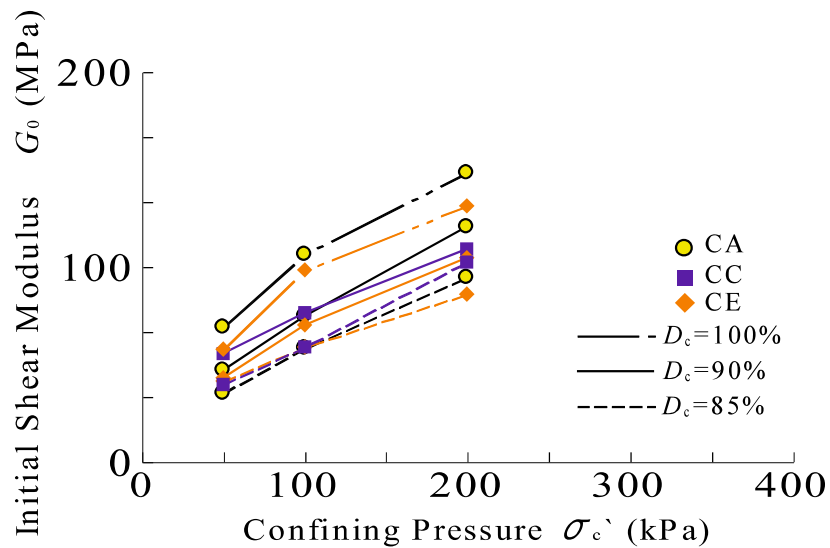


Figure 4.23 Relationship between initial shear modulus and confining pressure at various  $D_c$

In Figure 4.24 the relationship between the gravel content and initial shear modulus is shown. The green plots show results for 50kPa, the blue plots for 100kPa and the red plots for 200kPa. Although there are some slight discrepancies, there is a trend for the initial shear modulus to increase along with an increase in gravel content up to 30% at all confining pressures. However, above a gravel content of 30% there is almost no change in initial shear modulus.



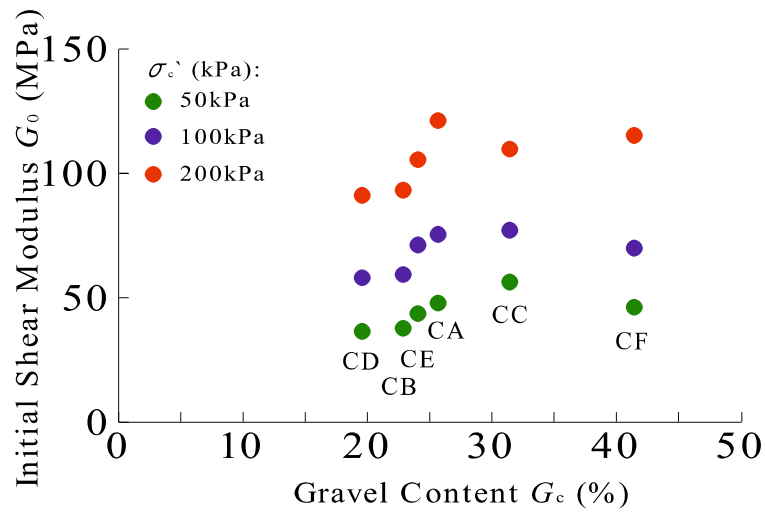


Figure 4.24 Relationship between initial shear modulus and gravel content.

In Figure 4.25 the relationship between the initial shear modulus and the fines content is shown. Again, although there is not a huge effect, a slight decrease in initial shear modulus can be observed as fines content increases.

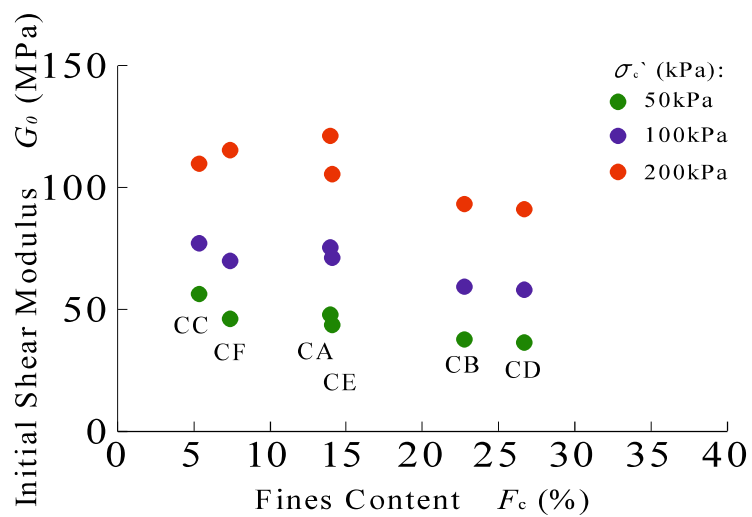


Figure 4.25 Relationship between initial shear modulus and fines content

#### 4.2.4 Comparison of results with other experiments

A comparison of results for the initial shear modulus gained from bender element tests and those gained from other experiments are shown in Figure 4.26. The degrees of compaction shown are those from the given tests and the values in the parentheses are those from the bender element tests. The other test types given are HT=Hollow Torsional and CT=Cyclic Triaxial.

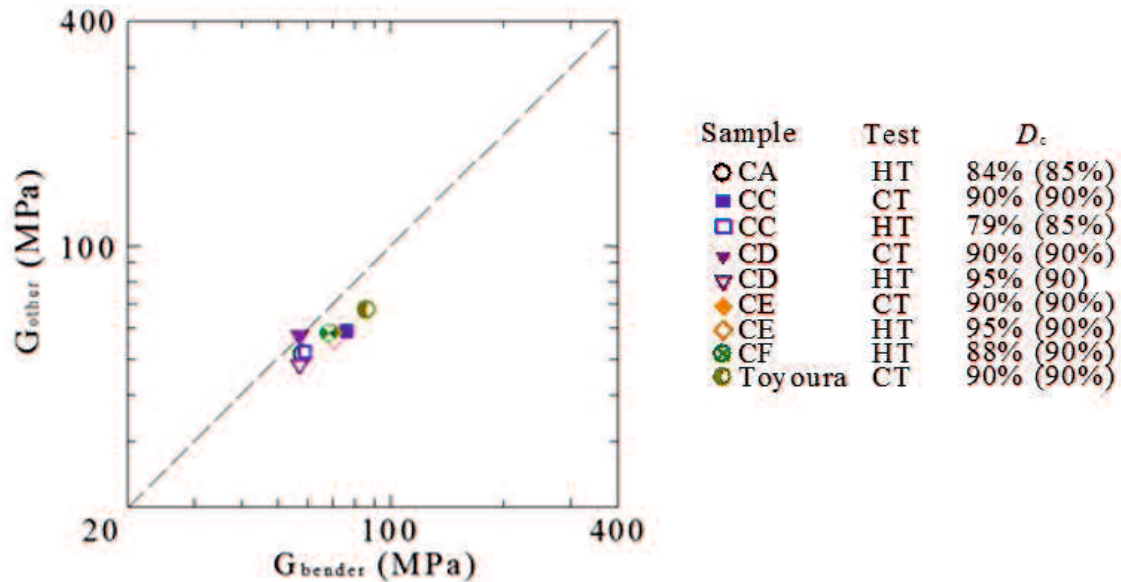


Figure 4.26 Comparison of values gained from bender tests and other tests

The initial shear modulus for the triaxial dynamic deformation tests was calculated using Equation 4.12:

$$G = \frac{E}{2(1+\nu)} \quad (4.12)$$

The Poisson ratio used in this research was 0.5. The results for CD are almost equal for the bender tests and other tests, however for the other results, the results from the bender element tests are slightly

higher than those gained from other tests. This trend is in line with previously conducted research on Toyoura sand, as shown in Figure 4.27.

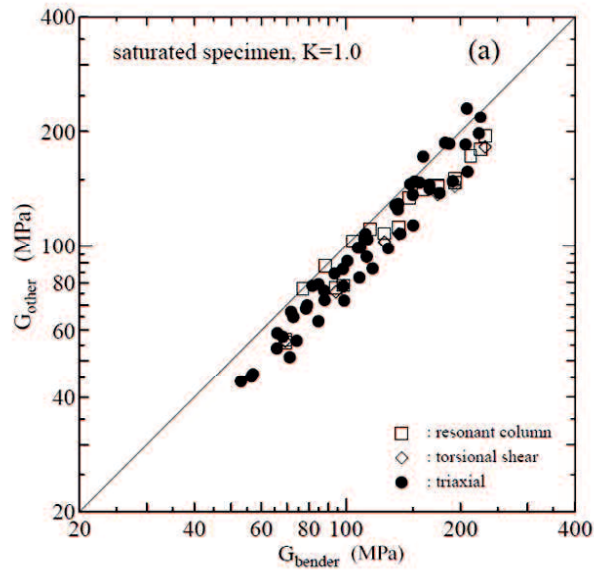


Figure 4.27 Comparison of results from bender tests and other tests<sup>6)</sup>

### 4.3 Liquefaction strength characteristics through cyclic triaxial testing

#### 4.3.1 Specimen preparation and test conditions

There has been increasing focus on liquefaction of soil due to earthquakes, however in the case of clinker ash so far there has mostly only been research<sup>7)</sup> conducted on loose state samples, and as such the liquefaction characteristics of dense clinker ash are also not yet very clear.

In order to ensure the specimen is as saturated as possible, the sample is first placed in de-aired water before being left in a vacuum chamber for 2-3 days in order to remove air. The specimen had a height of 30cm and a diameter of 15cm. For degrees of compaction  $D_c=85$  and 90%, the specimen was

prepared using the water pluviation method. For  $D_c=100\%$ , it was necessary to first prepare the specimen in a separate mold, before freezing it and placing in the membrane to thaw, as tamping the specimen inside the membrane could easily cause the membrane to tear, due to the angular shapes of clinker ash particles. The specimen was prepared in 10 layers using a tamper to reach  $0.5E_c$  as gained from compaction tests. Table 4.4 shows the test conditions for each of the experiments performed.

Table 4.4 Test conditions

Sample	$D_c$ (%)	$\sigma_d/\sigma_{2c}$	Number of Cycles $N$
CC	85	0.19	54
	85	0.28	14
	85	0.32	7
	85	0.36	5.2
	97	0.30	190
	97	0.37	44
	97	0.44	28
	97	0.51	7
CD	85	0.13	36
	85	0.16	19
	85	0.20	13
	85	0.23	5
	85	0.30	4
	99	0.30	209
	99	0.37	66
	99	0.45	55
	99	0.56	16
CE	85	0.17	22
	85	0.21	13.5
	85	0.23	12
	85	0.25	8
	85	0.30	7.5
	97	0.30	154
	97	0.38	58
	97	0.45	19
	97	0.54	17
Ube Masado	85	0.13	388
	85	0.15	44
	85	0.16	29
	85	0.18	12
	97	0.24	148
	97	0.26	39
	97	0.27	36
	97	0.30	19

### 4.3.2 Test equipment and test procedure

Undrained cyclic triaxial tests were carried out using the testing apparatus shown in Figure 4.28.

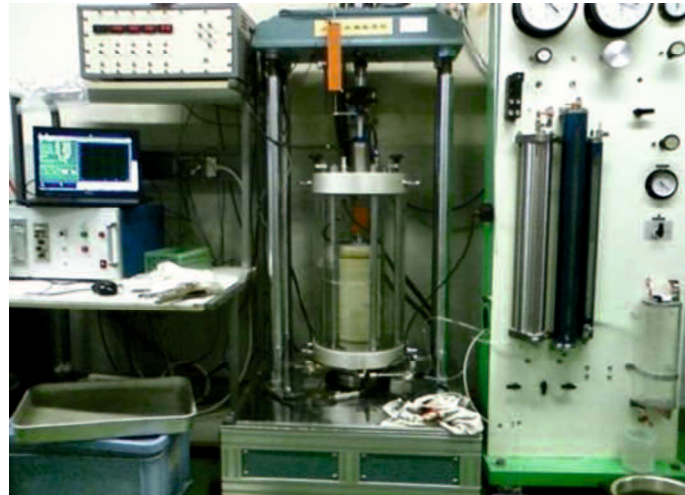


Figure 4.28 Cyclic triaxial testing apparatus

The deviator stress and mean effective stress are given as follows:

$$q = \sigma_a' - \sigma_r' \quad (4.13)$$

$$p' = \frac{\sigma_a' + 2\sigma_r'}{3} \quad (4.14)$$

Isotropic consolidation was carried out under an initial confining pressure of  $\sigma_c' = 100\text{kPa}$  and a load was applied with a frequency of  $f=0.02\text{Hz}$ . Liquefaction was taken to have occurred at a double amplitude axial strain of  $\varepsilon_{DA}=5\%$ .

### 4.3.3 Test results

Figure 4.29 shows an example of test results from cyclic triaxial testing. Some additional test data is given in Appendix D.

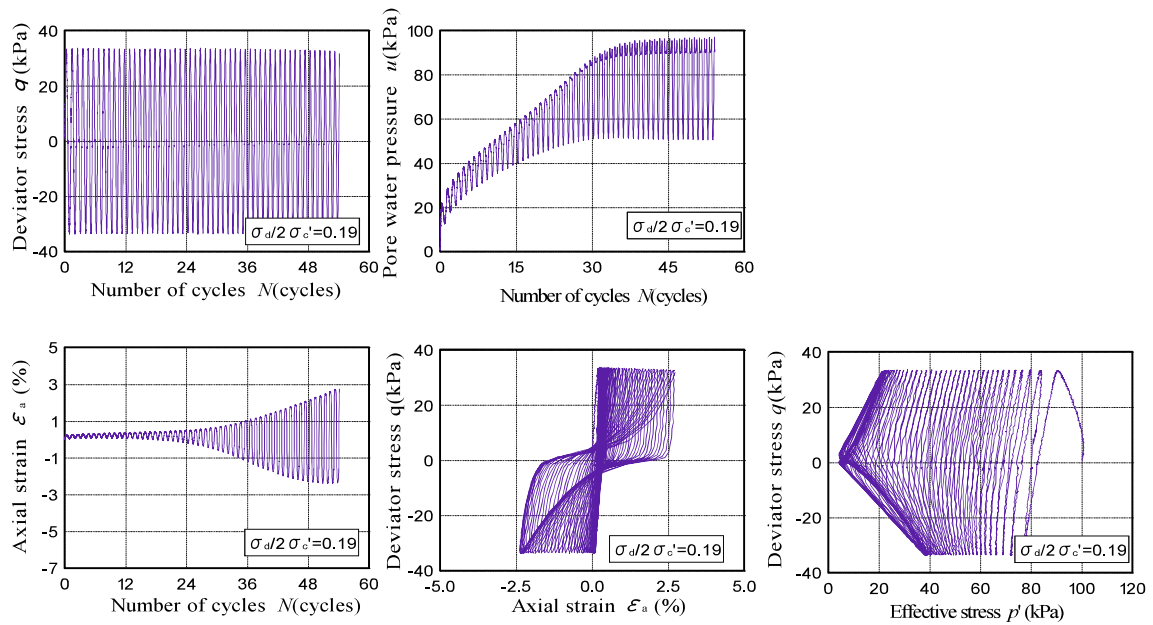


Figure 4.29 Cyclic test results for CC  $\sigma_d/2\sigma_c' = 0.19$   $D_c = 85\%$

As can be seen from the results, the mean effective stress does not fully reach zero, indicating that liquefaction does not completely occur with clinker ash. This could be due to the complex particle shapes, which interlock with each other and make it difficult for negative dilatancy to occur.

Figure 4.30 shows the relationship between the cyclic stress ratio  $\sigma_d/2\sigma_c'$  and the number of cycles  $N$  at which the double amplitude axial strain reaches  $\epsilon_{DA} = 5\%$  at degrees of compaction  $D_c = 85$  and 100%. For comparison, Ube Masado is also shown.

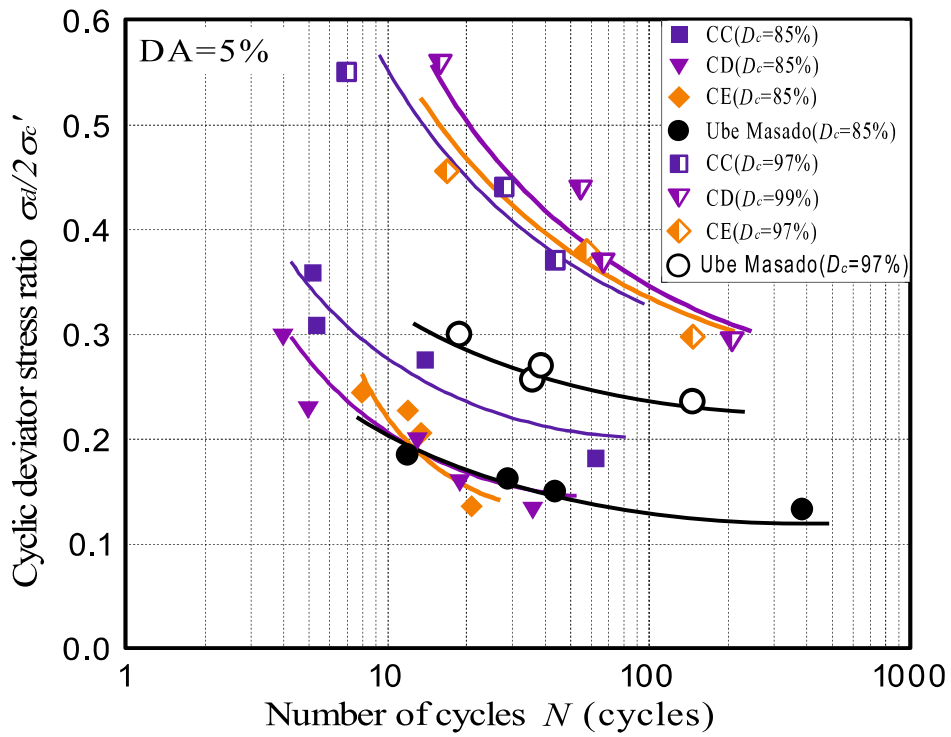


Figure 4.30 Relationship between  $\sigma_d / 2\sigma'_c$  and  $N$

As can be seen from the figure, in a loose state Ube Masado displays similar liquefaction strength to that of clinker ash. However, when the degree of compaction is increased to around  $D_c=97-99\%$ , a significant difference in liquefaction strength becomes apparent between the clinker ash samples and that of Ube Masado.

In order to show more clearly the influence of degree of compaction of the liquefaction strength of clinker ash, the relationship between liquefaction resistance  $R_{20}$  and degree of compaction  $D_c$  is shown in Figure 4.31. The liquefaction resistance  $R_{20}$  is the shear ratio at which liquefaction occurs on the 20<sup>th</sup> cycle for a specimen. As mentioned, at low density there is little difference between the liquefaction resistance for that of clinker ash and Ube Masado. CC shows slightly higher strength, although the reason for this has not yet been fully investigated.

When the specimens are compacted to over  $D_c=95\%$ , a clear difference in liquefaction resistance becomes apparent between all of the clinker ash samples and Ube Masado. The strength of the clinker ash samples become around 1.5 times that of Ube Masado, and the increase in degree of compaction from  $D_c=85\%$  to around  $D_c=97\%$  leads to an increase in strength of the clinker ash from between 1.5 to 3 times as much.

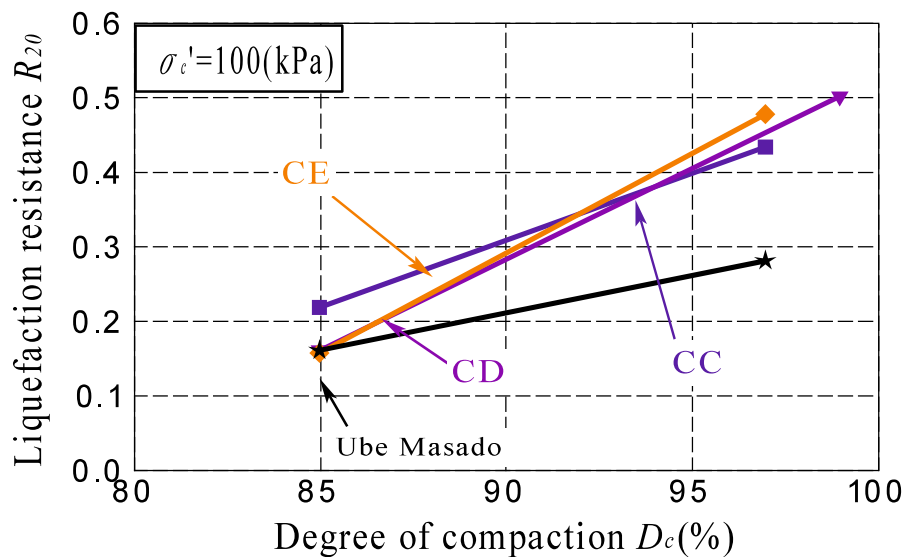


Figure 4.31 Relationship between  $R_{20}$  and  $D_c$



## 4.4 Summary

### 1) Dynamic deformation test

The initial equivalent Young's modulus of clinker ash is smaller than that of Toyoura sand.

When comparing Toyoura sand and clinker ash with the same degree of compaction, the equivalent Young's modulus in clinker ash is smaller in the very small strain region than in Toyoura sand, although it shows a wider elastic region.

Regarding the damping ratio  $h$ , in the strain range where the single amplitude axial strain is less than 0.01%, there is no big difference between clinker ash and Toyoura sand. However, in the strain range where the single amplitude axial strain is larger than 0.01%, Toyoura sand displays higher values than clinker ash. The reason for this is that as the level of strain increases in Toyoura sand, the decrease in rigidity due to liquefaction becomes significant, and as a result,  $h$  increases.

By using the HD model, dynamic deformation characteristics of clinker ash can be modelled to some extent.

### 2) Bender Element Tests

In the same way as the dynamic deformation test results, in comparison with Toyoura sand the results gained for clinker ash are slightly lower, however an increase in degree of compaction leads to an increase in initial shear modulus.

Up to a gravel content of around 30%, the initial shear modulus increases slightly with an increase in gravel content, however after 30%, there is no real change.

Conversely, there is a slight tendency for the initial shear modulus to decrease with increasing fines content.

When comparing the results of initial shear modulus from bender element tests and those of

other tests, it is clear that the values from the bender element tests are slightly higher. This is a trend which has also been seen in past research on Toyoura sand and is due to the results being the initial shear modulus  $G_0$ , rather than the shear modulus taken after strain has been applied.

### 3) Liquefaction test

Clinker ash was found to display similar or higher strength than Ube Masado at low degrees of compaction, and an increase in degree of compaction leads to a great increase in liquefaction strength.

When the specimens are compacted to over  $D_c=95\%$ , a clear difference in liquefaction resistance becomes apparent between all of the clinker ash samples and Ube Masado. The strengths of the clinker ash samples become around 1.5 times that of Ube Masado, and the increase in degree of compaction from  $D_c=85\%$  to around  $D_c=97\%$  leads to an increase in strength of the clinker ash from between 1.5 to 3 times as much.

## References

- 1) Hardin B.O. and Drnevich V.P. (1972) Shear modulus and damping in soils: design equations and curves, *Journal of Soil Mechanics and Foundations Division, ASCE*. 98(6), 603-624.
- 2) Taichi K, Shigeo I, Yukihiro K, Fumio T, Masaru T (1994) The deformation properties on triaxial specimen of Kanto-loam in micro-strain range, *Bulletin of Kisarazu National College of Technology*, 27, 49-55.
- 3) Shirley D.J. and Hampton L.D. (1977) Shear wave measurements in laboratory sediments, *Journal of Acoustical Society of America*, 62(2), 607-613.
- 4) Lings M.L. and Greening P.D. (2001) A novel bender/extender element for soil testing, *Geotechnique*, 51(8), 713-717.

- 5) Japanese Geotechnical Society (2013) JGS 0544-2011 Method for laboratory measurement of shear wave velocity of soils by bender element test, *Newly Established Geo-Technology Engineering Standards*, 4.
- 6) International parallel test on the measurement of  $G_{\max}$  using bender elements organized by TC-29 (2003), 64.
- 7) Wakatsuki Y, Hyodo M, Yoshimoto N, Anai R, Yoshinaga Y, Yoshioka I, Nakashita A. (2009) Particle characteristics and strength, deformation characteristics of loose clinker ash, *Journal of Japan Society of Civil Engineers*, 65(4), 897-914.

## **Chapter 5 Conclusions and further research**

### **5.1 Conclusions**

In Chapter 2, the material properties of the clinker ash samples used in this research were investigated. It was found to be a relatively light material with low optimum water content and high maximum dry density compared with natural sands. Clinker ash displays a wide range of particle distributions although it can be classified as a sandy or gravelly soil. The porous nature of the particles leads to relatively large minimum and maximum void ratios.

Through microscopic observation and evaluation of clinker ash particles the complex shape and nature could be made clear and it was found that clinker ash has much more complex and angular particle shapes than those of natural sands. However, after particle crushing tests were performed it was found that the crushing strength of the clinker ash particles is relatively weak compared to that of natural sands and clinker ash is identified as a crushable material. Although this can be a negative aspect for a ground material, we can see in further chapters that despite the weak particle strength, clinker ash still displays desirable shear characteristics.

In Chapter 3, the static shear characteristics of the clinker ash samples were investigated through static triaxial compression tests. A wide range of tests were performed under various conditions in order to gain a clear understanding of what affects or influences the shear behaviour of clinker ash. It was found that due to being a crushable material, an increase in confining pressure would lead to a decrease in peak strength, due to particle breakage occurring. Even so, clinker ash still displayed high shear strength under such high stress conditions. Even in the loose state the clinker ash samples displayed relatively high strength, with this increasing remarkably with an increase in density. Under

low stress, low density conditions it was found that particle shape had the most effect on peak strength, whereas under high stress and high density conditions the particle crushing strength was more important. Through analysis of test data and using an adaptation of Bolton's equation for the peak strength of sands it was possible to predict the peak strength to a good degree if the residual strength, particle crushing strength and aspect ratio of a sample are known.

In Chapter 4, the dynamic shear characteristics of the clinker ash samples were investigated through dynamic deformation tests, bender element tests and liquefaction tests. From the dynamic deformation testing, it was found that the initial equivalent Young's modulus of clinker ash is smaller than that of Toyoura sand. However, when comparing Toyoura sand and clinker ash with the same degree of compaction, the equivalent Young's modulus in clinker ash may be smaller in the micro-strain region but it shows a wider elastic region. As for the damping ratio  $h$ , in the strain range where the single amplitude axial strain is less than 0.01%, there is no big difference between clinker ash and Toyoura sand. However, in the strain range where the single amplitude axial strain is larger than 0.01%, Toyoura sand displays higher values than the clinker ash. The reason for this is that as the level of strain increases in Toyoura sand, the decrease in rigidity due to liquefaction becomes significant, and as a result,  $h$  increases. By using the HD model, the dynamic deformation characteristics of clinker ash could be modeled to some extent.

Bender element testing also showed that in comparison with Toyoura sand, the results gained for the initial shear modulus of clinker ash are slightly lower, however an increase in degree of compaction leads to an increase in stiffness. Although there was no clear difference in initial stiffness of clinker ash samples based on any material properties, the amount of gravel or fines content seemed to have some slight influence, with higher gravel content leading to a slight increase in initial stiffness. When comparing the results of initial shear modulus from bender element tests and those of other tests, it is

clear that the values from the bender element tests are slightly higher. This is a trend which has also been seen in past research on Toyoura sand.

Clinker ash was found to display similar or higher liquefaction strength than Ube Masado at low degrees of compaction, and an increase in degree of compaction leads to a great increase in liquefaction strength. When the specimens are compacted to over  $D_c=95\%$ , a clear difference in liquefaction resistance becomes apparent between all of the clinker ash samples and Ube Masado. The strength of the clinker ash samples become around 1.5 times that of Ube Masado, and the increase in degree of compaction from  $D_c=85\%$  to around  $D_c=97\%$  leads to an increase in strength of the clinker ash from between 1.5 to 3 times as much.

## **5.2 Further research**

From the initial investigation into the material properties of the clinker ash samples to be used in this research, it became clear that there can be differences in many aspects of the different samples. The samples came from 6 different power plants, however, over time the properties of clinker ash even from the same power plant can change. Some reasons for this could be the type of coal that is being incinerated, the boiler type and incineration method and the process of formation. A further area of research could focus more on these aspects, in order to investigate the core of the influences on differences in properties and behaviour.

In this research, the static shear behaviour was investigated through many tests with various conditions, and the shear characteristics could be evaluated quite satisfactorily. For the dynamic shear tests however, less tests were performed and as such it is slightly more difficult to evaluate the results based on material properties. In the future, it would be interesting to focus more on the dynamic shear aspect, especially with further investigation into the liquefaction characteristics. As the liquefaction

tests were only performed under an effective confining pressure of  $\sigma_c' = 100\text{kPa}$ , a further topic could be to perform the tests under effective confining pressures of  $\sigma_c' = 50\text{kPa}$  and  $200\text{kPa}$  as well. In this way, the change in liquefaction strength due to change in stress could be compared with that of the static shear strength and a link between the two could become possible to investigate.

## Appendices

### A. Table of physical properties

Table A.1 gives a list of the physical properties of the clinker ash samples used in this research.

Table A.1 List of physical properties

	$\rho_s$ (g/cm <sup>3</sup> )	$\rho_{dmax}$ (g/cm <sup>3</sup> )	$w_{opt}$ (%)	$\rho_{dmax}$ (g/cm <sup>3</sup> )	$\rho_{dmin}$ (g/cm <sup>3</sup> )	$e_{max}$	$e_{min}$
CA	2.072	1.019	37.71	1.063	0.754	1.748	0.949
CB	2.151	0.948	40.22	1.070	0.813	1.646	1.010
CC	2.173	1.102	34.09	1.154	0.830	1.618	0.883
CD	2.132	1.014	38.46	1.130	0.857	1.488	0.887
CE	2.151	1.140	29.6	1.228	0.888	1.422	0.752
CF	2.110	1.085	34.74	1.193	0.870	1.425	0.769

	$U_c$	$d_{50}$	$G_c$ (%)	$S_c$ (%)	$F_c$ (%)	$R_c$	$A_r$	After Compaction $B_M(\%)$	After Max Density $B_M(\%)$
CA	20.3	0.57	25.8	60.1	14.1	2.73	1.55	6.8	8.6
CB	12.5	0.21	23	54.1	22.9	2.55	1.46	9.8	9.4
CC	13.8	1.3	31.6	63.0	5.5	3.04	1.42	12.7	10.1
CD	-	0.22	19.7	53.5	26.8	3.39	1.60	3.9	5.2
CE	26.7	0.71	24.2	61.7	14.2	2.63	1.45	6.1	4.4
CF	21	1.75	41.6	50.9	7.5	2.55	1.44	9.3	12.2



## B. Stress-strain relationships from triaxial compression tests

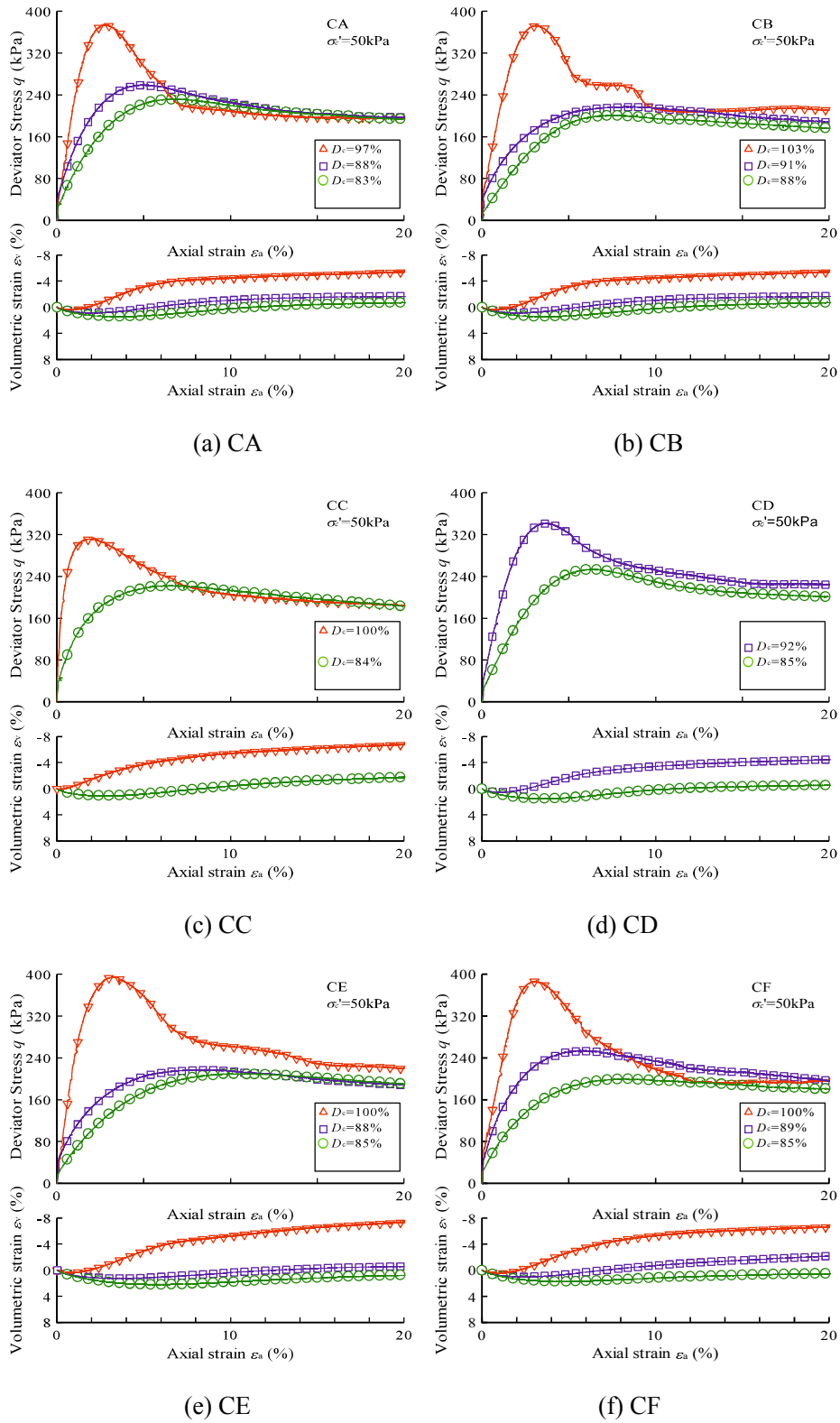
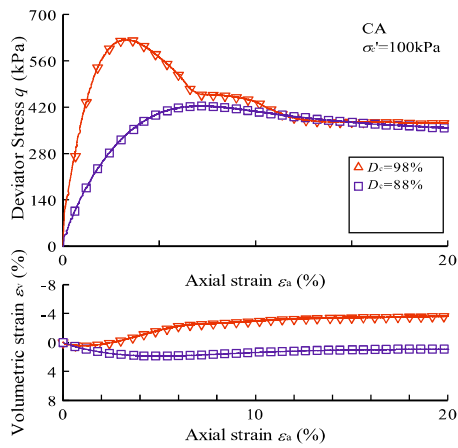
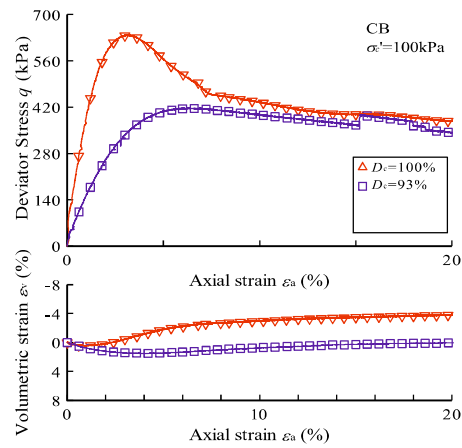


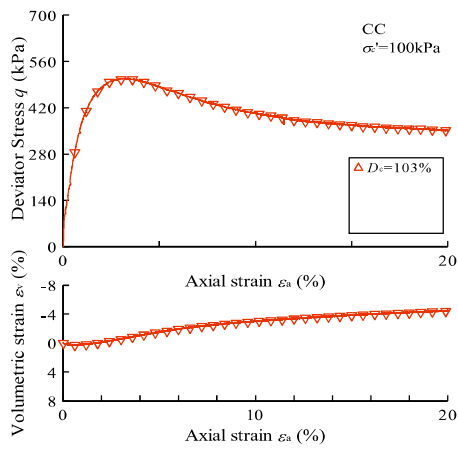
Figure B.1 Stress-strain relationships with  $\sigma'_c = 50$  kPa



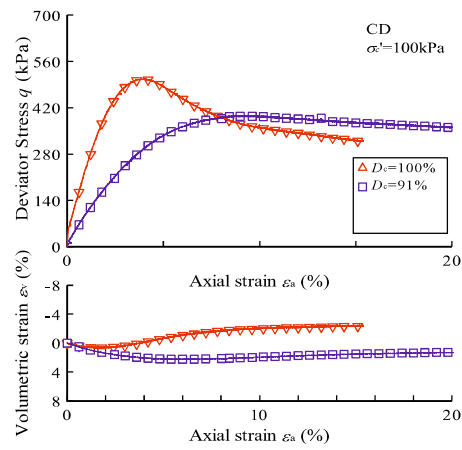
(a) CA



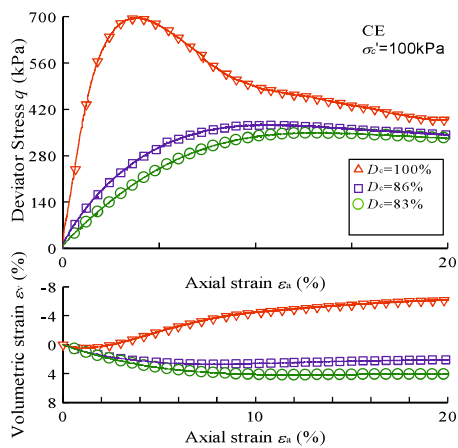
(b) CB



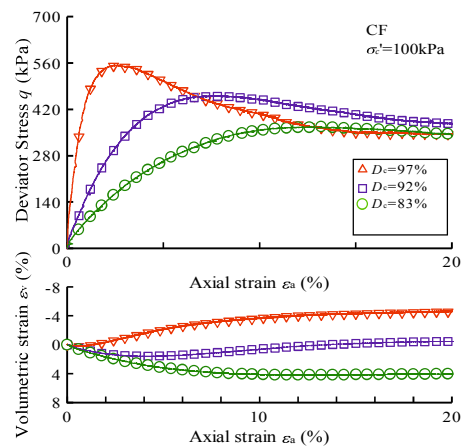
(c) CC



(d) CD

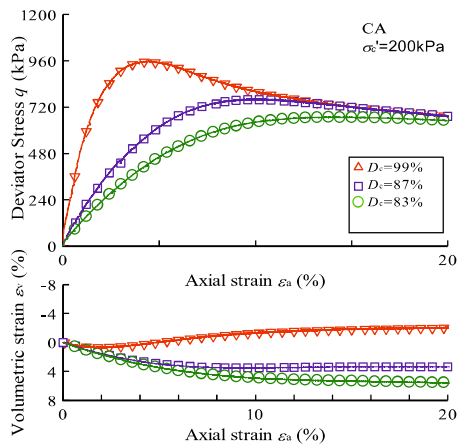


(e) CE

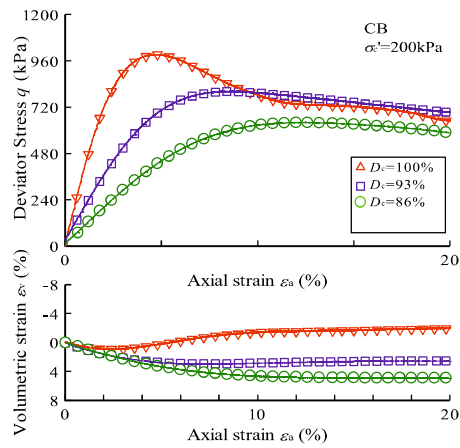


(f) CF

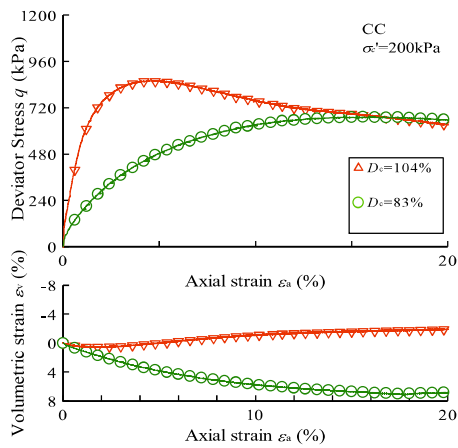
Figure B.2 Stress-strain relationships with  $\sigma_c' = 100 \text{ kPa}$



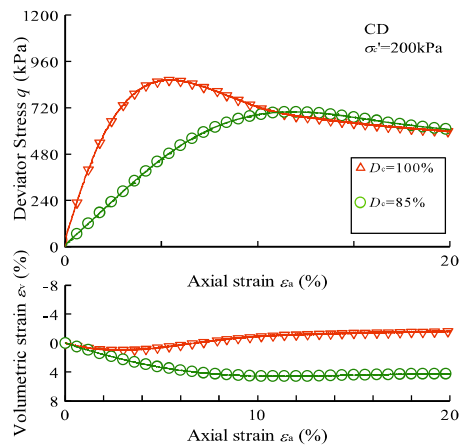
(a) CA



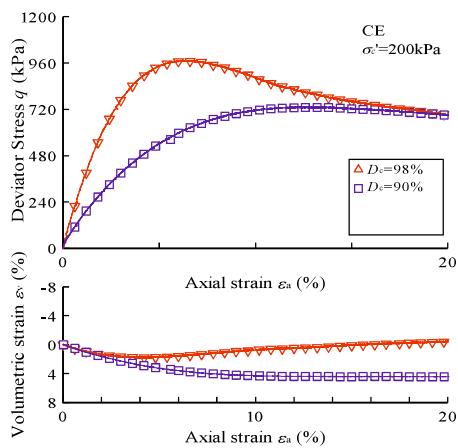
(b) CB



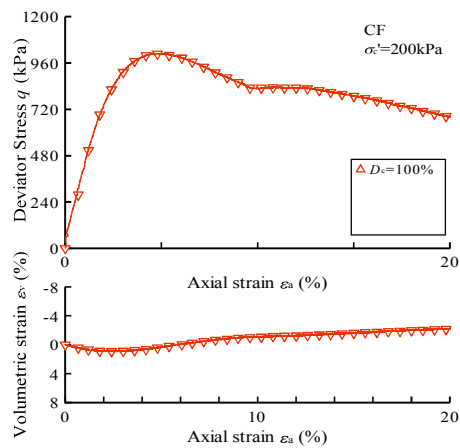
(c) CC



(d) CD



(e) CE



(f) CF

Figure B.3 Stress-strain relationships with  $\sigma_c' = 200 \text{ kPa}$

### C. Mohr's stress circles from triaxial compression tests

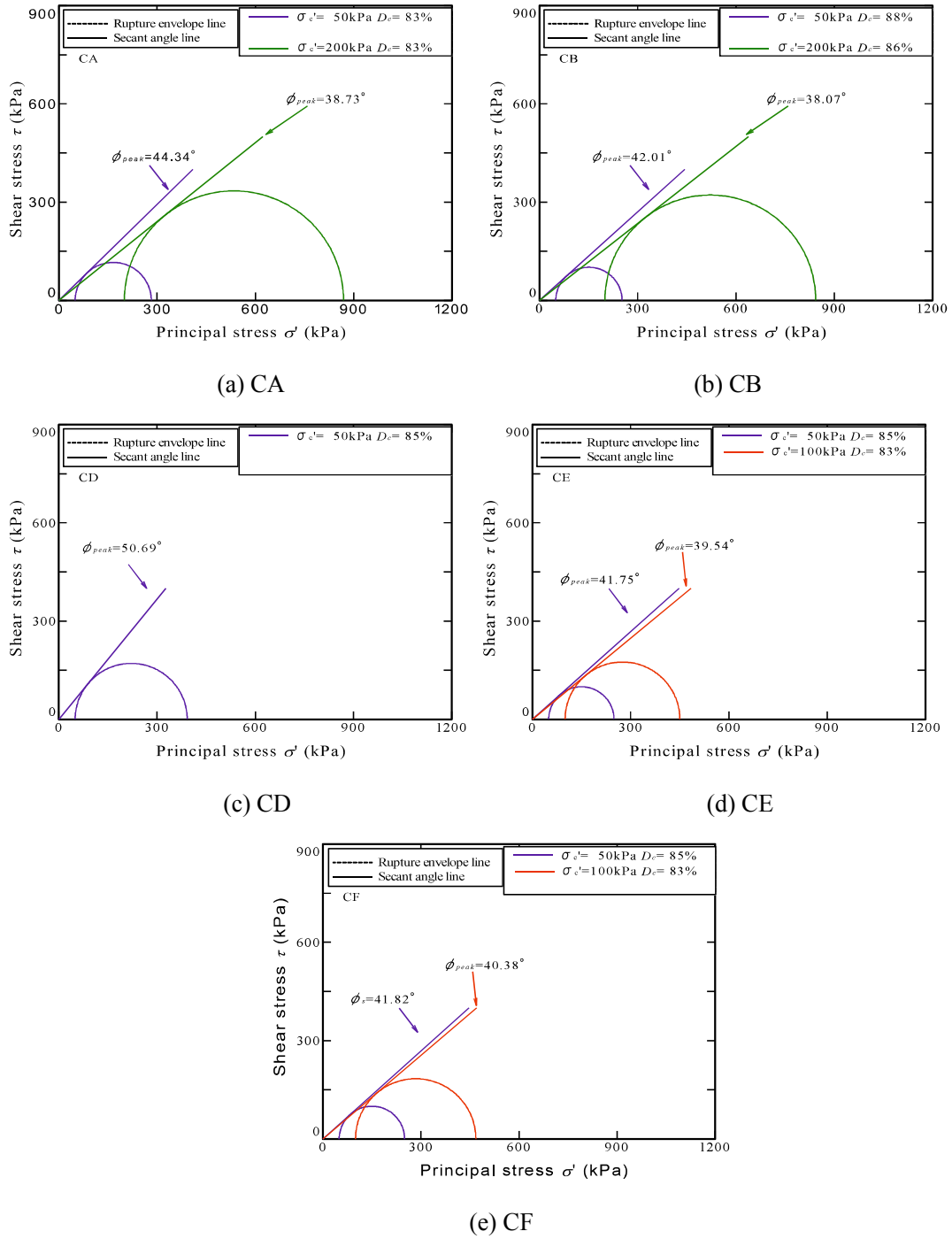
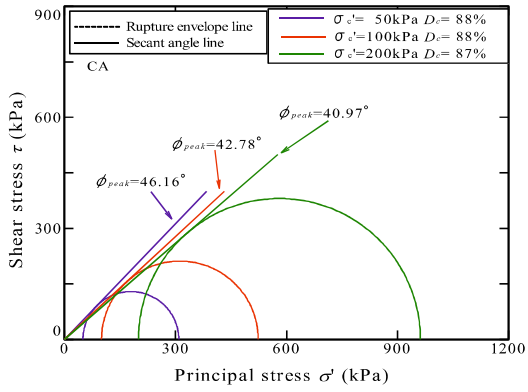
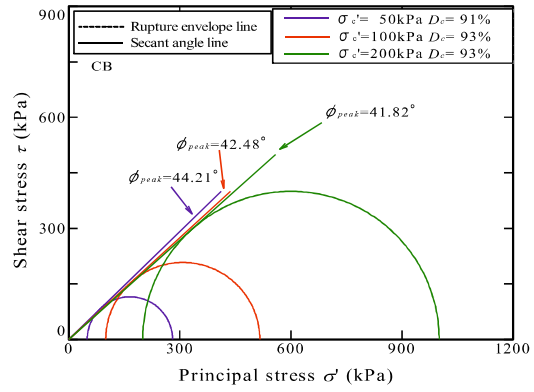


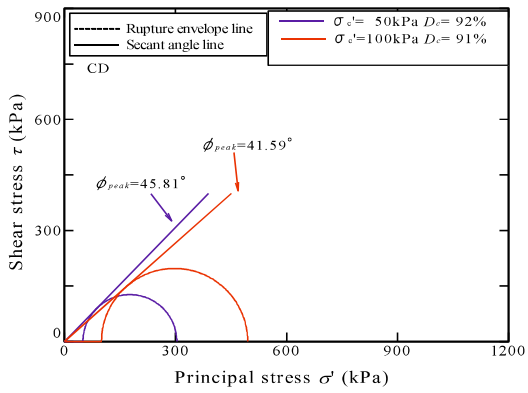
Figure C.1 Mohr's circles with  $D_c=85\%$



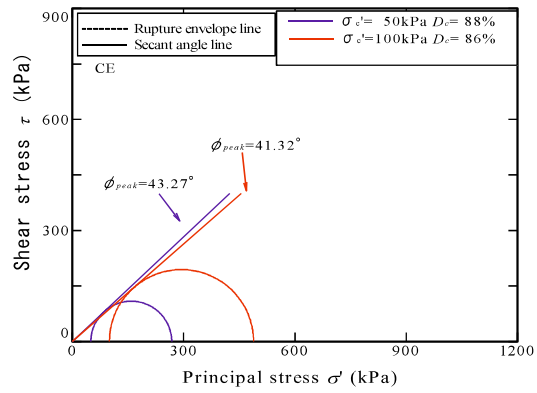
(a) CA



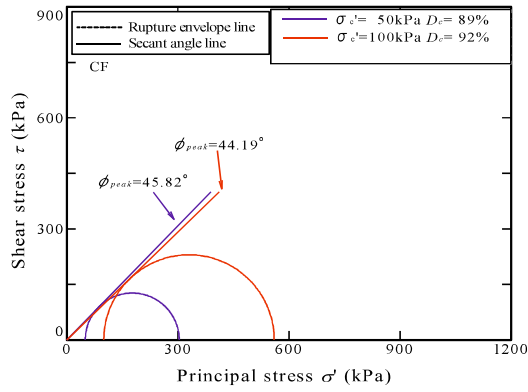
(b) CB



(c) CD



(d) CE



(e) CF

Figure C.2 Mohr's circles with  $D_c=90\%$

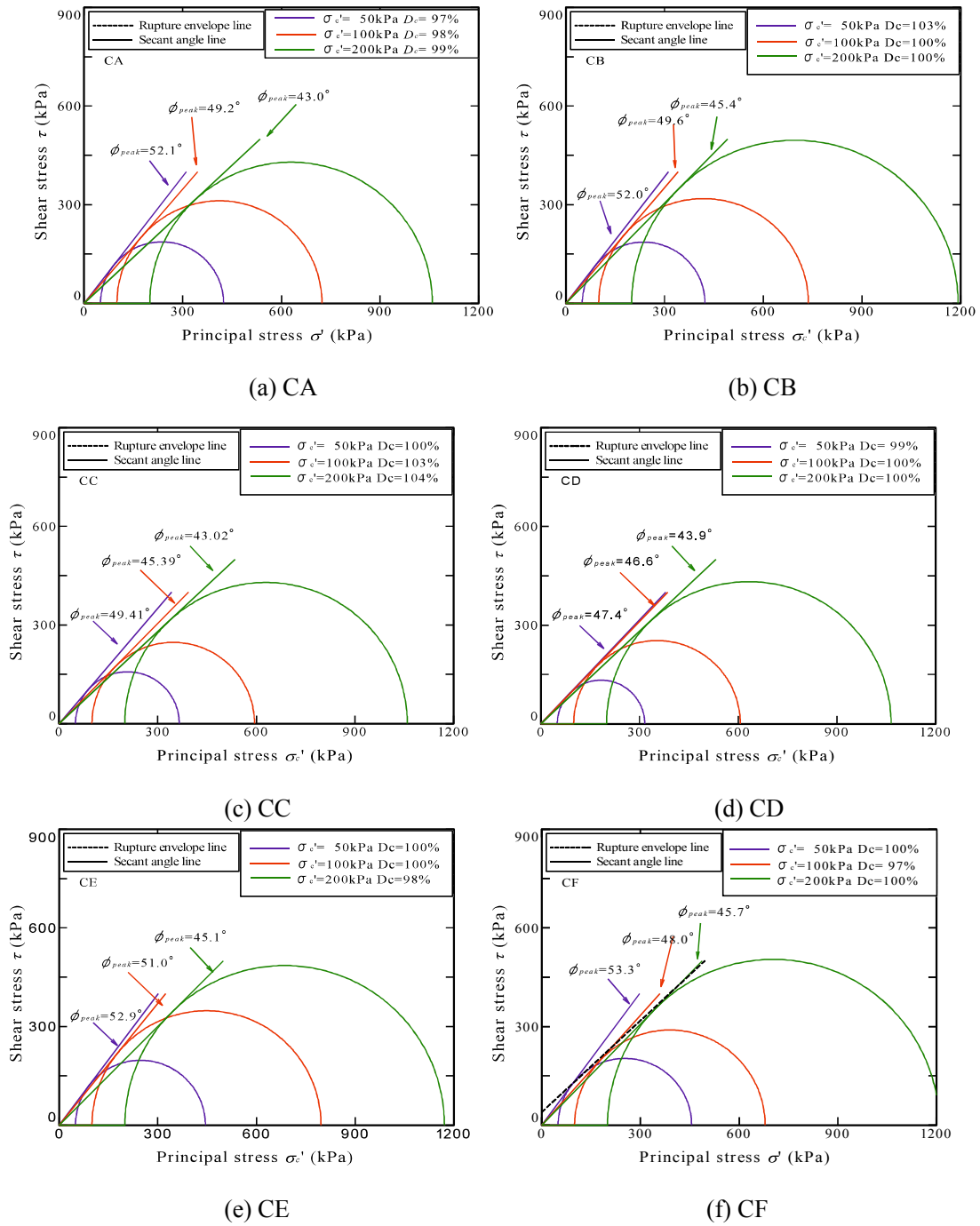


Figure C.3 Mohr's circles with  $D_c=100\%$

D. Test results from cyclic triaxial liquefaction tests

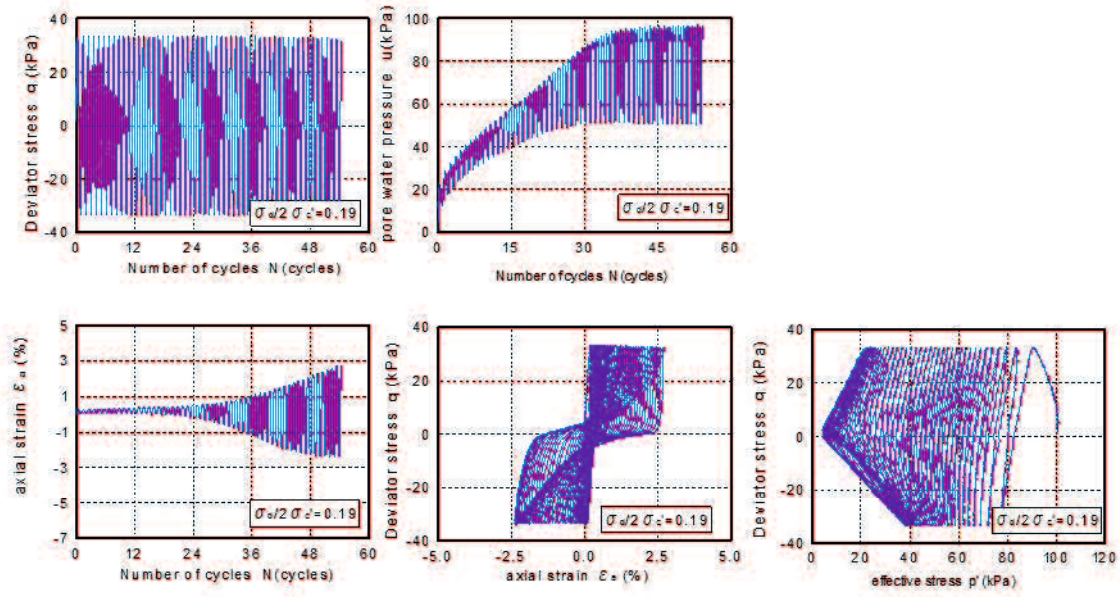


Figure D.1 CC  $\sigma_d/2\sigma'_c = 0.19$   $D_c = 85\%$

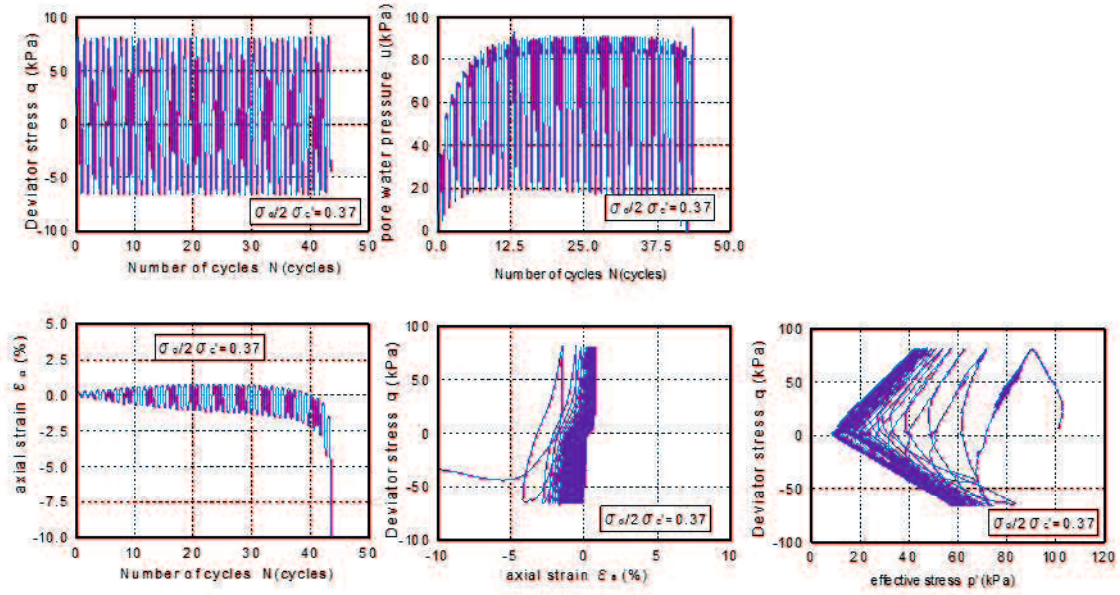


Figure D.2 CC  $\sigma_d/2\sigma'_c = 0.37$   $D_c = 97\%$

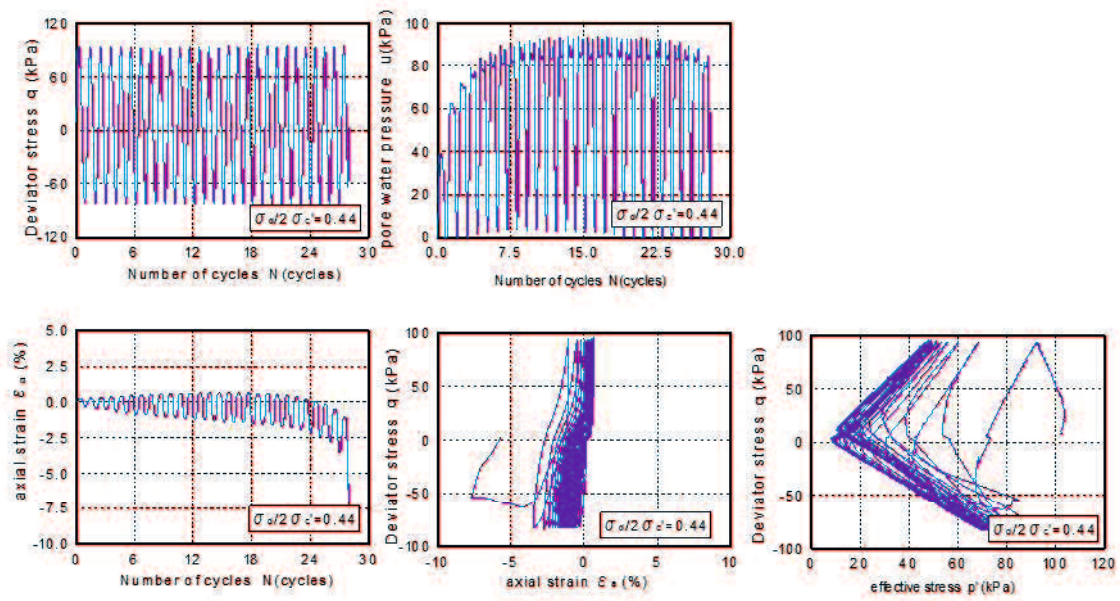


Figure D.3 CC  $\sigma_d/2\sigma'_c = 0.44$   $D_c = 97\%$

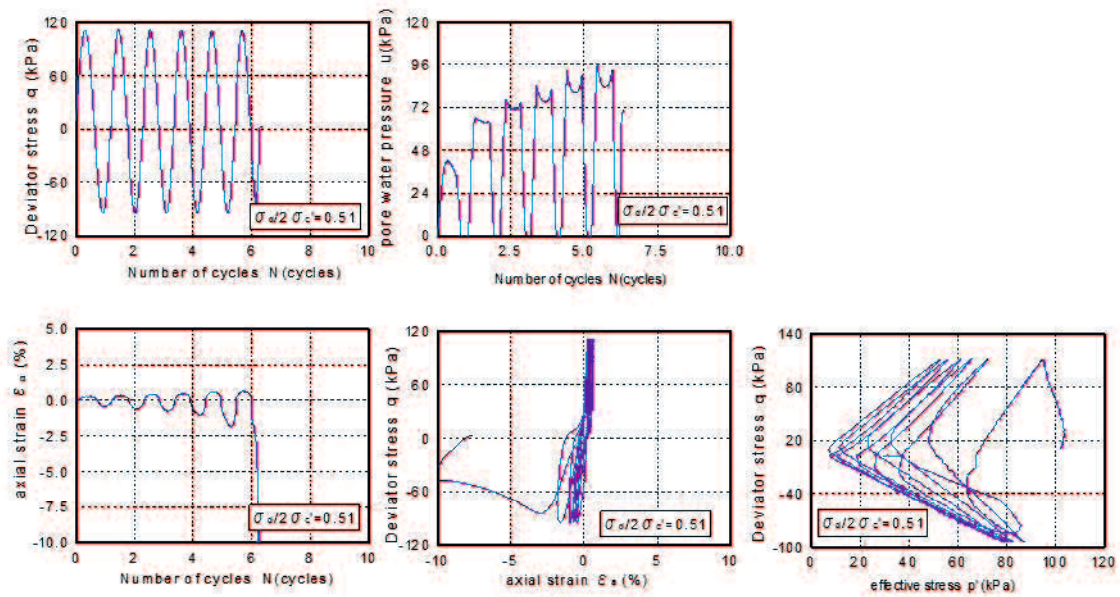


Figure D.4 CC  $\sigma_d/2\sigma'_c = 0.51$   $D_c = 97\%$



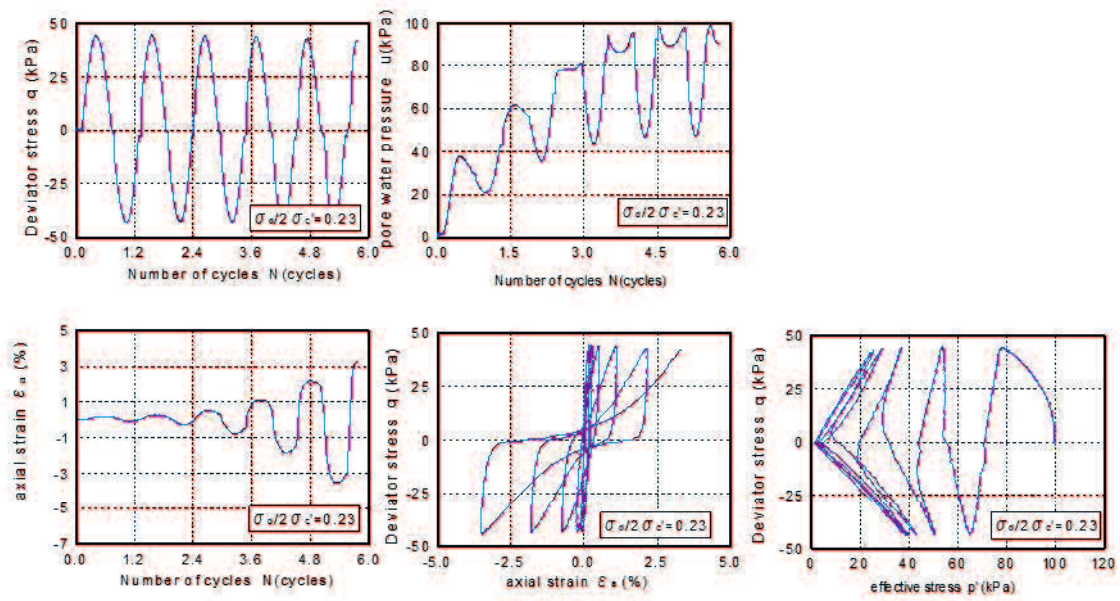


Figure D.5 CD  $\sigma_d/2\sigma_c' = 0.23$   $D_c = 85\%$

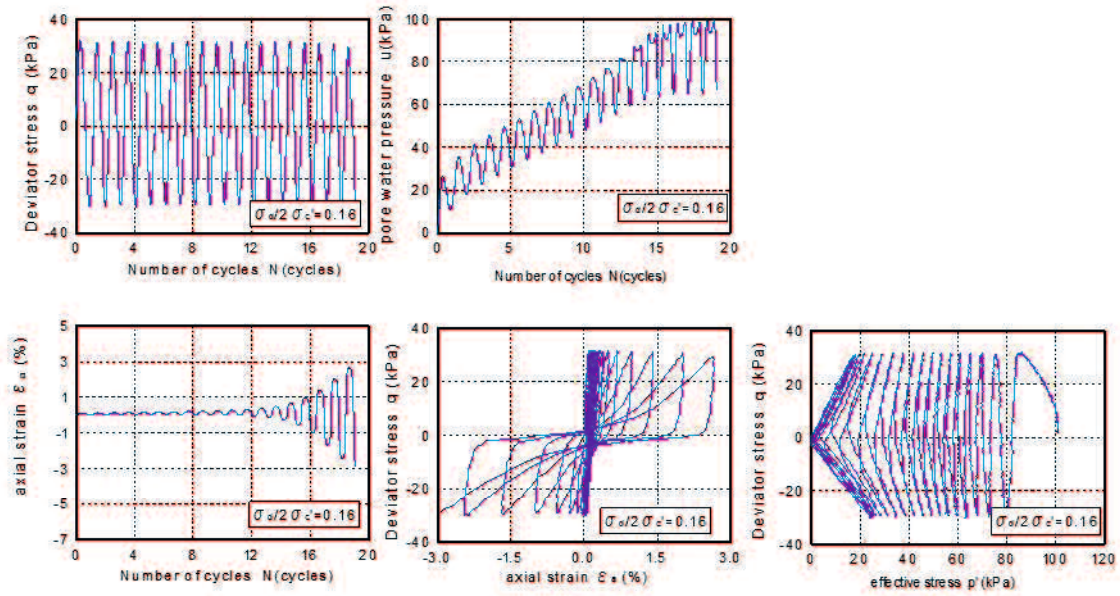


Figure D.6 CD  $\sigma_d/2\sigma_c' = 0.16$   $D_c = 85\%$

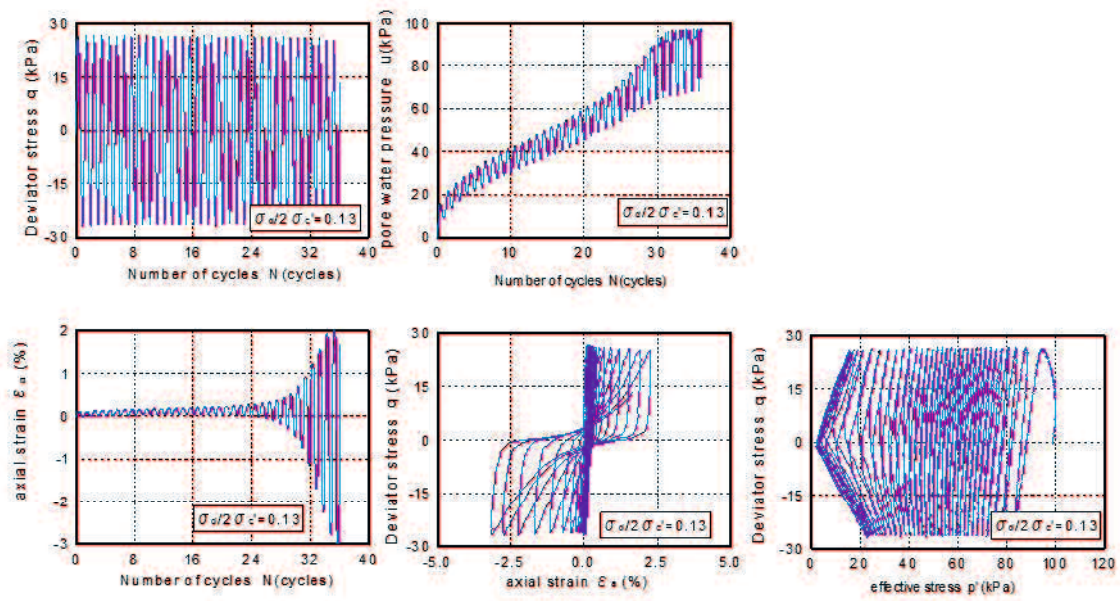


Figure D.7 CD  $\sigma_d/2\sigma'_c = 0.13$   $D_c = 85\%$

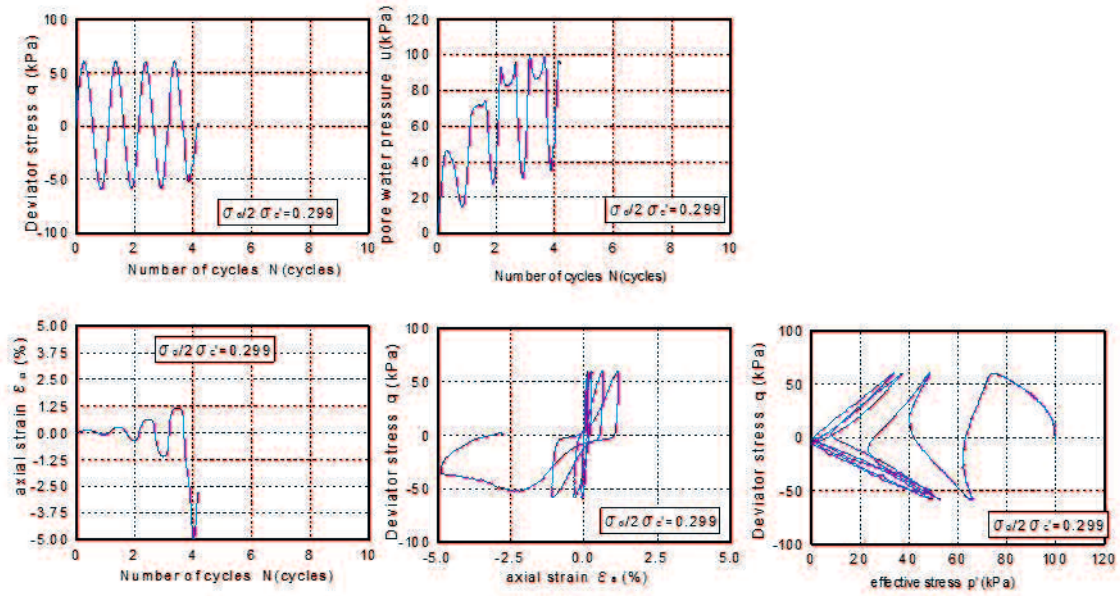


Figure D.8 CD  $\sigma_d/2\sigma'_c = 0.30$   $D_c = 85\%$

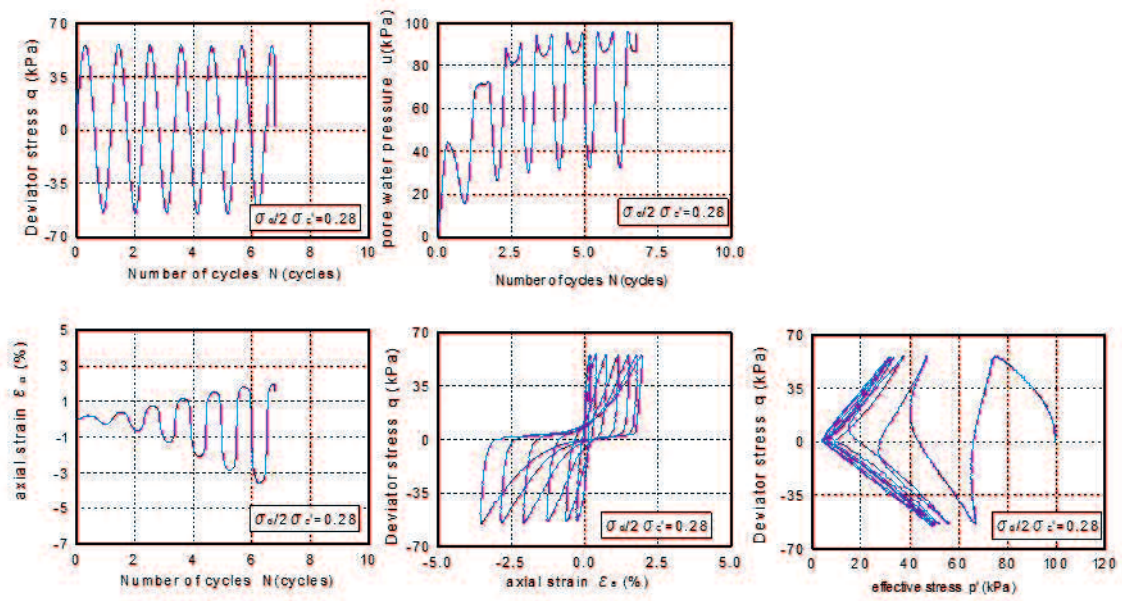


Figure D.9 CD  $\sigma_d/2\sigma_c' = 0.28$   $D_c = 90\%$

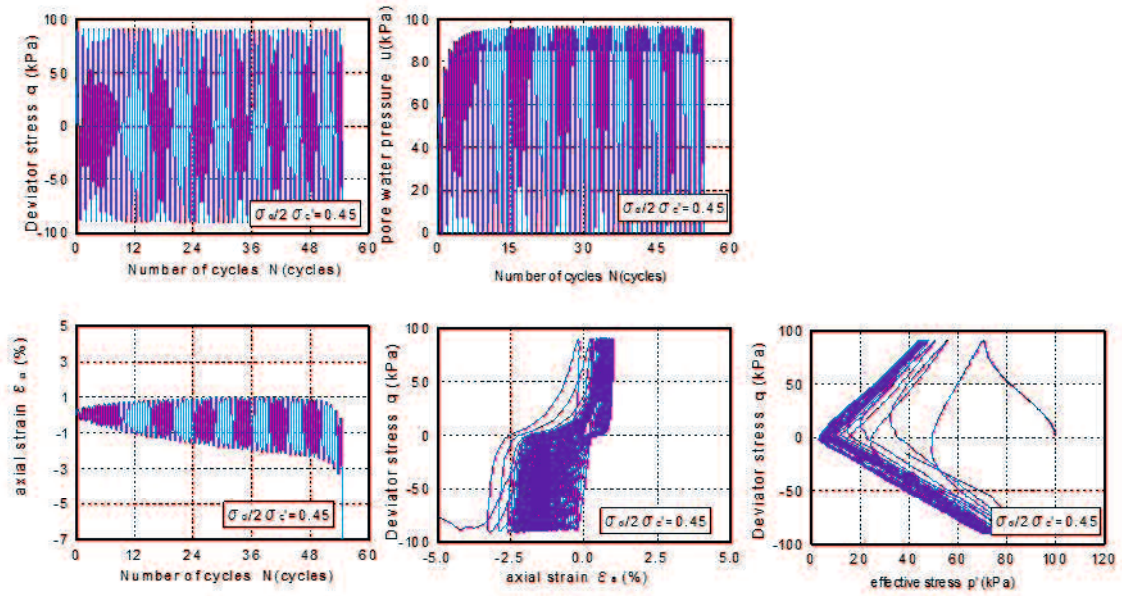


Figure D.10 CD  $\sigma_d/2\sigma_c' = 0.45$   $D_c = 99\%$

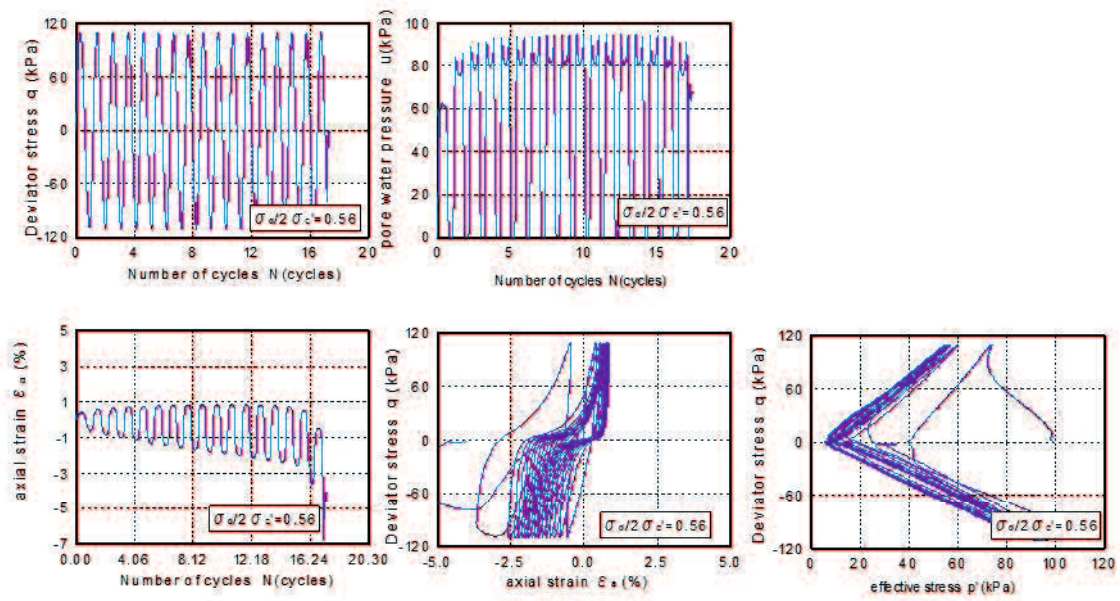


Figure D.11 CD  $\sigma_d/2\sigma_c = 0.56$   $D_c = 99\%$

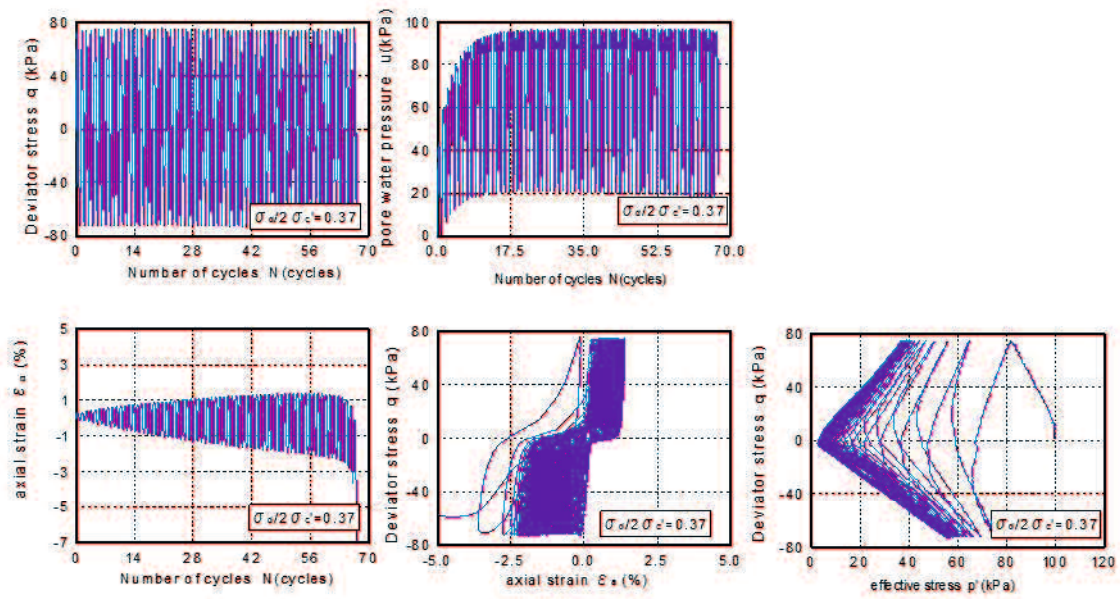


Figure D.12 CD  $\sigma_d/2\sigma_c = 0.37$   $D_c = 99\%$

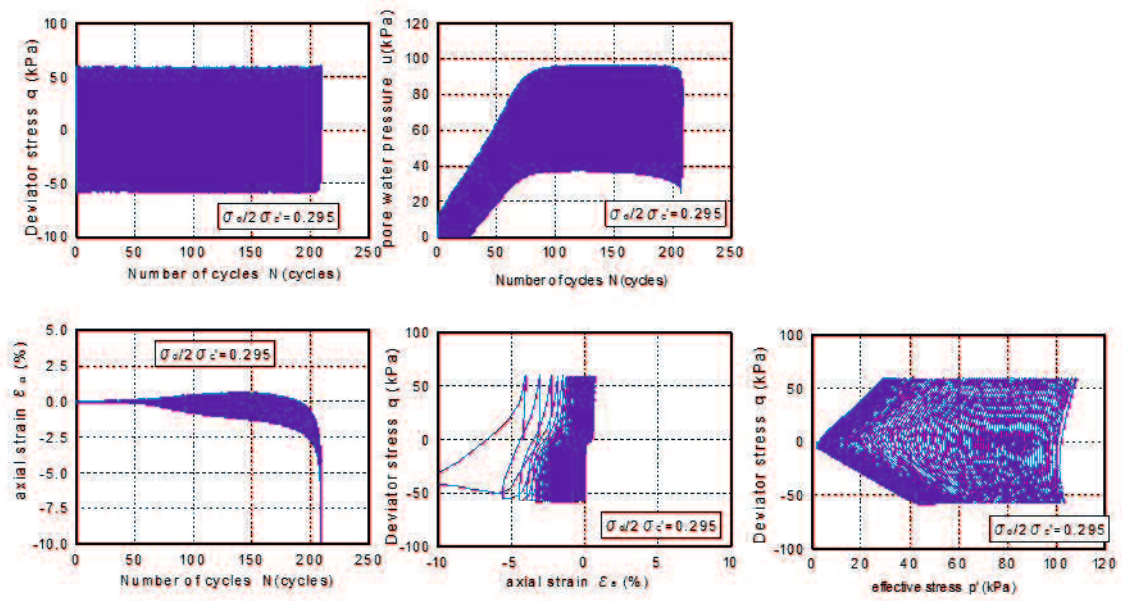


Figure D.13 CD  $\sigma_d/2\sigma_c' = 0.30$   $D_c = 99\%$

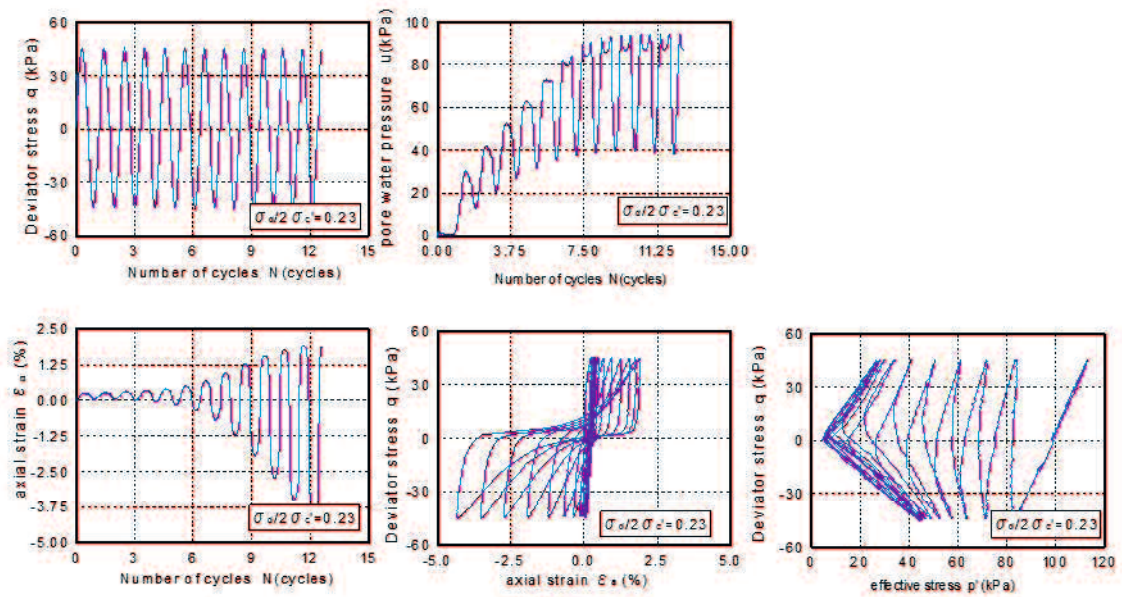


Figure D.14 CE  $\sigma_d/2\sigma_c' = 0.23$   $D_c = 85\%$

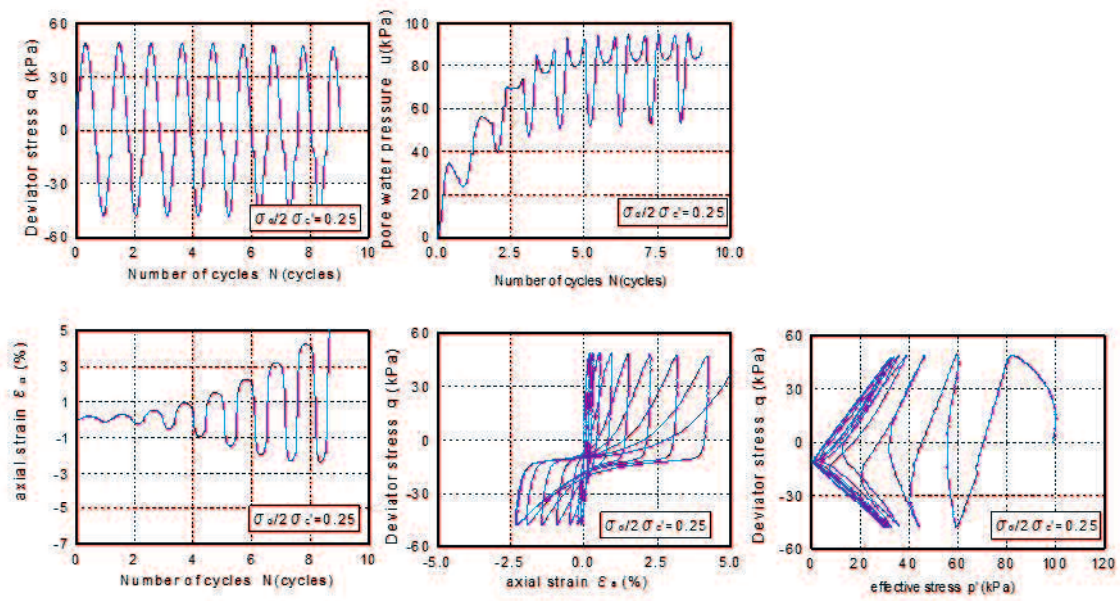


Figure D.15 CE  $\sigma_d/2\sigma_c = 0.25$   $D_c = 85\%$

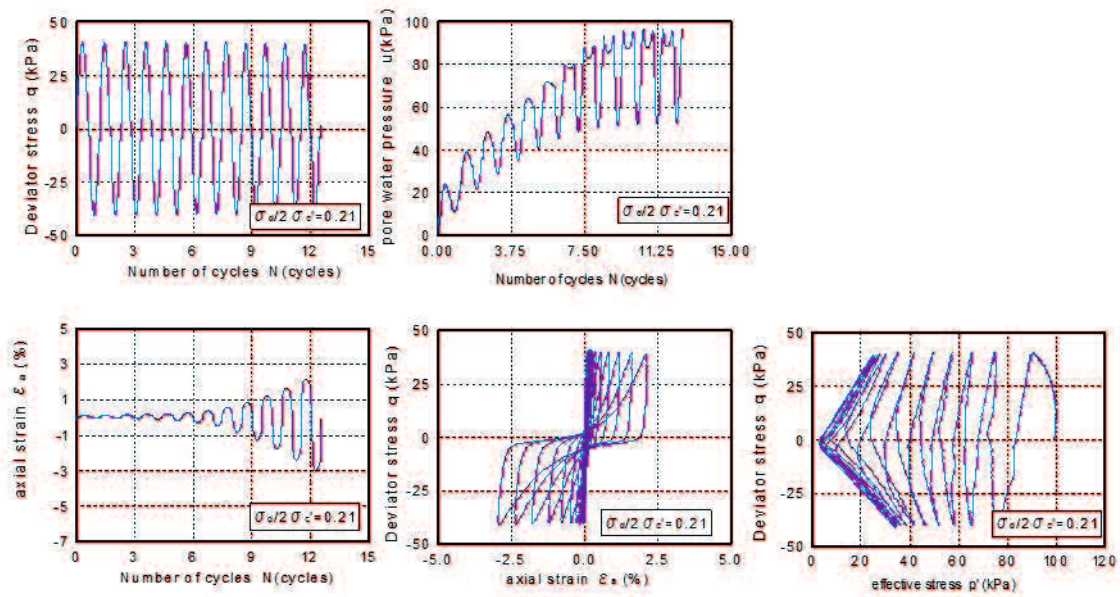


Figure D.16 CE  $\sigma_d/2\sigma_c = 0.21$   $D_c = 85\%$

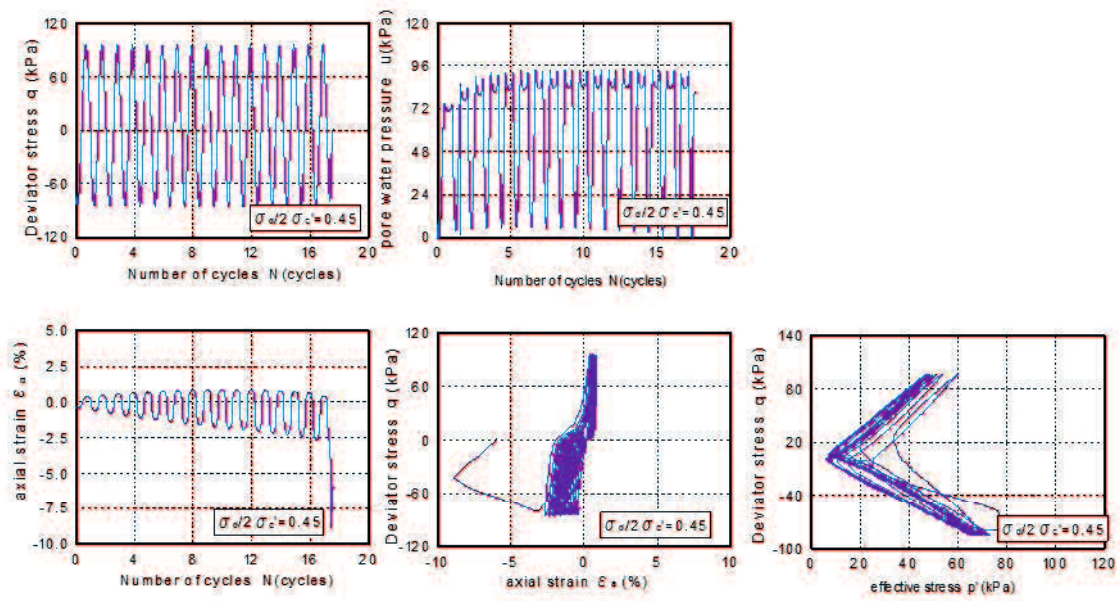


Figure D.17 CE  $\sigma_d/2\sigma_c = 0.45$   $D_c = 97\%$

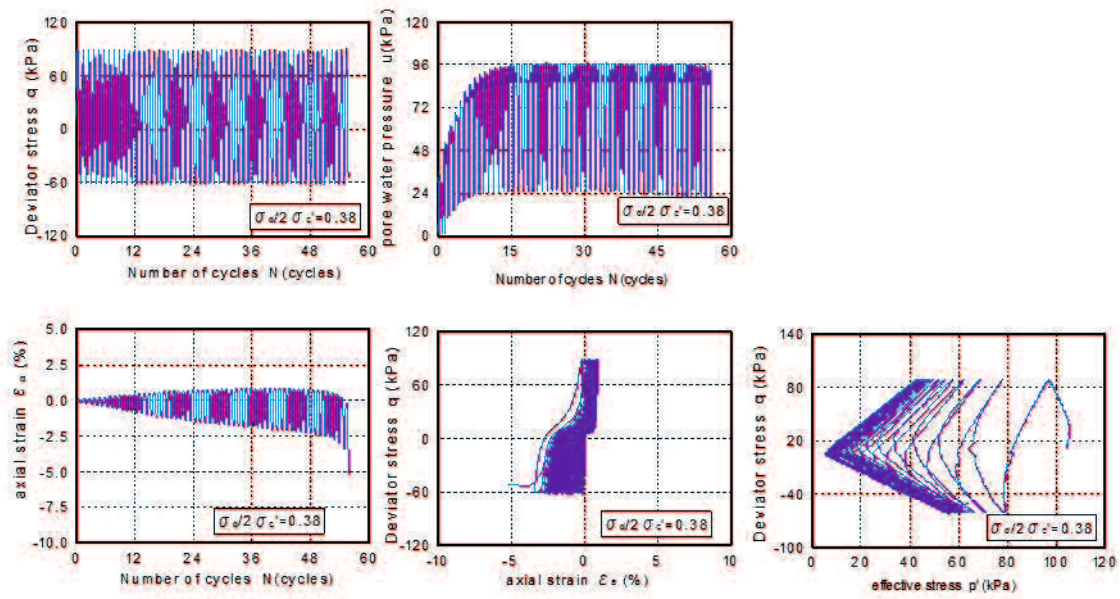


Figure D.18 CE  $\sigma_d/2\sigma_c = 0.38$   $D_c = 97\%$

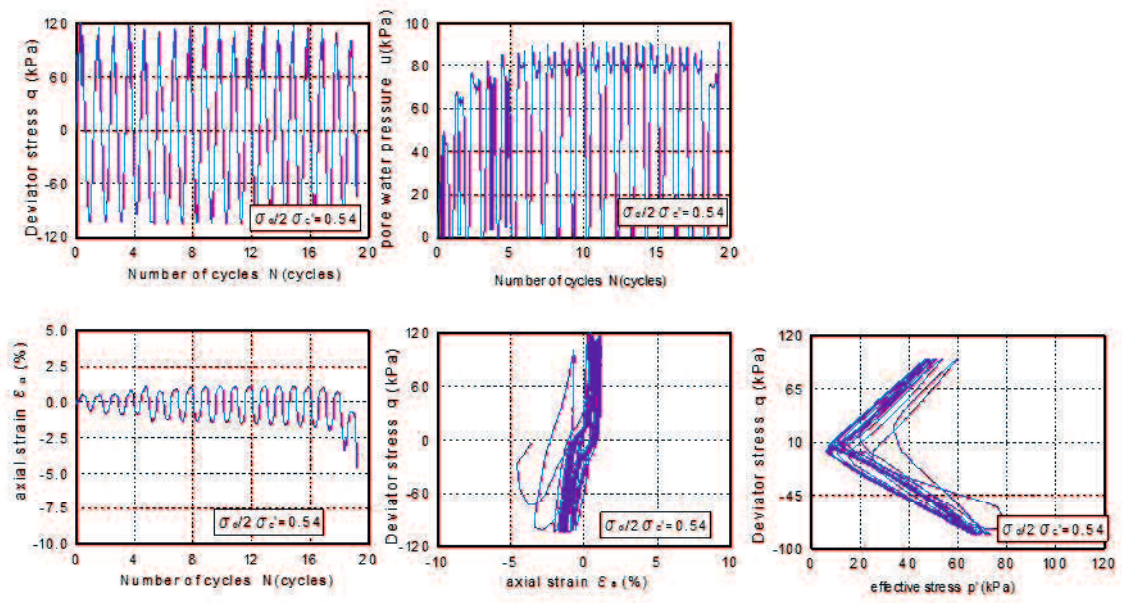


Figure D.19 CE  $\sigma_d/2\sigma_c = 0.54$   $D_c = 97\%$